

Epitaxial growth and charge-to-spin
conversion studies of Bi_2Te_3 topological
insulator

zur Erlangung des Doktorgrades der Naturwissenschaften
(Dr. rer. nat.)

der

Naturwissenschaftlichen Fakultät II
Chemie, Physik und Mathematik

der Martin-Luther-Universität
Halle-Wittenberg

vorgelegt von

Frau **Jue Huang**

geb. am 24.12.1989 in Anhui, China

Gutachter:

Prof. Dr. Stuart S. P. Parkin

Prof. Dr. Ingrid Mertig

Prof. Dr. Thorsten Hesjedal

Tag der öffentlichen Verteidigung:

29.06.2021

Contents

Contents	i
List of Figures	iii
List of Tables	vii
Abbreviations	ix
Abstract	xi
1 Introduction	1
1.1 Topological insulators	1
1.1.1 Background of topological insulators	1
1.1.2 Surface states in topological insulators	4
1.1.3 Electronic transport and spin-momentum locking	6
1.2 Spintronics: spin and charge transport	8
1.2.1 Fundamental concepts	8
1.2.2 Spin Hall effect and inverse spin Hall effect	10
1.2.3 Spin transfer torque	13
1.2.4 Spin orbit torque	16
1.3 Motivation and outline	18
2 Experimental Instruments and Techniques	20
2.1 Ultra high vacuum technology	20
2.2 Molecular beam epitaxy	26
2.3 Structural characterizations	29
2.3.1 Reflection high energy electron diffraction	29
2.3.2 Complementary <i>ex-situ</i> characterizations	30
3 Epitaxial Growth and Characterization of Bi₂Te₃ Thin Films	35

3.1	General considerations	35
3.2	Epitaxial growth of Bi_2Te_3 thin films	36
3.2.1	Growth of $\text{STO}(111)/\text{Bi}_2\text{Te}_3$	37
3.2.2	Growth of $\text{Al}_2\text{O}_3(0001)/\text{Bi}_2\text{Te}_3$	40
4	Electronic Transport Measurements	44
4.1	Measurement geometry	44
4.2	Hall effect	46
4.3	Temperature dependence of resistivity, carrier density and mobility	47
5	Spin Torque Ferromagnetic Resonance Experiments	53
5.1	Spin torque ferromagnetic resonance	53
5.2	Sample preparation and device fabrication	57
5.3	Experiments and results	58
5.4	Discussion	65
6	Summary and Outlook	70
6.1	Summary	70
6.2	Outlook	71
A	Cleaning of $\text{Al}_2\text{O}_3(0001)$ Substrates	73
	Bibliography	75
	Publications	93
	Acknowledgements	95
	Curriculum Vitae	97
	Eidesstattliche Erklärung	99

List of Figures

1.1	Schematic figures of quantum Hall effect and quantum spin Hall effect. (a) chiral edge charge current in the QH state [1], (b) quantized Hall resistance [2], (c) a pair of edge spin current in the QSH state [1], (d) The spin-Hall conductance with a plateau value close to $2\frac{e^2}{h}$ [3]. Figures are adapted from Ref. [1–3].	3
1.2	Schematic figures of band structures of TI and normal insulator. The red and blue colours represent different band components.	6
1.3	Spin momentum locking in TI. (a) Schematic diagram of the spin texture [4]; (b) Concept drawing of the transport experiment [4]; (c) Fitted values of the spin polarization vector which demonstrates the topological helicity of the spin-Dirac cone [5]; (d) ARPES dispersion of Bi ₂ Te ₃ along the kx cut [5]; (e) ARPES intensity map at E _F of the (111) surface of Bi ₂ Te ₃ [5]; and (f) Measured y component of spin-polarization along the $\bar{\Gamma} - \bar{M}$ direction at E _B =-20 meV [5]. Figures are adapted from Ref. [4, 5]. The red arrows in the figure represent the spin directions.	7
1.4	Schematic figures of prototypical spintronic devices. (a) Spin valve (b) GMR (c) MTJ and (d) racetrack	9
1.5	Schematic figures describing the (a) anomalous Hall effect and (b) spin Hall effect.	11
1.6	Schematics of Mott scattering. An unpolarized electron beam is injected along LT ₁ direction and scattered by the first target T ₁ . Then the electron beam is scattered by the second target T ₂ and finally detected by two detectors, M and M', which are set symmetrically. If the electron beam is unpolarized after the first scattering, the two detectors will get the same amount of electrons. Otherwise the electron beam is polarized after the first target.	12
1.7	Schematic of spin transfer torque. (a) An unpolarized electron beam is polarized after passing through a magnetic film, either through a spin-flip collision or through the backscattering and (b) spins of electrons in the multilayered heterostructures.	14

1.8	Schematic of (a) STT-MRAM and (b) racetrack Memory. Figures are adapted from Ref. [6].	15
1.9	Schematic of SOT setup. When a current is flowing through the NM layer, a transverse spin current are generated and injected to the FM layer. The torque on the local magnetic moment in FM layer can be split to two components τ_{FL} , which drives the moment into precession around the effective magnetic field, and τ_{DL} , which acts to bring the moment back to its equilibrium position.	17
2.1	Schematic diagram of a routine UHV pumping system for a typical MBE machine.	22
2.2	Schematic diagrams of designs and operations for (a) scroll pump; (b) turbomolecular pump; (c) ion pump and (d) titanium sublimation pump.	24
2.3	Schematic diagram of a simple MBE chamber showing the effusion cells, shutters, substrate heater and RHEED system.	27
2.4	(a) A standard K-cell (MBE-Komponenten GmbH, WEZ 40-10-22-KS), (b) schematic of the wire heating assembly.	28
2.5	Schematics of electron diffraction geometries, film morphologies, and crystalline structures for:(a) A single crystal. (d) Single-crystal islands. (g) Polycrystalline islands. Corresponding Ewald sphere constructions are seen in b, e, and h and corresponding RHEED patterns in c, f, and i. Figures are adapted from [7].	31
2.6	Basic working principle of an contact mode AFM. By scanning a tip across the sample surface, changes of the cantilever deflection is monitored with photodiode detector.	32
2.7	Schematic diagram of diffraction of x-rays by a crystal (Bragg condition).	33
3.1	(a) Binary alloy phase diagram of Bi-Te and (b) Tetradymitetype crystal structure of Bi_2Te_3 . Figures are adapted from Ref. [8, 9] . . .	37
3.2	RHEED patterns of (a) STO (111) substrate, (b) Bi_2Te_3 film of 3 QL on STO(111) with $T_{\text{sub}}=160^\circ\text{C}$, (c) Bi_2Te_3 film of 10 QL on STO(111) with $T_{\text{sub}}=160^\circ\text{C}$ and (d) Bi_2Te_3 film on STO(111) with $T_{\text{sub}}=140^\circ\text{C}$	39
3.3	AFM images showing the surface morphology of the Bi_2Te_3 films growing with substrate temperature at 140°C (a) and 160°C (b), respectively, (c) The line profile taken across the area shown in (b).	40

3.4	The XRD curves for 5 QL Bi_2Te_3 thin film. (a) θ - 2θ scan shows the peaks. The XRR scan is performed between 0 - 6° (2θ) as shown in the insert panel. (b) phi scan profile using the (015) planes for the Bi_2Te_3 layer.	41
3.5	Characterization of Bi_2Te_3 film grown on $\text{Al}_2\text{O}_3(0001)$. (a) and (b) are RHEED patterns of $\text{Al}_2\text{O}_3(0001)$ and 7 QL Bi_2Te_3 film on $\text{Al}_2\text{O}_3(0001)$, respectively; (c) is an AFM image of Bi_2Te_3 film and (d) is the profile taken across the blue area in (c).	42
4.1	Electrical measurement geometries: Van der Pauw geometry (left panel) and Hall bar geometry (right panel). The black circles represent measurement leads and the magnetic field is applied perpendicular to the plane.	45
4.2	Hall effect measurement setup for electrons. By applying a current along x direction and an out-of-plane magnetic field along z direction, a voltage develops along y direction (E_y).	47
4.3	Temperature dependence of longitudinal resistivity for temperature varying from 2 K to 300 K with film thickness $d=5$ QL, 10 QL and 20 QL. The inset shows the resistivity for 5 QL Bi_2Te_3 ranging from 2 K to 30 K.	48
4.4	The normalized magnetoresistance of the film with $d=5$ QL measured at various temperatures. In the weak H regime, the MR shows a steep increase characteristic of WAL with temperature below 20 K.	49
4.5	(a) 2D carrier density of electrons and (b) mobility of electrons in Bi_2Te_3 films grown on $\text{STO}(111)$ obtained by Hall measurements at various temperatures with thickness $d=5$ QL, 10 QL and 20 QL.	51
4.6	Dependence of 2D carrier density on film thickness for Bi_2Te_3 films grown on $\text{STO}(111)$ at various temperatures	52
5.1	The wiring of the circuit to the device. RF generator is attached on high frequency port of the bias tee. Voltage meter is on the DC port.	54
5.2	Illustration of the relation between the ST-FMR line-shape and the direction of the torque. (a)-(c) represent the in-plane torque at the resonance point. The resistance oscillation is in-phase with the driving current, leading to a symmetric line-shape. (d)-(f) describe the out-of-plane torque at the resonance point. The resistance oscillation is 90° out-of-phase with the driving current, leading to an anti-symmetric line-shape [10].	56
5.3	Microscope image of a typical microstrip device after fabrication used for ST-FMR measurements.	58

5.4	System setup of ST-FMR measurement. The RF probe is fixed in the center of the magnetic field and sample holder can be moved in three directions. On the top of the magnet, a microscope is used to observe the position of the device and the probe.	59
5.5	ST-FMR spectra measured on a 10 QL Bi ₂ Te ₃ /5 nm Py sample versus external magnetic field H_{ext} . Solid lines represent fits.	60
5.6	(a) Fitting curve for M_{eff} by using the Kittel formula and (b) a typical mixing voltage signal at resonance, showing the fit and its two components: the black solid line is fit to the data using equation 5.2 where the blue and green lines are the symmetric and antisymmetric Lorentzian fits.	61
5.7	SHA of Bi ₂ Te ₃ films on STO substrate. (a) The frequency dependence and (b) the thickness dependence of SHA for 3 QL, 5 QL, 8 QL, 10 QL Bi ₂ Te ₃ with 5 nm Py, respectively.	61
5.8	Change of linewidth (ΔH_{pp}) versus DC current for Bi ₂ Te ₃ (5 QL)/Py(5 nm) at 8 GHz.	64
5.9	The frequency dependence of measured SHA for 3 QL, 5 QL, 8 QL Bi ₂ Te ₃ with 5 nm Py on Al ₂ O ₃ substrate, respectively.	65
5.10	ST-FMR spectra measured on a 5 QL Bi ₂ Te ₃ /5 nm Py device versus external magnetic field H_{ext} at (a) 4 K and (b) 300 K. Solid lines represent fits.	66
5.11	The frequency dependence of SHA measured at 4 K and 300 K for (a) 3 QL and (b) 5 QL Bi ₂ Te ₃ with 5 nm Py on Al ₂ O ₃ substrate, respectively	66

List of Tables

5.1	Comparison of SHA in topological insulators.	62
-----	--	----

Abbreviations

AFM	Atomic force microscopy
AHE	Anomalous Hall effect
AMR	Anisotropic magnetoresistance
ARPES	Angle-resolved photoemission spectroscopy
BZ	Brillouin zone
DC	Direct current
FM	Ferromagnetic
GMR	Giant magnetoresistance
HE	Hall effect
K-cell	Knudsen effusion cell
MBE	Molecular beam epitaxy
MRAM	Magnetoresistive random access memory
MTJ	Magnetic tunnel junctions
NI	Normal insulator
NM	Non-magnetic
PBN	Pyrolytic Boron Nitride
PID	Proportional–integral–derivative
PPMS	Physical property measurement system
Py	Permalloy
QH	Quantum Hall

QHE	Quantum Hall effect
QL	Quintuple layer
QSH	Quantum spin Hall
QSHE	Quantum spin Hall effect
REE	Rashba-Edelstein effect
RF	Radio frequency
RHEED	Reflection high-energy electron diffraction
SHA	Spin Hall angle
SHE	Spin Hall effect
SOC	Spin-orbital coupling
SOT	Spin orbit torque
SQUID	Superconducting quantum interference device
ST-FMR	Spin torque ferromagnetic resonance
STO	Strontium titanate
STT	Spin transfer torque
TI	Topological insulator
TMDs	Transition metal dichalcogenides
TRIM	Time reversal invariant momenta
UHV	Ultra high vacuum
VdP	Van der Pauw
XRD	X-ray diffraction
XRR	X-ray reflectivity
2D	Two dimensional
2DEG	Two-dimensional electron gas
3D	Three dimensional

Abstract

As a novel class of materials, topological insulators (TI) have been intensively studied since the first theoretical prediction in 2006 [11]. Bi_2Te_3 , Sb_2Te_3 and Bi_2Se_3 compounds were theoretically predicted and experimentally observed as 3D topological insulators, which have a large bulk bandgap, but possess metallic surface states. These spin-polarized surface states have a number of exciting properties such as the spin/momentum locking and suppression of backscattering. The field of TIs leads to potential applications in spintronics and quantum computing, and lots of research efforts are being made.

This dissertation explores the charge-to-spin conversion in topological insulator thin films of Bi_2Te_3 grown by molecular beam epitaxy (MBE). It shows a thickness-dependent spin Hall angle in ultrathin thickness range (3 QL - 10 QL), where QL refers to quintuple layer.

In the first part, we focus on the growth of high quality Bi_2Te_3 thin films by employing molecular beam epitaxy technique. Using *in-situ* and *ex-situ* methods for structural and morphology characterizations, the growth of Bi_2Te_3 thin films is optimized. Then we performed electrical measurement on Bi_2Te_3 thin films to explore the electronic transport properties, and disentangle contributions from the bulk and surface states.

In the second part, we use spin torque ferromagnetic resonance (ST-FMR) to measure spin torques generated by the topological insulator Bi_2Te_3 onto a magnetic layer (permalloy) and calculate the spin Hall angle. We find the value of spin Hall angle reaches maximum at 8 QL Bi_2Te_3 in a thickness range from 3 QL to 10 QL. The ST-FMR measurements are performed both at 300K and at 4K, yielding a larger spin Hall angle at low temperature. The observations suggest significant contributions of the surface states of the TI to the charge-to-spin conversion.

Chapter 1

Introduction

1.1 Topological insulators

1.1.1 Background of topological insulators

Ever since the discovery of atoms and electrons, one interesting field of condensed matter physics was putting together these fundamental particles to form new states of matter. Based on band theory, these ordered states of matter can be classified based on band theory as conductors, insulators and semiconductors. This classification is simple, however, it has been proven to be not sufficient to account for a full description of novel condensed matter systems. A major discovery is the quantum Hall effect in 1980s, which does not fit into this simple paradigm [12].

In the quantum Hall state, the bulk is insulating, while the edges of the material are metallic. This phase is reached when electrons are confined in a two-dimensional slab and subject to a strong magnetic field as shown in Fig. 1.1(a). On the one hand, a chiral charge current can be found along the edge under the magnetic field,

on the other hand, the Hall resistance of the system does not increase linearly with the magnetic field, but shows quantized plateau values in unit of $\frac{e^2}{h}$. The quantization of the Hall resistance can be attributed to a global quantity which does not depend on the details of the system, the so called first-Chern number of the bands located below the chemical potential. Over 40 years of study, the quantum Hall effect has led to a different classification concept based on the topological order.

In order to have quantum Hall state, an essential precondition is that the time reversal symmetry needs to be broken. Nevertheless, if an insulator has time reversal symmetry and an appropriate band gap, another type of topological invariant which is called Z_2 number [13] may exist. Unlike QH state, this system should be described using the spin Hamiltonian, and is the joint effect of charge and spin. Moreover, in QH state the conductance of the edge involves only charge transport. While for a system which has non-trivial Z_2 number, the edge conductances involve both charge and spin transport as shown in Fig. 1.1(c). Therefore, it is called Quantum spin Hall (QSH) phase. This theory was first completed by C. Kane and G. Mele, who further predicted the existence of this phase in graphene and proposed a generalization of the formalism applicable to multiband and interacting systems [14, 15]. They demonstrated that spin-orbit interaction plays an important role in getting the QSH phase. However, since the spin orbit coupling (SOC) in graphene is very small, which results in a band gap in order of 10^{-3} meV, the experimental observation of QSHE in graphene is not realistic.

Shortly after C. Kane and G. Mele's work, A. Bernevig, T. Hughes and S. C. Zhang proposed that QSH state can be realized in mercury telluride-cadmium telluride semiconductor quantum wells [3]. More interesting, they demonstrated the possible topological phase transition in this system by tuning the thickness of the quantum well. These predictions were experimentally verified by L. W. Molenkamp's group who showed that the topological phase is stable when the well

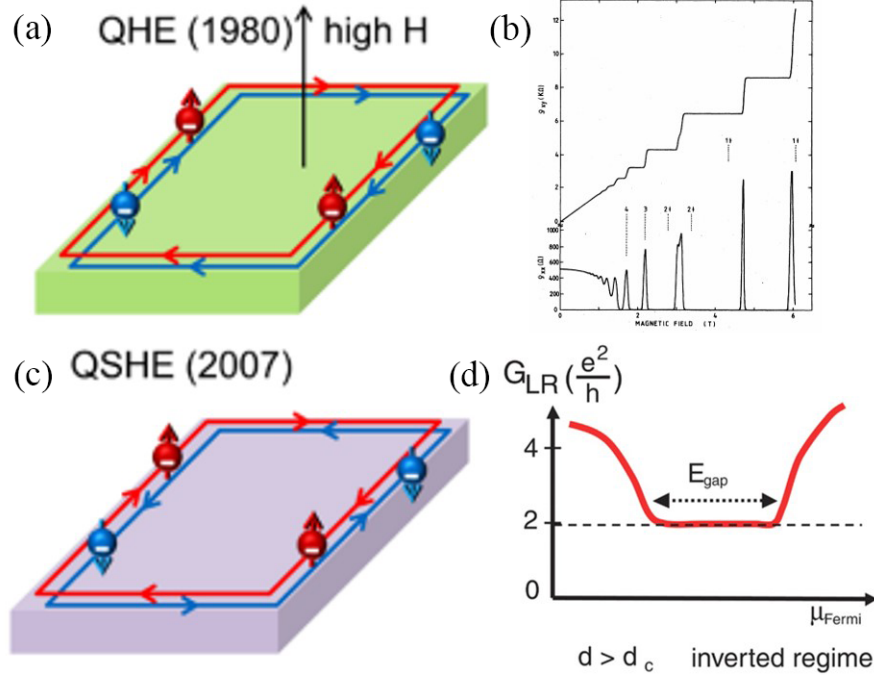


FIGURE 1.1: Schematic figures of quantum Hall effect and quantum spin Hall effect. (a) chiral edge charge current in the QH state [1], (b) quantized Hall resistance [2], (c) a pair of edge spin current in the QSH state [1], (d) The spin-Hall conductance with a plateau value close to $2\frac{e^2}{h}$ [3]. Figures are adapted from Ref. [1–3].

width d is larger than 6.3 nm [16], and that non-dissipative quantum transport occurs through edge channels [17].

In addition to the two dimensional (2D) QH and QSH states, the topological characterization of the QSH effect was soon generalized to three dimensional (3D) insulators by three theoretical groups based on different models [18–20]. This type of insulator is termed as “topological insulator (TI)”. In distinguished to the QSH state which has only one Z_2 invariant, the topological insulator has four Z_2 invariants which differentiate the insulator from “weak” and “strong” topological insulators (TIs). Due to the topological similarity, the QSH and QH states are also regarded as 2D topological insulators. A realistic candidate of the 3D topological insulator phase was predicted to be the $\text{Bi}_{1-x}\text{Sb}_x$ alloy within a certain range of

composition x [21, 22]. It was soon verified by the angle-resolved photoemission spectroscopy (ARPES) measurements which measured the electronic band structure of $\text{Bi}_{0.9}\text{Sb}_{0.1}$ and displayed an odd number of topologically nontrivial surface states [23]. An odd number of crossings lead to topologically protected metallic boundary states [24]. Moreover, simpler versions of the 3D topological insulators: Bi_2Se_3 , Bi_2Te_3 and Sb_2Te_3 compounds, which have a large bulk gap and gapless surface states consisting of a single Dirac cone, were theoretically predicted [25] and experimentally verified [26, 27] in 2009. The discovery of TIs triggered a large number of theoretical and experimental works on searching for TI materials. More TIs are reported afterwards, such as the TlBiSe_2 family [28–31], the KHgSb family [32], BaBiO_3 [33], SmB_6 [34–37] and so on.

1.1.2 Surface states in topological insulators

Formally, lots of properties of TIs can be interpreted in terms of the band structure. For example, one key ingredient of non-trivial topological invariant is the band inversion at time reversal invariant momenta (TRIM) points in first Brillouin zone (BZ). As shown in Fig. 1.2, for a normal insulator with conduction band constructed from the s orbit and valence band constructed from p orbit, the s band has higher energy than the p band and they are separated by the band gap. While for topological insulator, the bands are inverted near the TRIM points, around which the p band has higher energy than s band. For this reason, the states of conduction bands and valence bands are mixed together. This actually provides a good way of understanding the topology in topological insulator. It is impossible for a normal insulator transforming to a topological insulator through continuous deformations which does not open or close a band gap. Although the size of band

gap, the shape of conduction and valence bands can change, they cannot be converted, unless the band gap close first and then open again. Therefore, the NI and TI are topologically different.

Another resultant phenomena of topology is the surface state. If we construct a NI/TI interface, the conduction and valence bands constitution at TRIM will change from s, p in NI to p, s in TI. There must be a critical point when the conduction band and valence band touch with each other. Because of the topology difference, the gapless point can only exist on the interface as shown in Fig. 1.2.

Actually, this gapless point is direct analogue of Dirac electron in high-energy theories and can be described by the massless Dirac equation. It is therefore termed as Dirac cone and is quite robust against perturbations. The appearance of Dirac cone is guaranteed by the time reversal symmetry. The reason can be simply understood in this way:

On the one hand, the energy dispersion satisfies:

$$E(\mathbf{k}, \uparrow) = E(-\mathbf{k}, \uparrow)$$

at TRIM because of crystal translation symmetry. On the other hand, according to time reversal symmetry:

$$E(\mathbf{k}, \uparrow) = E(-\mathbf{k}, \downarrow)$$

Finally, we have:

$$E(\mathbf{k}, \uparrow) = E(\mathbf{k}, \downarrow)$$

where \mathbf{k} is the wave vector of Bloch wave, \downarrow and \uparrow correspond to electron's spin. Therefore, the spin up band and spin down band are degenerated at TRIM points.

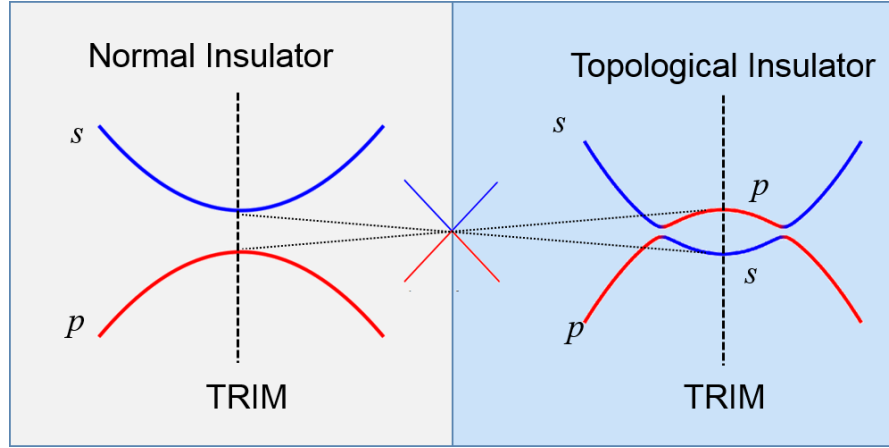


FIGURE 1.2: Schematic figures of band structures of TI and normal insulator. The red and blue colours represent different band components.

The gapless surface state is an important signature of TI surface.

1.1.3 Electronic transport and spin-momentum locking

Apart from the linear dispersion properties of the topological surface state which behaves like a massless Dirac fermion, the spin texture of the Dirac surface state exhibits striking helical nature. As shown in Fig. 1.3(a), above the Dirac point energy, the surface states spins are tangential to the Fermi surface contour with clockwise helicity. In other words, the surface electrons moving in k_x direction have spin polarization directions along $-y$ direction as shown Fig. 1.3(b). While below the Dirac point energy, the electrons moving in k_x direction are locked with the states whose spin polarization direction is along y direction and shows anticlockwise helicity. This phenomenon is termed as spin-momentum locking [38, 39].

The spin-momentum locking can be detected using spin- and angle-resolved photoemission spectroscopy (spin-ARPES) [5, 40, 41], polarized optical spectroscopic techniques [42] or by measuring the hysteresis loops of the in-plane resistance of

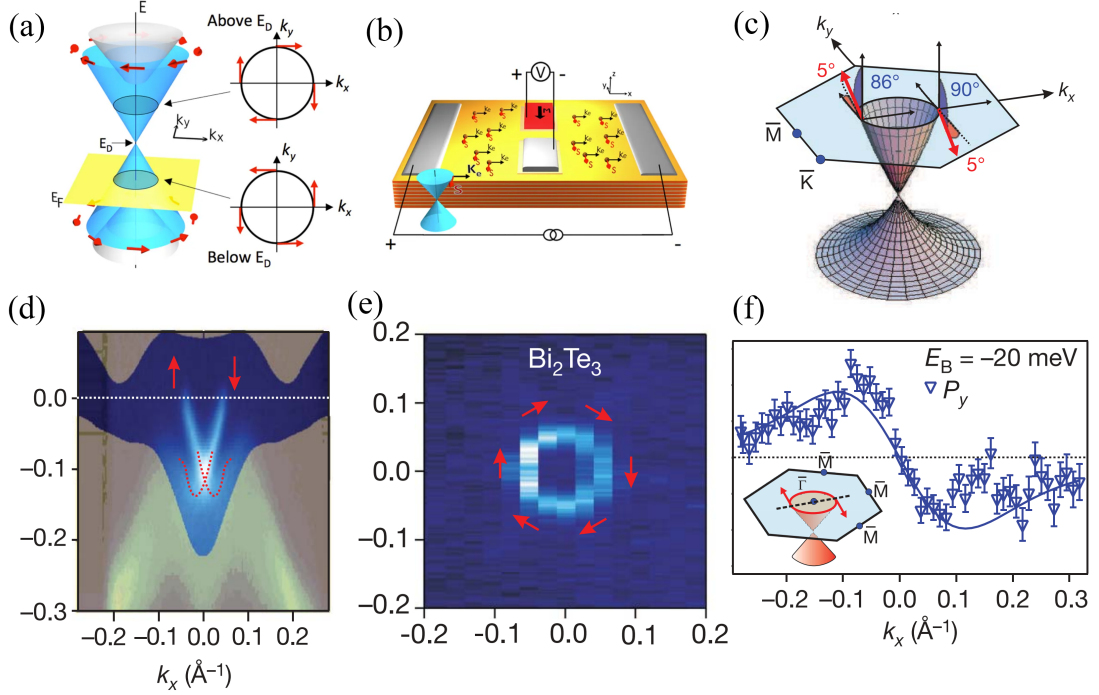


FIGURE 1.3: Spin momentum locking in TI. (a) Schematic diagram of the spin texture [4]; (b) Concept drawing of the transport experiment [4]; (c) Fitted values of the spin polarization vector which demonstrates the topological helicity of the spin-Dirac cone [5]; (d) ARPES dispersion of Bi_2Te_3 along the k_x cut [5]; (e) ARPES intensity map at E_F of the (111) surface of Bi_2Te_3 [5]; and (f) Measured y component of spin-polarization along the $\bar{\Gamma} - \bar{M}$ direction at $E_B = -20$ meV [5]. Figures are adapted from Ref. [4, 5]. The red arrows in the figure represent the spin directions.

the magnetic tunneling junction devices [43–46]. Shown in Fig. 1.3(c)-(f)) are the resultant surface states of Bi_2Te_3 measured by Princeton group. Both the Dirac cone and chiral spin texture are measured. Moreover, the chiral spin texture, as well as the chirality inversion above and below the Dirac point energy, have been explicitly observed in other materials like Bi_2Se_3 , BiTlSe_2 and Sb_2Te_3 [4, 47, 48].

The spin-momentum locking has attracted strong research interests for exploring various spin functionalities in semiconductor heterostructures and topological materials ever since it was predicted. On the one hand, the spin-momentum locking

strongly suppressed the backscattering, resulting in a high conductivity on the surface edge channels. On the other hand, it has been shown that the spin-momentum locking in the surface states of the topological insulators is able to induce a non-equilibrium spin accumulation into the adjacent magnetic layer that switches and manipulates the magnetization of the magnetic layer [49–53].

1.2 Spintronics: spin and charge transport

1.2.1 Fundamental concepts

Spintronics is the area of condensed-matter physics that refers to the study of the role played by electron spin, with the aim of improving the efficiency of electronic devices and to enrich them with new functionalities. In contrast to traditional electronic devices, which involves more charge transport in metals or semiconductors, spintronics specifically exploit spin properties, and thus has the advantages of lower power consumption, less heat dissipation and non-volatile.

The prototypical spintronic devices that have been used in industry, such as a read head and a memory-storage cell contain:

- 1). Spin valve which consists of two ferromagnetic (FM) layers separated by a non-magnetic (NM) metal layer like Cu.
- 2). Giant magnetoresistance (GMR) devices, designed as a repeated extension (superlattice) of spin valve, consisting of alternating FM and NM layers.
- 3). Magnetic tunnel junctions (MTJ) which consist of two FM layers separated by thin oxide insulating layer of oxide.

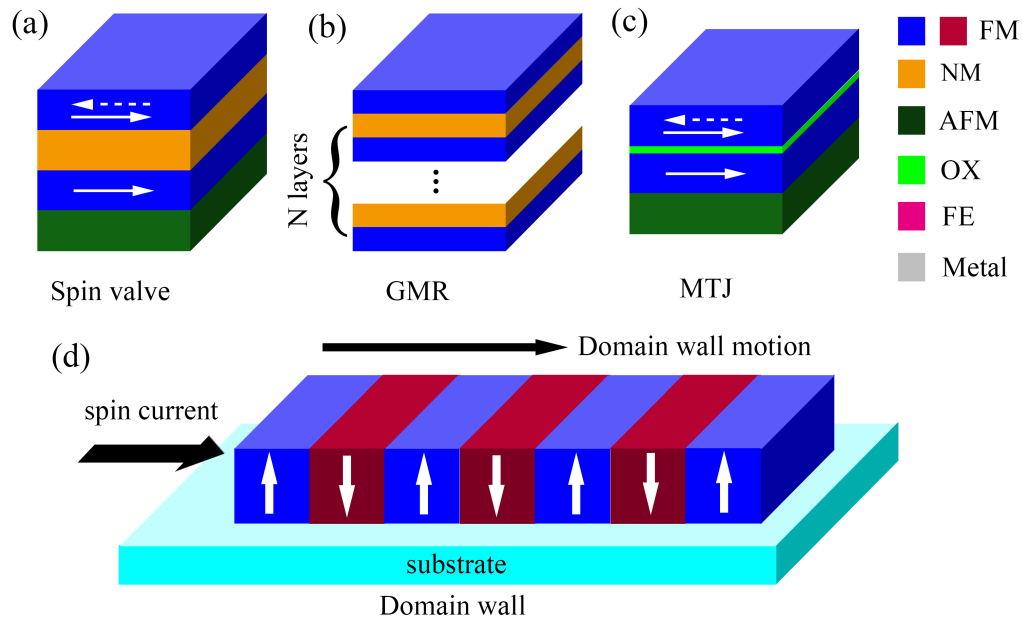


FIGURE 1.4: Schematic figures of prototypical spintronic devices. (a) Spin valve (b) GMR (c) MTJ and (d) racetrack

4). Domain wall motion in magnetic nanowires driven by spin-polarized charge current.

Despite the diversity of the spintronic devices, current effort mainly focus on two different approaches. The first is to improve the existing GMR-based technology, such as, developing new materials which has large spin polarization or improving the spin filtering ability of existing devices. The second one is to find better ways of generating and utilizing spin-polarized currents. Among these approaches, the spin transport in semiconductors has attracted increasing research interests. Compared with the metal-based devices, semiconductors have special advantages, for example, to amplify signals, to sustain less heat dissipation due to less charge transport, and being easier to be integrated with traditional semiconductor technologies.

While there are clear advantages for introducing semiconductors to novel spintronic applications, there are still questions pertaining to understand the spin transport in semiconductors and find good material candidates. Due to the strong SOC and spin-momentum locking properties of TI, a natural question is whether the TI is a good candidate for a spin-current generator. The answer turns to be positive, verified by lots of studies both experimentally and theoretically. However, in spite of many recent research efforts, there are still questions that need to be answered like the transport behavior of TI in combination with other materials, or whether the surface states survive after deposition of adjacent layers in TI heterostructures. In this thesis, we aim to study TIs interfaced with magnetic materials, and to find out signatures of surface states combining electrical transport and spin torque experiments. The fundamental concepts to understand spin torques will be described in the following sections.

1.2.2 Spin Hall effect and inverse spin Hall effect

Among the several possibilities of generating and controlling the spin currents, the spin Hall effect (SHE) has become a widely used strategy nowadays. It is described as the phenomenon of spin accumulations along the edges of a nonmagnetic conductive wire while a charge current passing through, as shown in Fig. 1.5(b). In comparison to the Hall effect (HE) and anomalous Hall effect (AHE), which concentrate on the charge accumulation along the edges and need either the external magnetic field (HE) or internal magnetic moments (AHE) to break time reversal symmetry, the SHE results in a pure spin current and does not need a broken time reversal symmetry (TRS), as illustrated in Fig. 1.5(a).

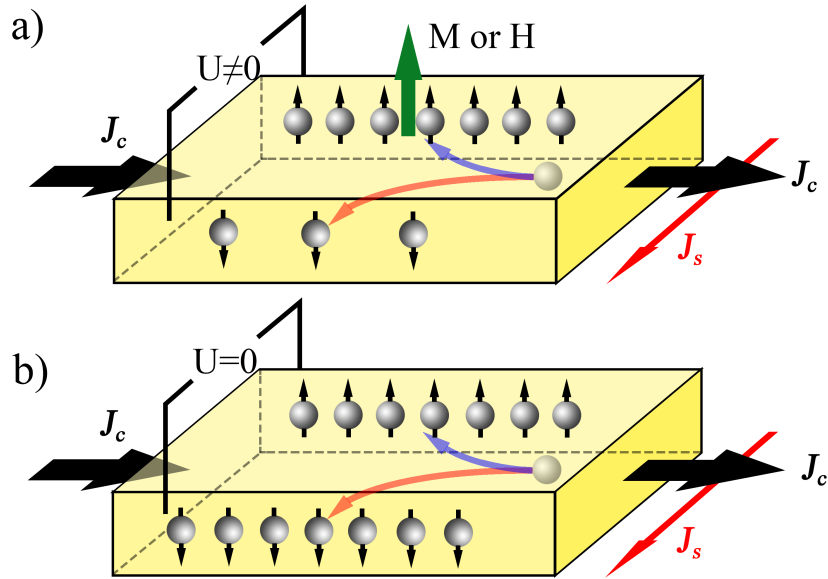


FIGURE 1.5: Schematic figures describing the (a) anomalous Hall effect and (b) spin Hall effect.

Although SHE was only observed less than twenty years ago [54, 55], it has deep roots in the history of electricity and magnetism. In 1929, in order to provide direct evidence that spin is an intrinsic property of the free electrons, Mott proposed his double-scattering experiment [56]. In his proposal, if an unpolarized electron beam falls on two targets with heavy nuclei and scattered successively, an asymmetric deflection of the electron beam after the second scattering will occur. This asymmetric deflection arises because the electron beam becomes spin polarized after the first scattering. Therefore, to some extent, the Mott-scattering can be regarded as the SHE in a non-solid-state environment. It was not until in 1971 when Mikhail Dyakonov and Vladimir Perel [57] of the Ioffe Institute in Leningrad proposed the existence of SHE in semiconductor. In their proposal, they refer to the extrinsic part of the SHE, which is originated from the scattering of electrons.

In solid-state systems, on the other hand, the electrons can also feel the spin

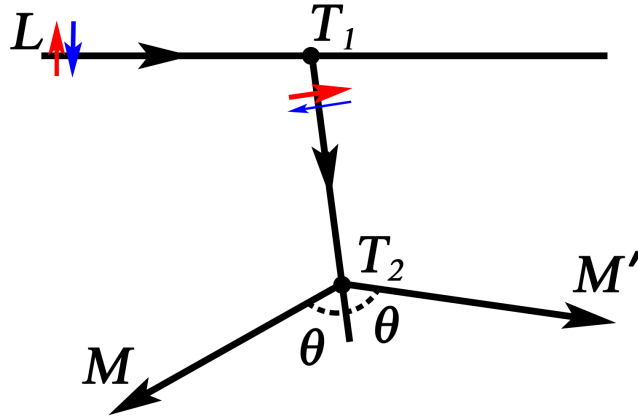


FIGURE 1.6: Schematics of Mott scattering. An unpolarized electron beam is injected along LT_1 direction and scattered by the first target T_1 . Then the electron beam is scattered by the second target T_2 and finally detected by two detectors, M and M' , which are set symmetrically. If the electron beam is unpolarized after the first scattering, the two detectors will get the same amount of electrons. Otherwise the electron beam is polarized after the first target.

orbit field of a perfect crystal even in the absence of scattering. This fundamental physics principle gives rise to another part of SHE which is clearly distinct from the Mott scattering of the free electron beam. Since this part of SHE can be directly derived from the relativistic band structure of a material, it is termed as intrinsic SHE. The intrinsic SHE was experimentally predicted by Sinova et al [58] and Murakami et al [59] and then soon verified by Wunderlich et al [55, 60] based on the circularly polarized luminescence experiments. These discoveries soon triggered an intensive research of SHE based on optical methods [61–66].

Heuristically, if we go back to Mott-scattering effect again, another branch of transport phenomenon in solid-state can be found. According to Mott's calculation, if the polarized electron beam falls into the second target and is scattered, the electron beam will be deflected asymmetrically. Similarly, what will happen if a polarized spin current are injected to a metal? Hirsch gave his answer in

1999 [67]. He proposed that, in this case, the electrons with spin up will be scattered preferentially in one direction perpendicular to the flow of current, and spin down preferentially in the opposite direction. A Hall voltage will be generated at the edges of the metal because of the transverse charge imbalance. This Hall voltage was soon measured by different groups [68–70] and this effect is named as inverse spin Hall effect (ISHE). The ISHE is very attractive not only because of its importance as a fundamental transport phenomena in solid-state physics but also due to its potential applications in electrical spin detection. It is gradually becoming a standard measurement tool for pure spin current, having impact on a lot of research studies [71–75].

1.2.3 Spin transfer torque

Ever since the discovery of the GMR effect, there is considerable interest in the study of multilayered heterostructures which consist of magnetic and nonmagnetic metals or insulators. Recently, the transport properties of these multilayers and thin films have been widely investigated and have revealed interesting properties resulting from the joint effect between electron transport and magnetic behavior.

It is known that when an unpolarized charge current passes through a ferromagnetic film, there are two possible processes as shown in Fig. 1.7(a). For the first one, the spin-up and spin-down electrons that build up the current have different transmission probabilities. The transmission probability depends on the magnetic order of the film. The electrons which have the opposite spin direction to the local magnetic moment in the film have lower transmission probability and thus may be reflected backwards. In the second process, there are spin-flip collisions between the electron beam and the magnetic moment in the film. Part of the electrons flip their spin direction to the same as the local moment after the collisions [76, 77].

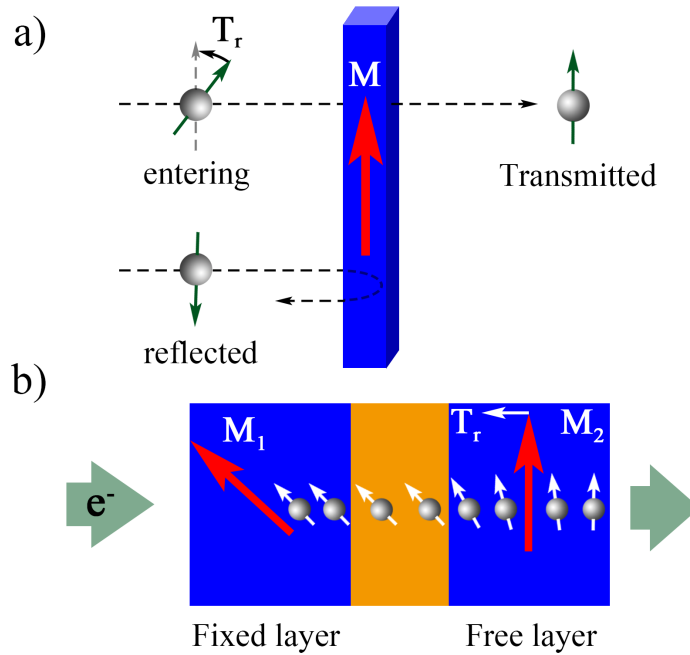


FIGURE 1.7: Schematic of spin transfer torque. (a) An unpolarized electron beam is polarized after passing through a magnetic film, either through a spin-flip collision or through the backscattering and (b) spins of electrons in the multilayered hetrostructures.

For both cases, the charge current becomes polarized. Specifically, the second process means that there is a transfer of angular momentum from the ferromagnet to the electrons. Since angular momentum is conserved, there must be an equal amount of angular momentum from the electrons to the ferromagnet. This effect is called spin transfer. The torque which rotate the spin direction is therefore called spin transfer torque (STT).

On the other hand, for a typical STT device which consist of two ferromagnetic layers and separated by a spacer layer as shown in Fig. 1.7(b), the spin transfer also holds and has more practical applications. In this heterostructure, the fixed layer has its magnetization fixed along M_1 direction, whereas the magnetic moment M_2 in the free layer is free to move. When an charge current is injected through the heterostructure, the electrons' spins are first polarized along M_1 direction due to

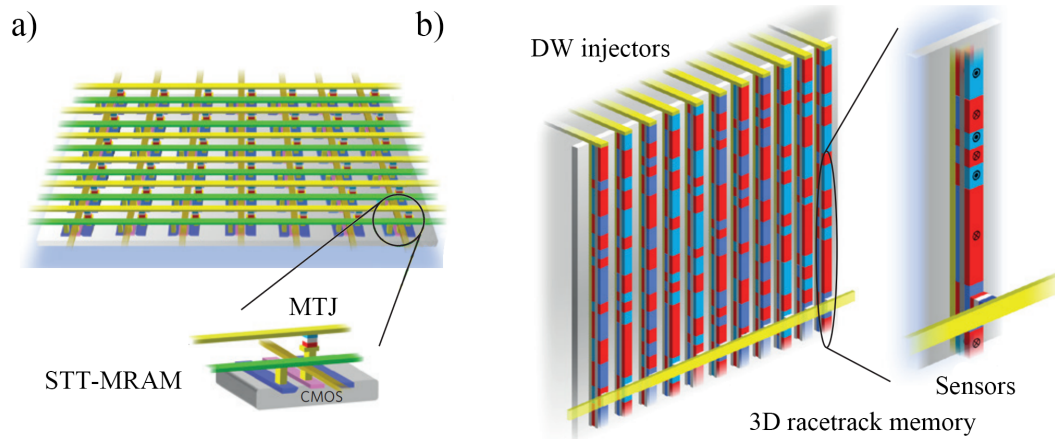


FIGURE 1.8: Schematic of (a) STT-MRAM and (b) racetrack Memory. Figures are adapted from Ref. [6].

spin transfer and then propagate to the free layer. If M_1 is not aligned with M_2 direction, the polarized spins will then align with M_2 because of exchange interaction. During the process, the change of conduction electrons' angular momentum has to be offset by the change of free layer's angular momentum as a result of conservation of angular momentum. Thus the magnetic moment suffers from a torque which rotate it towards to M_1 direction. Notably, the aforementioned torque could result in two qualitatively different types of magnetic behaviors in the free layer, either simply switching the magnetic orientation from M_2 to M_1 or exciting a dynamical state where the magnetization undergoes steady-state precession [78, 79].

Although the STT was first considered in the late 1970s by Berger [80], it did not attract much attention. The most influential paper work which launched the widely study of STT came in 1996 by Slonczewski [81] and Berger [82]. This effect was soon confirmed experimentally and observed around 2000 by different groups [83–85]. The STT effect is exciting because it allows for the efficient manipulation of magnetic configurations without the assistance of external fields, which

is good for downscaling of devices. It has triggered the study and commercialization of spin-based technologies, for example, the racetrack memory, which is based on current-driven domain wall motions, proposed by Parkin [6] and the current-controlled magnetoresistive random access memory (STT-MRAM) as shown in Fig. 1.8.

1.2.4 Spin orbit torque

Another setup that can also exhibit current-induced magnetization dynamics is illustrated in Fig. 1.9. In contrast to the STT devices which use a fixed layer of ferromagnet to generate the polarized current, this setup is based on the effective spin polarization originating from SOC of a nonmagnetic material. When charge current passes through the nonmagnetic material, the spin will be polarized due to the effective field and a transverse spin current will be generated [86]. Similarly to STT, the spin current can be injected to the FM layer and introduce spin torque in the FM layer. Since this spin torque is generated through SOC, it is called spin orbit torque (SOT). Normally, the nonmagnetic materials which are used to fabricate the SOT devices can be classified into several categories:

- 1). Heavy metals or bulk semiconductors, such as Pt [87], β -Ta [88], GaAs [89]. Generally speaking, the spin current is induced by two effects in heavy metals. The first one is the SHE effect mentioned in the previous section. The second one is the interfacial spin-orbit effects such as the Rashba-Edelstein effect (REE) which is also called inverse spin galvanic effect. Usually, interfaces between a heavy metal and nonmagnetic materials or 2D electron gases are able to generate a momentum-dependent Rashba spin-orbit field originating from an asymmetric bonding at the interface. This Rashba spin-orbit field leads to the REE. According to the REE,

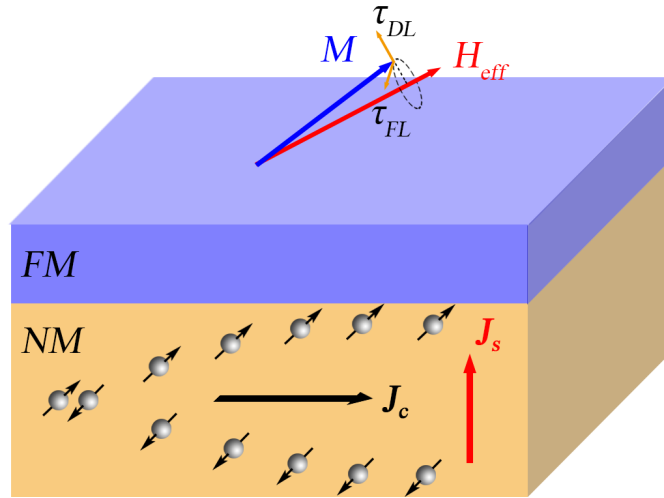


FIGURE 1.9: Schematic of SOT setup. When a current is flowing through the NM layer, a transverse spin current is generated and injected to the FM layer. The torque on the local magnetic moment in the FM layer can be split into two components: τ_{FL} , which drives the moment into precession around the effective magnetic field, and τ_{DL} , which acts to bring the moment back to its equilibrium position.

a nonequilibrium spin polarization can be achieved through an electrical current in systems lacking inversion symmetry [90].

2). Topological insulator, such as Bi_2Se_3 [49, 91], $(\text{Bi}_{0.5}\text{Sb}_{0.5})_2\text{Te}_3$ [51], in which electrons' spin orientation is locked relative to its propagation directions because of the topological surface states. Such spin-moment locking gives rise to a nonequilibrium surface spin accumulation during the flow of charge current. It is conceptually similar to the Rashba-Edelstein effect in non-topological materials.

3). Weyl Semimetal, such as WTe_2 [92]. The Weyl semimetal is a new state of topological quantum matter which has been found recently. Pairs of linear dispersion points, named as Weyl fermion, can stably exist in its band structure. A number of novel properties have been observed in these topological semimetals, such as large magnetoresistance (MR), high carrier mobility, negative MR. Especially,

there exist unclosed surface states, which are called Fermi arcs, connecting the projections of the Weyl points with opposite chirality on the surface of the Weyl semimetal [93]. More importantly, it has been suggested that the Fermi arcs are also spin-polarized with similar spin-momentum locking effect as having been observed in the surface states of TIs [92, 94–96]. This spin-momentum locking will also give rise to a non-equilibrium spin accumulation while injecting an charge current.

4) Atomically thin transition metal dichalcogenides (TMDs), such as WTe_2 [97], MoS_2 [98], WSe_2 [99]. The TMDs are 2D materials which have only the interfacial spin-orbit effect. It was reported the SOT generated by TMDs is dominated by the in-plane component and it turns out to be almost temperature-independent [99].

1.3 Motivation and outline

The need for energy-efficient computing nowadays is more urgent than ever before, covering various domains such as large-scale sensor networks, Internet of Things, bioelectronics, and neuromorphic/neuro-inspired computing. With the dramatic increase in device counts to meet the modern system requirements, it is critical to develop a building block with fundamentally different computing and storage mechanisms. Non-volatile switches with novel computing mechanisms are considered as the most promising solution to overcome the energy brick wall. Among them, spin-based technologies have advantages of non-volatile memory and logic owing to their supreme features of low-voltage (sub-mV), high-speed operation (sub-ns), and high endurance (over 10^{12} cycles).

In order to fulfill these needs, we are motivated to search for materials to provide more efficient current-induced torques. Recent experiments have demonstrated large spin-orbit torques in TIs due to the fact that an electron's spin orientation is locked relatively to its propagation direction in the surface states of TIs. Such spin-momentum locking gives rise to a non-equilibrium surface spin accumulation while flowing a charge current. If this spin accumulation couples to an adjacent magnetic film, the resulting flow of spin angular momentum will exert a spin torque on the magnet.

This thesis is structured as follows: In chapter 2, we introduce the ultra high vacuum (UHV) technology and MBE as the experimental setup for sample preparation, followed by the introduction of characterization methods. In chapter 3, we discuss the epitaxial growth of topological insulator Bi_2Te_3 thin films. Chapter 4 and 5 contain results for the electronic transport measurements and spin torque ferromagnetic resonance measurements. Chapter 6 summarizes that the surface contribution is dominant in the charge-to-spin conversion in Bi_2Te_3 thin films and suggests for future work.

Chapter 2

Experimental Instruments and Techniques

The deposition of topological insulator thin films was carried out in a MBE growth chamber with a base pressure of 8×10^{-11} mbar. To optimize the growth recipe, reflection high-energy electron diffraction (RHEED), x-ray techniques and atomic force microscopy (AFM) were employed for the structural characterization. In the following, these techniques will be briefly introduced.

2.1 Ultra high vacuum technology

UHV is the vacuum regime characterized conventionally by a pressure better than 10^{-9} mbar (1 mbar=100 pa). Surface science experiments require a chemically clean sample surface with the absence of any unwanted adsorbates. Our experiments were performed under a vacuum of the order 10^{-10} mbar or better. To give an idea of the absorption rate of residual molecules in the chamber, we shall

perform a rough estimation. At room temperature ($T \approx 293$ K) with the sticking coefficient assumed to be unity, the time constant to form a monolayer on the surface from the gas phase is about one hour when the pressure is 10^{-9} mbar. Thus, to keep the sample clean and study the intrinsic physical properties, the usage of UHV is absolutely necessary. On the other hand, the mean free path of the gas molecule is much greater than the typical dimensions of the vacuum chamber when the vacuum is better than 10^{-9} mbar, which is the ideal scenario for MBE growth. In this section, we are going to introduce UHV technology and mainly focus on how to obtain and maintain the vacuum in the chamber [100–102].

A pumping system is normally composed by pumps, gauges and valves. Fig. 2.1 is a typical UHV pumping system. To pump down the system from atmospheric pressure (1013.25 mbar) to UHV (10^{-10} - 10^{-11} mbar), the pressure needs to be changed by ~ 13 - 14 orders of magnitude, which is beyond the pumping capacity of any single pump. So, the pumps for a UHV system often consist of scroll pumps, turbomolecular pumps, ion pumps and titanium sublimation pumps. Scroll pumps are widely used for initially pumping the system from atmospheric pressure down to about 10^{-2} - 10^{-3} mbar. The principle of the operation of scroll pumps is illustrated in Fig. 2.2(a). Two interleaved spiral-shaped scrolls are used to pump gases. One of the scrolls is fixed, while the other orbits eccentrically without rotating, thereby trapping and pumping fluids between the scrolls. It is noteworthy that scroll pumps are oil free, which can avoid oil vapor backstreaming and prevent the whole vacuum system from contamination.

A turbomolecular pump consists of a stack of rotor and stator blades (Fig. 2.2(b)). When the blades are rotated at very high speed (> 10000 rpm), the gas molecules are hit and led towards the exhaust connected to the foreline. The operating range of turbomolecular pumps is from 10^{-2} - 10^{-10} mbar, so they cannot work

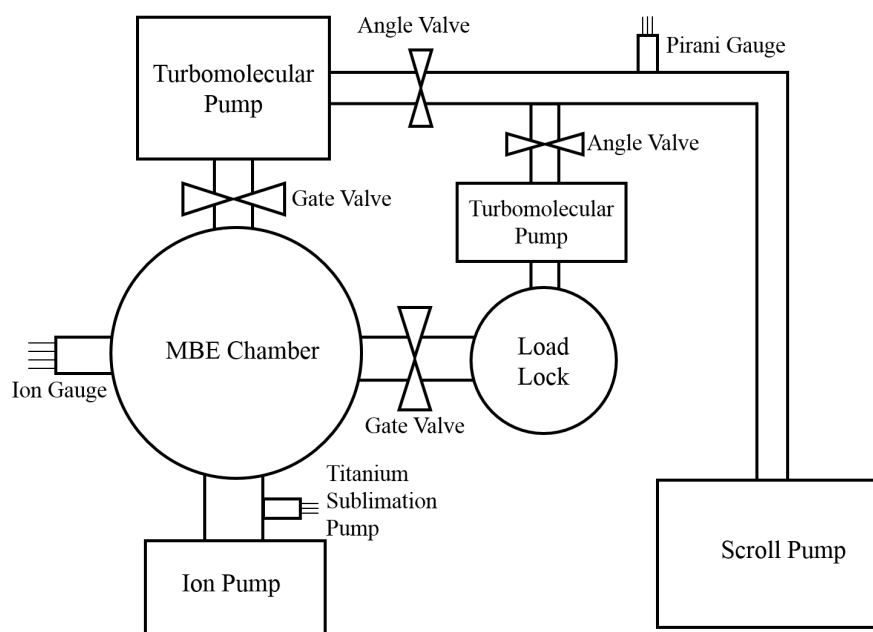


FIGURE 2.1: Schematic diagram of a routine UHV pumping system for a typical MBE machine.

at atmospheric pressure, thus a scroll pump is conventionally used as a backing pump.

Ion pumps and titanium sublimation pumps are often used together and connected directly to the UHV chamber. The basic mechanism of both pumps is the generation of titanium atoms inside the vacuum chamber. The gases react with the fresh Ti film to form non-volatile compounds. Ion pumps are the most popular UHV pumps. The working principle is shown in Fig. 2.2(c). The main components of an ion pump are anode (a stack of stainless steel tubes), cathode (Ti plates mounted close to the two open ends of anode) and a magnet. By applying a DC voltage of 3-7 kV between the cathodic plates and anodic tubes (Penning trap), electrons are emitted from cathodic plates and move along helical trajectories in the anodic tubes, then the molecules are ionized and accelerated. Stroked by the ionized molecules, titanium is sputtered. The fresh Ti film coats the tubes with strong

sorption ability. Ion pumps help to reach the 10^{-11} mbar level, which is perfect to maintain UHV together with the advantages of cleanliness, long operation life, vibration-free operation etc. Titanium sublimation pumps are usually used as a plus to ion pumps. The structure of a titanium sublimation pump is shown in Fig. 2.2(d), titanium is sublimated from the Ti-covered filament heated by passing through a high electrical current (typically around 40 A) continuing a short time (1 minute). Ti film coats the surrounding chamber walls and reacts with the residual gas to improve the vacuum quickly. However, it cannot work continuously since the Ti film will not be clean anymore and the sorption capacity is reduced after some time. Usually, it needs to be re-heated after a certain time manually or with an automated program.

In addition to the pumping system, gauges are needed to read the pressure of the vacuum system. Like pumps, there is no universal gauge that is able to work along the whole range from atmospheric pressure to UHV. Different gauges are chosen depending on the chamber pressure. Mechanical gauges are usually used to check whether a vacuum exists at all, but they are not necessary in a UHV system. Pirani gauges operate in the range of 10^{-3} mbar, which are mostly used in foreline monitoring. Ionization gauges are the basic instrument to measure pressures lower than 10^{-4} mbar. The most widely used one is the hot-filament ionization gauge by using thermionic emission of electrons from a hot filament. The electrons are accelerated to the grid at a DC potential of about +150 V. These electrons collide with gas molecules and ionize them. The ionized gases are attracted to the central-situated ion collector, such that the resulting ion current is proportional to the amount of gas molecules on the chamber, being indicated as pressure reading. Strictly speaking, ion gauge measurement depends on the gas composition, because the ion current differs for different gases at same pressure. In practice, they are calibrated for nitrogen.

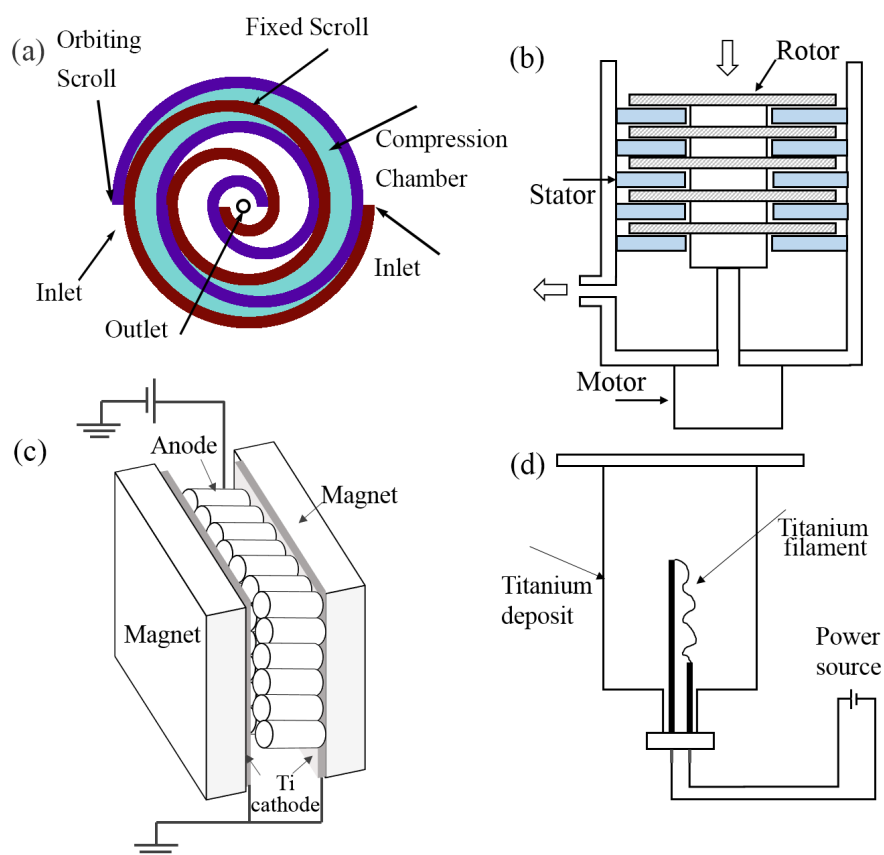


FIGURE 2.2: Schematic diagrams of designs and operations for (a) scroll pump; (b) turbomolecular pump; (c) ion pump and (d) titanium sublimation pump.

Besides pumps and gauges, valves also play a key role in the vacuum system. Sometimes, one needs to isolate one section of a vacuum system from another one. For example, the valve connecting the sample preparation chamber and sample loading chamber (load lock) needs to be closed to keep the UHV in the preparation chamber. The most common valves are angle valves and gate valves. The usage of the valves can be found in Fig. 2.1.

So far, a UHV pumping system can be built with all the above components, but there are additional hints to obtain and preserve a good vacuum. It is worthy to learn the aspects that can affect the vacuum. The two main issues are leaks and

degassing, which are typically originated from desorption of gases on the surface, diffusion of gas inside materials, penetration of atmosphere and vapor pressure of the materials etc. Therefore, it is important to choose the materials which are less prone to mechanical leaks while designing a UHV system. Normally, the material for the chamber body is 304 stainless steel and the flanges are connected by using copper gaskets. For the construction of evaporators and sample holders, the common materials are tantalum, tungsten and molybdenum. These materials not only have low vapor pressures, but are able to endure chamber bakeout, and additionally can sustain very high local temperatures ($> 1000\text{ }^{\circ}\text{C}$). The chamber bakeout is an essential step to reach a desired vacuum. Once the system is exposed to air, the surfaces of the inner walls and components within the chamber(s) will be covered by water, nitrogen, oxygen and other atmospheric gases. When the system is pumped down again, desorption of the adsorbed gases is very slow at room temperature which hampers the achievement of a good vacuum. If the whole UHV system is heated to a higher temperature, gas desorption can be accelerated and, hence the gas coverage on the surface will be decreased tremendously. Afterwards, the system is cooling down to room temperature and the desorption rate is reduced as well as less residual gases are left over in the chamber. As a result, lower base pressures can be obtained. Typically, the system is baked at $150\text{ }^{\circ}\text{C}$ - $250\text{ }^{\circ}\text{C}$ for 24-48 hours, which is sufficient to reach the expected vacuum. Additionally, some of the evaporators could reach a high temperature at working mode, which also affects the vacuum, so it is prerequisite to install cooling water for the evaporators with evaporation temperatures above $400\text{ }^{\circ}\text{C}$, and recommended for those below $400\text{ }^{\circ}\text{C}$. The purpose is to reduce local degassing and maintain the vacuum during growth.

2.2 Molecular beam epitaxy

MBE [101–104] is a versatile technique for growing high-quality epitaxial thin films, which is applicable for a wide material range, such as semiconductors, metals or insulators. In MBE, the constituent elements for the film growth are delivered to the substrate surface using molecular or atomic beams which are evaporated from a typically solid or liquid source. The substrate is kept at an appropriate elevated temperature, which means that, on the one hand, it ensures the migration of the atoms over the surface, on the other hand, it should not be too high to induce agglomeration (clustering) or diffusion intermixing into the substrate or adjacent layers when growing multilayer compounds. It plays a key role in epitaxial growth to choose the proper type of substrates and prepare them chemically and/or thermally to ensure a homogeneously clean and flat surface.

In comparison to other deposition techniques, MBE has several advantages. First, MBE growth is carried out in a UHV environment which can greatly lower the impurity level to get high purity epitaxial thin films. Secondly, the growth rate is low and beam fluxes can be precisely controlled, which ensures that the surface migration of atoms or molecules and the composition of the grown epilayer can be tuned with atomic resolution. Moreover, MBE growth proceeds at conditions far from thermodynamic equilibrium and is governed mainly by the kinetics of the surface when the impinging molecular beams react with the outermost atomic layers of the substrate crystal. This allows the growth of some materials which can hardly grow at conditions near thermodynamic equilibrium. Furthermore, due to the UHV environment and the compatible geometry of standard MBE chamber, RHEED can be employed for *in-situ* monitoring the crystalline quality of deposited films. The more detailed information about RHEED is referred in the following section.

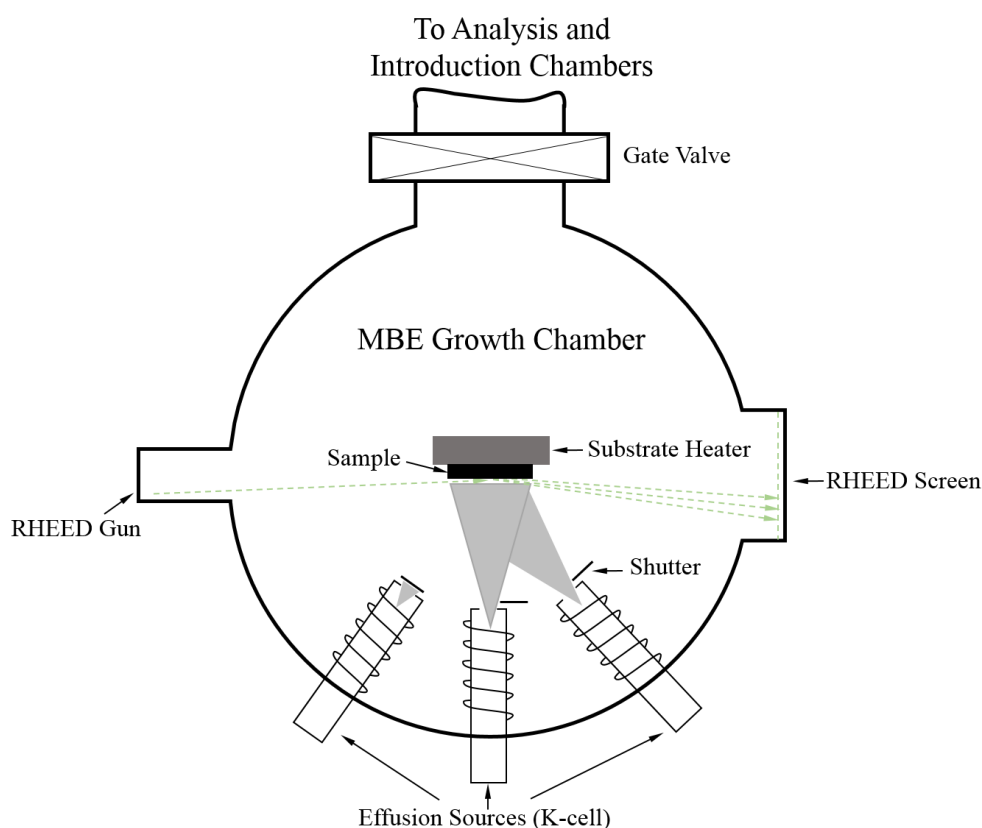


FIGURE 2.3: Schematic diagram of a simple MBE chamber showing the effusion cells, shutters, substrate heater and RHEED system.

Fig. 2.3 depicts a typical MBE chamber. The essential elements are effusion cells, substrate heating assembly and RHEED system. The typical effusion cell used in MBE is Knudsen effusion cell (K-cell) (Fig. 2.4). An important part of the K-cell is the crucible, where the beam fluxes are evaporated from solid or liquid materials. The crucibles are often made by Pyrolytic Boron Nitride (PBN), sapphire (Al_2O_3), graphite or quartz. Due to the temperature requirements and potential reactions between materials, it depends on the deposition materials for choosing different types of crucibles. In a K-cell, the crucible is heated by metal wire (W or Ta wire) to reach the desirable temperature. At the bottom of the crucible, a thermocouple is loaded to measure and monitor the cell temperature.

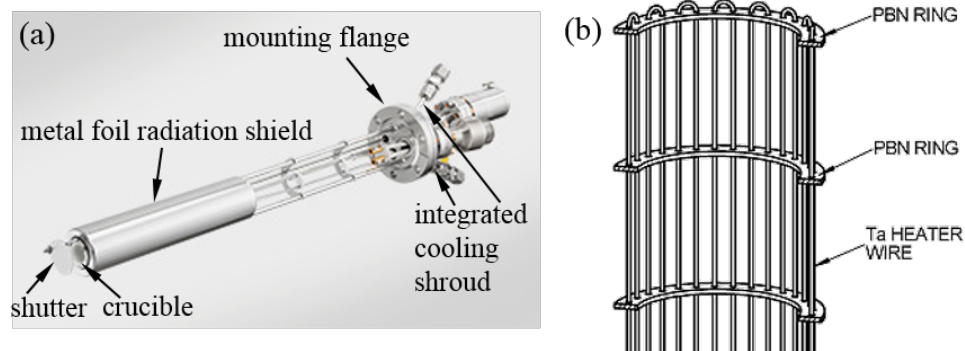


FIGURE 2.4: (a) A standard K-cell (MBE-Komponenten GmbH, WEZ 40-10-22-KS), (b) schematic of the wire heating assembly.

In addition, radiation shields are surrounded to improve both temperature stability and thermal efficiency. It is recommended to install cooling water for all evaporators while it is a must for evaporators working at high temperatures. This can prevent the generation of unwanted outgassing from high-temperature parts. The maximum operating temperature for K-cells is reported to 1900 °C by our manufacturer (MBE Komponenten) which can satisfy the requirements for most materials. For the materials with higher evaporating temperatures, i.e. Mo, Nb, Ta, W, etc. electron beam evaporation is employed. The basic principle is that an electron beam is generated from a filament and the beam strikes source material by the application of a high voltage towards the source. Thereby, the surface atoms will have sufficient thermal energy to evaporate. The highest temperature at local points can reach up to 2500 °C.

Another important part in MBE chamber is the substrate heating assembly. There are two conventional methods to heat substrates, direct current heating and radiative heating, respectively. For conductive substrates, they can be heated by direct current and the temperature can be measured by infrared thermometer (pyrometry) which can read the temperature directly on the sample. On the other hand, insulating substrates are transparent in this optical range, which makes errors

by measuring temperatures with infrared thermometer. As a result, insulating substrates are always heated via radiation and the temperature is measured by thermocouple. As thermocouples cannot be mounted on the samples but on nearby surface, the measured temperature is not the real temperature on the sample and it always has an offset and a temporal hysteresis for reflecting the temperature change of the samples. In our case, the most often used substrates are insulating materials, so one should keep in mind for the hysteresis of temperatures during optimizing the growth recipe for thin films.

2.3 Structural characterizations

2.3.1 Reflection high energy electron diffraction

It is important to characterize the structural and surface quality of thin films to optimize the parameters of thin film growth. In MBE growth setup, RHEED is a very powerful technique with high surface sensitivity to gain information of the surface quality, as well as to monitor real time growth of thin films [105]. Unlike most structural characterization tools, RHEED is always built inside MBE chamber and the glancing-incidence-angle geometry of RHEED offers the advantage that it will not affect the growth procedure while monitoring the quality of epitaxial growth of thin films. Without RHEED, we are blind to the quality of the film during growth and can only do *ex-situ* characterizations after the sample is taken out of the chamber. This would be a time consuming effort to get feedback for film growth optimization. Therefore, RHEED is the most widely used *in-situ* analytical tool in MBE. We would like to briefly present the principle of RHEED operation hereinafter.

The RHEED setup in a MBE system is shown in Fig. 2.3. A RHEED system requires an electron gun and a detector. From the electron gun, the electron beam is emitted with a primary energy E ($1 \text{ keV} < E < 30 \text{ keV}$) and guided by electromagnetic lenses. The electron beam is incident at a small glancing angle (about $1^\circ - 2^\circ$) relative to the sample surface, from where the electrons undergo diffraction owing to the crystalline lattice of the substrate or the film. With the help of phosphor detector screen, the diffraction patterns can be collected and digitally imaged by a charge-couple-device (CCD) camera, which is transferred to the computer for analysis using commercial software. Due to the small incident angle, electrons do not penetrate into the bulk of the material, but only get diffracted by very few atomic layers at the surface.

Fig. 2.5(a), (d) and (g) show electron diffraction from three different crystalline materials, respectively. These collected diffraction patterns, which are related to the intersection of Ewald sphere with the reciprocal lattice rods, reflect the crystal structures and surface quality.

2.3.2 Complementary *ex-situ* characterizations

Besides *in-situ* monitoring of the film deposition, we also check the quality of MBE-grown Bi_2Te_3 films with *ex-situ* methods. Atomic force microscopy (AFM) and x-ray techniques were employed to investigate the surface morphology and crystalline quality.

The basic application of AFM as a microscopic technique is to measure the topography of a sample at the nanometer scale. There are various operating modes, depending on the applications, which are described as contact, tapping mode and non-contact modes. Among those modes, contact mode is the simplest one, which

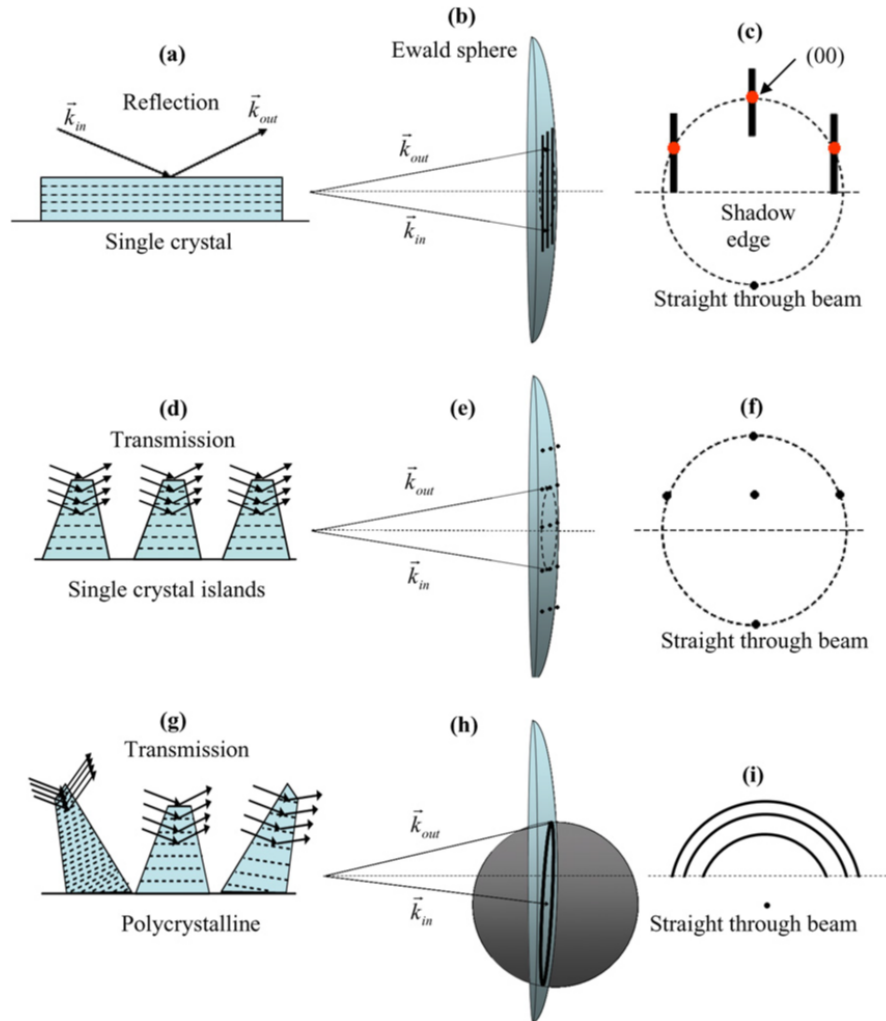


FIGURE 2.5: Schematics of electron diffraction geometries, film morphologies, and crystalline structures for:(a) A single crystal. (d) Single-crystal islands. (g) Polycrystalline islands. Corresponding Ewald sphere constructions are seen in b, e, and h and corresponding RHEED patterns in c, f, and i. Figures are adapted from [7].

is applied in our investigation. The working principle of the contact mode is described basically in the following. A sharp tip attached to the end of a cantilever scans across the surface of the sample, the position of which is finely controlled by the cantilever displacement using piezoelectric actuators. The laser beam is reflected on the top of the cantilever and collected by a photodiode detector with an output signal amplified and correlated to the height profile of the sample's surface.

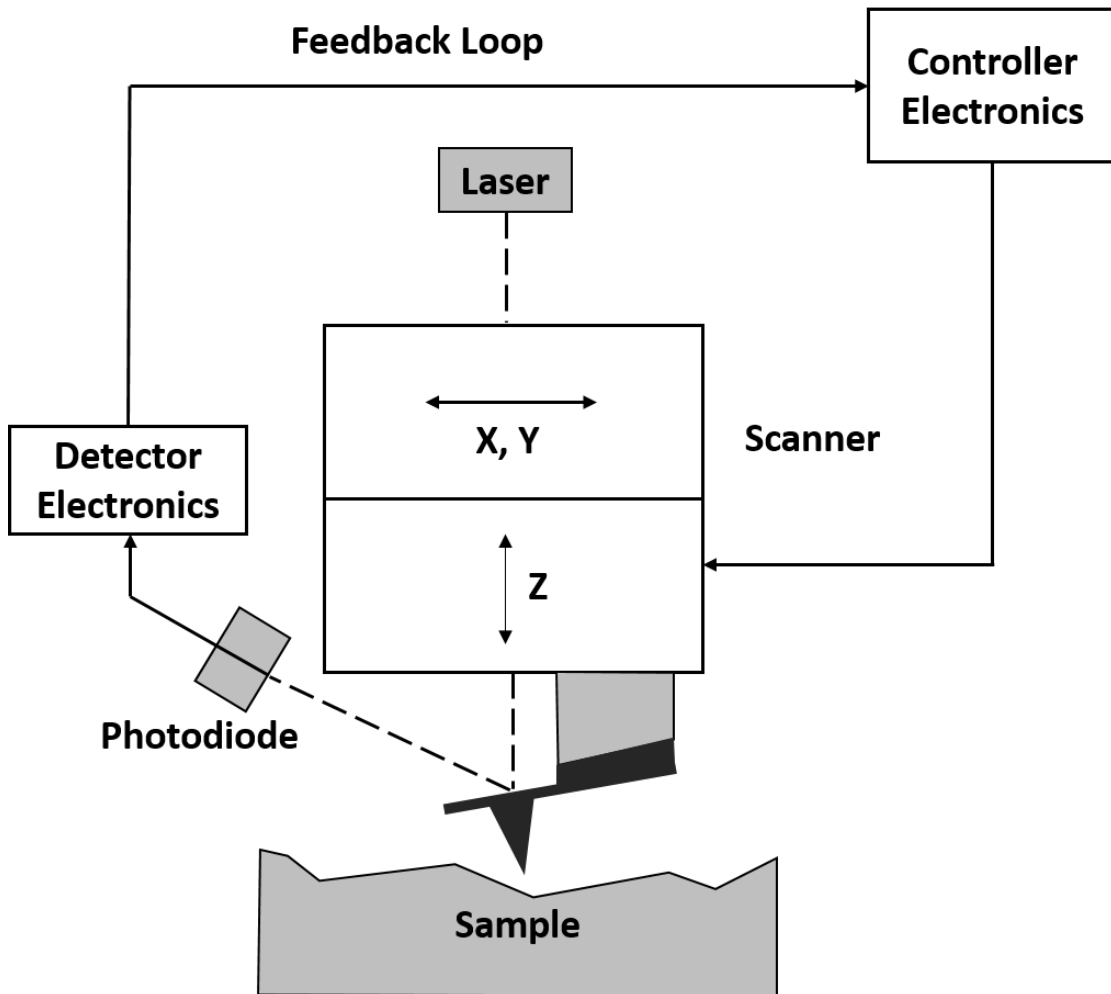


FIGURE 2.6: Basic working principle of an contact mode AFM. By scanning a tip across the sample surface, changes of the cantilever deflection is monitored with photodiode detector.

Having the height data, we can easily generate images with analysis software. The feedback loop is shown in Fig. 2.6.

In addition to AFM, x-ray technique is another powerful tool to probe the crystal structure as well as the thickness of the Bi_2Te_3 thin films. X-ray diffraction (XRD) is based on the elastic scattering of x-ray photons by the crystal lattice of the probed sample. The monochromatic x-rays scattered at specific angles give constructive interference, from which the diffraction peaks are produced. Fig. 2.7

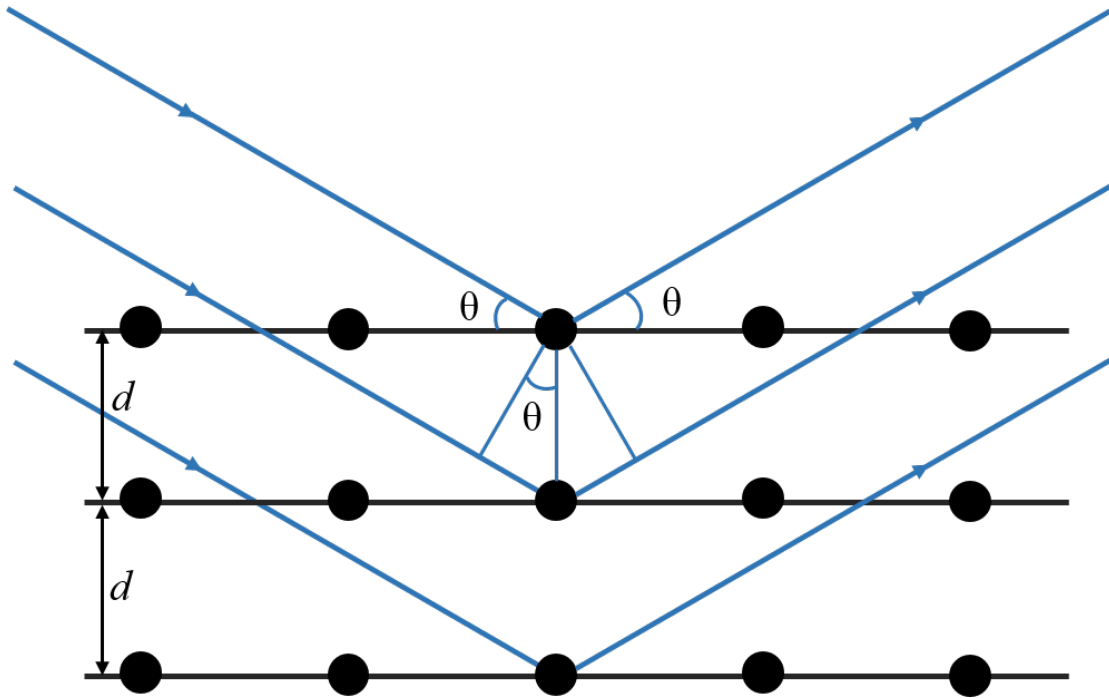


FIGURE 2.7: Schematic diagram of diffraction of x-rays by a crystal (Bragg condition).

illustrates the diffraction of x-rays by crystal planes and how one can derive lattice spacing with Bragg's law (Eq. 2.1).

$$2d \sin \theta = n\lambda (n \in \mathbb{N}) \quad (2.1)$$

Where d is interplanar spacing, θ is the angle between the incident beam and the crystal planes that diffract, n is the order of reflection, and λ is the wavelength of x-rays (we use $\lambda = 1.54056 \text{ \AA}$, the wavelength of the $K\alpha_1$ emission line for Cu). By varying the incident angle θ , the detector at the diffraction angle 2θ can collect the diffraction spectra, from which one can calculate d by using Bragg's law, furthermore, crystal structure of the material can be determined by analyzing the main peakwidth and the satellite diffraction spectra (Kiessig fringes). This is achieved via a θ - 2θ scan, which is frequently used in crystalline structure determination.

On the other hand, the x-ray reflectivity (XRR) measurement can be used to determine the thickness of thin films. The x-rays undergo total reflection for the incident angle smaller than the critical angle (θ_c) and penetrate inside the film for the incident angle greater than θ_c . The interference between the x-rays reflected from different interfaces result in interference fringes (Kiessig fringes). By using Eq. 2.2 and 2.3, we can easily estimate the thickness of thin films.

$$2t\sqrt{\sin^2 \theta_m - \sin^2 \theta_c} = m\lambda \quad (2.2)$$

$$\theta_m^2 - \theta_c^2 = m^2 \left(\frac{\lambda}{2t}\right)^2 \quad (2.3)$$

Where t is the layer thickness, θ_m is the angle position of the m -th maximum in Kiessig fringes, θ_c is the critical angle for the total external reflection, λ is the x-ray wavelength [106].

Chapter 3

Epitaxial Growth and Characterization of Bi_2Te_3 Thin Films

3.1 General considerations

As mentioned in the previous section, we employ the MBE technique to grow high-quality single crystalline Bi_2Te_3 thin films [107, 108]. As shown in the Bi-Te phase diagram (Fig. 3.1(a)), bismuth and tellurium can only form stoichiometric Bi_2Te_3 compound and excess Te, without any secondary phase, when the atomic percentage of tellurium is more than 0.6. This gives us the idea that we do not have to keep Te/Bi (θ) flux ratio strictly at 3:2, but under highly Te-rich condition ($\theta = 8-20$) with the substrate temperature satisfying $T_{\text{sub}} \geq T_{\text{Te}}$. At fixed temperature, the saturated vapor pressure of Te is much larger than that of Bi, therefore we can set $T_{\text{Bi}} > T_{\text{sub}} \geq T_{\text{Te}}$, then the extra Te molecules cannot be

incorporated into the film and will desorb. Thus, we can guarantee the growth of Bi₂Te₃ thin films under such conditions. Here, T_{Te} and T_{Bi} are the temperatures of Te and Bi Knudsen cells, which were used to precisely control the deposition flux. The crystal structure of Bi₂Te₃ is schematically shown in Fig. 3.1(b). It has a rhombohedral structure and belongs to space group R3m. The a-b (111) plane has hexagonal structure with the lattice constant 4.38 Å. Along the [111] crystallographic direction, the unit cell contains five atomic layers with a stacking sequence of Te(1)-Bi-Te(2)-Bi-Te(1), in which the middle Te layer is coordinated differently than the side Te layers. The unit cell is called a quintuple layer (QL) and is ~ 1 nm in height. The lattice constant along this direction is 10.17 Å. The interaction between two adjacent QLs is of van der Waals type, while the interaction between two atomic layers within a QL relies on covalent bonding. As a result, a bulk Bi₂Te₃ crystal always gives a Te-terminated cleaved surface due to its low surface energy. Our experiments were conducted in a home-made MBE growth chamber (details in chapter 2) with the base pressure better than 1×10^{-10} mbar. High purity Bi (99.9999%) and Te (99.9999%) were evaporated from individual standard Knudsen cells. The substrate was heated by radiant heating and the temperature was controlled by a proportional–integral–derivative (PID) controller.

3.2 Epitaxial growth of Bi₂Te₃ thin films

Bi₂Te₃, Bi₂Se₃ and Sb₂Te₃ all belong to the same TI family and share the same crystal structure as shown in Fig. 3.1(b) for Bi₂Te₃. The growth mechanism of these materials is similar. As the study of TIs has become a hot topic, plenty of successful growth experiments of epitaxial Bi₂Se₃ and Bi₂Te₃ thin films on variety of substrates have been reported. For example, Bi₂Te₃ and Bi₂Se₃ have been grown

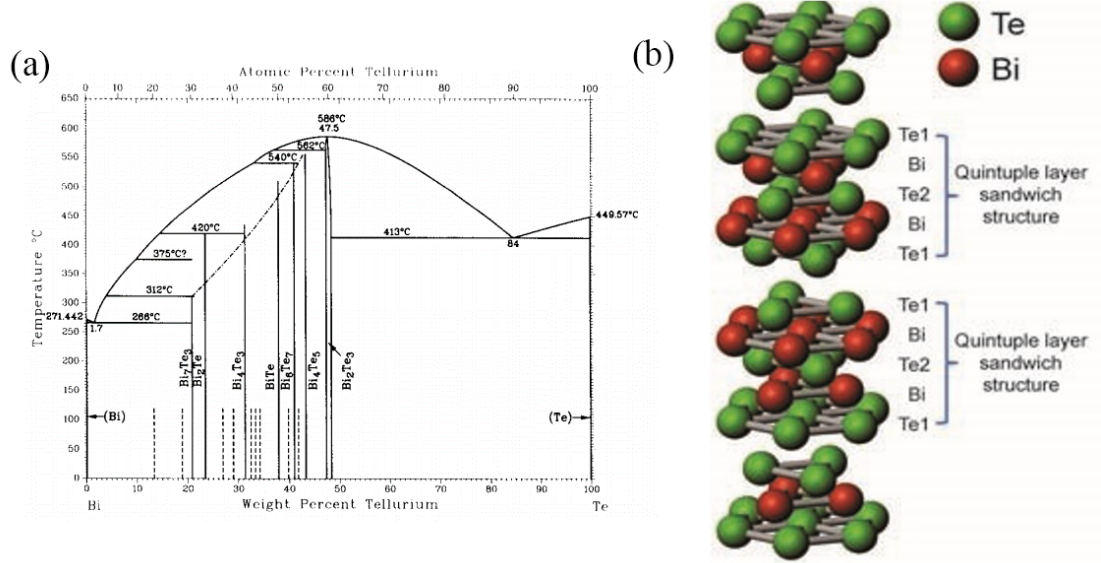


FIGURE 3.1: (a) Binary alloy phase diagram of Bi-Te and (b) Tetradymitetype crystal structure of Bi_2Te_3 . Figures are adapted from Ref. [8, 9]

on Si(111) [107], and $\text{Cr}_{0.15}(\text{Bi}_{0.1}\text{Sb}_{0.9})_{1.85}\text{Te}_3$ has been grown on STO(111)[109], and Bi_2Se_3 has been grown on $\text{Al}_2\text{O}_3(0001)$ [110]. In our work, Bi_2Te_3 thin film is grown on $\text{SrTiO}_3(111)$ and $\text{Al}_2\text{O}_3(0001)$ substrates, respectively.

3.2.1 Growth of STO(111)/ Bi_2Te_3

Polished single crystal STO(111) substrates were purchased from commercial vendors (CrysTec GmbH). The miscut of such substrates is less than 0.1° . The substrate was cleaned with acetone and ethanol ultrasonically and soaked in DI water at 140°C for 90 minutes, which was followed by annealing the substrate in the furnace at 880°C with flowing oxygen for 3 hours. Then an atomically flat surface with average surface roughness less than 4 \AA is obtained, which is crucial for epitaxial growth of thin films. After the cleaning and annealing procedure, the substrate was loaded into the growth chamber. Inside the growth chamber,

the substrate was heated to ~ 350 °C. This helps to remove the adsorbates and contaminants which can be pumped away. After 1 hour at 350 °C, the substrate was brought to growth temperature. Meanwhile, Bi and Te sources were heated to evaporation temperature. We let the substrate and sources stabilize thermally for at least 30 minutes before starting the deposition.

The critical growth parameters are the Te₂/Bi flux ratios (θ) and STO substrate temperatures (T_{sub}). The fluxes of Bi and Te were tested separately before co-deposition of Bi₂Te₃. In our case, we set evaporation temperature of Bi at ~ 515 °C and substrate temperature at ~ 160 °C, while the evaporation temperature of Te is fixed at ~ 210 °C. At these temperatures, the Te/Bi flux ratio is ~ 15 -20 which satisfies the condition of forming Bi₂Te₃. After the Te/Bi flux ratio is set, the growth of Bi₂Te₃ is mainly controlled by the temperature of the substrate. From the initial temperature that Te will not stick on the STO surface, we increase T_{sub} step by step to monitor the real time growth with help of RHEED. By a systematic study of the growth conditions and parameters, we established the optimal conditions for layer-by-layer growth of Bi₂Te₃ and the temperature of substrate was set to 160 °C. Under such growth condition, the growth rate of Bi₂Te₃ thin film was ~ 0.1 QL per minute. It should be noted that all the temperatures of sources and substrate can only be a reference. It might be different from another MBE system.

We investigate the RHEED patterns of cleaned STO (111) surface and the Bi₂Te₃ film which were captured during the deposition of Bi₂Te₃ thin film. The electron beam incidence is along the Γ - K direction. Fig. 3.2(a) shows the RHEED pattern of the cleaned substrate. The RHEED pattern after 3 QL growth is shown in Fig. 3.2(b). Fig. 3.2(c) shows RHEED pattern of a 10 QL film at the end of growth with substrate temperature at 160 °C. The clear and sharp streaky pattern shown in Fig. 3.2(c) indicates that the film has an atomically flat surface morphology.

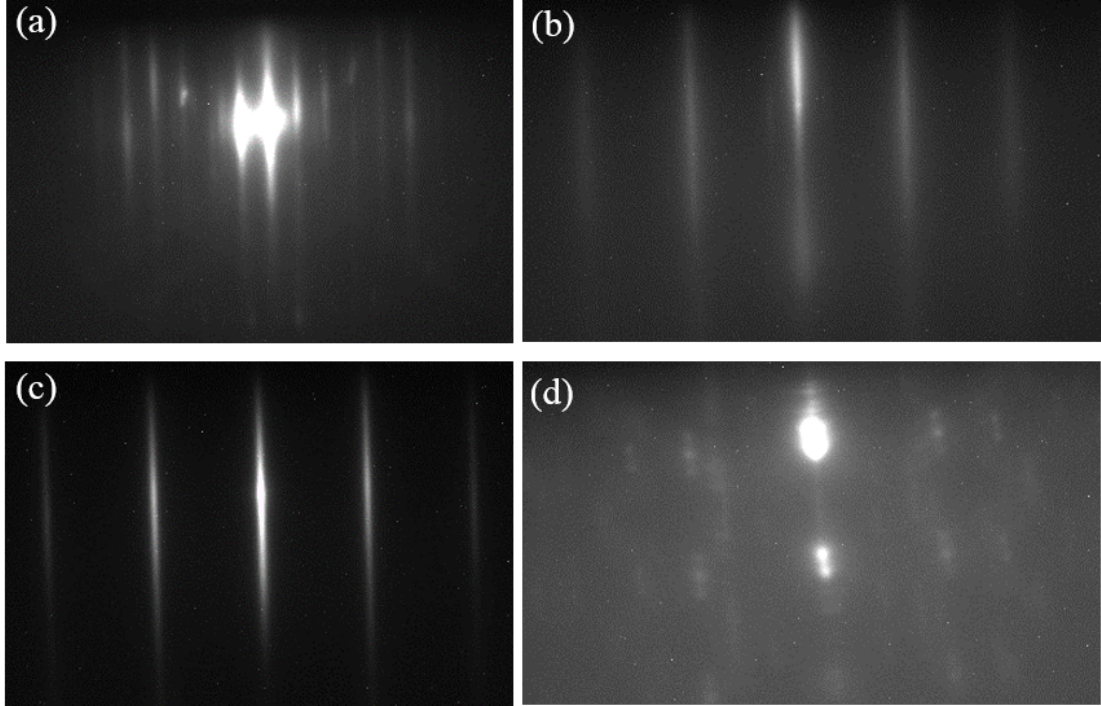


FIGURE 3.2: RHEED patterns of (a) STO (111) substrate, (b) Bi₂Te₃ film of 3 QL on STO(111) with T_{sub}=160 °C, (c) Bi₂Te₃ film of 10 QL on STO(111) with T_{sub}=160 °C and (d) Bi₂Te₃ film on STO(111) with T_{sub}=140 °C.

As comparison, Fig. 3.2(d) is the RHEED pattern for a sample growing with a substrate temperature of 140 °C displaying a spotty pattern characteristic of 3D growth. These last patterns indicate that the growth condition is not optimized and that the crystallinity of Bi₂Te₃ is very sensitive to the substrate temperature.

After the film is taken out from the chamber, it is investigated by AFM and x-ray technique. Fig. 3.3(a) and (b) display the surface topography of a 10 QL Bi₂Te₃ film deposited by MBE on a STO (111) substrate with substrate temperature at 140 °C and 160 °C, respectively. In Fig. 3.3(a), the film topography is not characteristic of layer by layer growth which agree with the RHEED pattern shown in Fig. 3.2(d). Fig. 3.3(b), in contrast, shows a film surface with flat terrace, except for a tiny amount of nanoscale islands and voids. Fig. 3.3 (c) shows the line profile

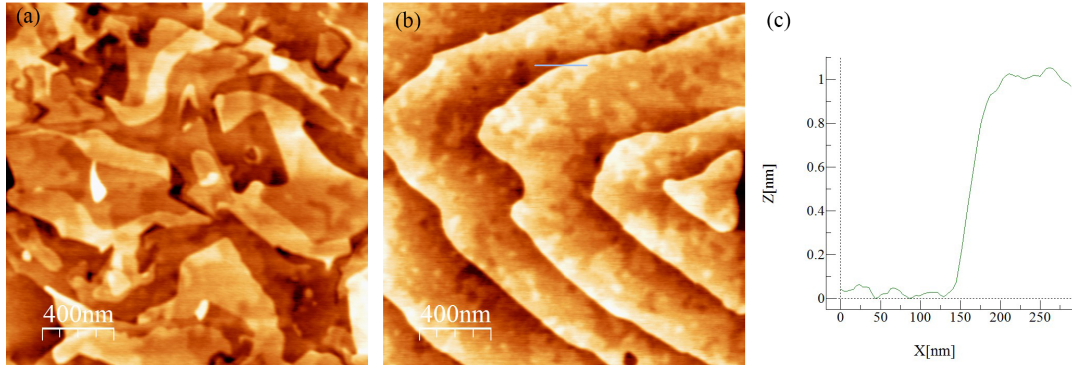


FIGURE 3.3: AFM images showing the surface morphology of the Bi₂Te₃ films growing with substrate temperature at 140 °C (a) and 160 °C (b), respectively, (c) The line profile taken across the area shown in (b).

taken across the area in (b). The height of the islands is 1 QL (~ 1 nm).

Fig. 3.4(a) shows θ - 2θ XRD patterns of Bi₂Te₃ thin films grown on STO (111) substrate. The (006), (0015), (0018) and (0021) XRD peaks are very clear, which are all collinear with the (001) direction, indicating single-crystal epitaxial growth with the c-axis in growth direction. The thickness of Bi₂Te₃ film is 5 QL (~ 5 nm). The insert panel in Fig. 3.4(a) is the XRR pattern which can be used to determine the thickness of the layers, fitted by an analysis software (Leptos). The in-plane phi scan of the film by XRD is shown in Fig. 3.4(b). It shows the peaks from the (015) plane of Bi₂Te₃ (0001). The film show six-fold symmetry, as expected from the in-plane crystalline structure of Bi₂Te₃.

3.2.2 Growth of Al₂O₃(0001)/Bi₂Te₃

The growth mechanism of Bi₂Te₃ film on Al₂O₃(0001) substrate is similar with that on STO(111). Polished single crystal Al₂O₃(0001) substrates were purchased from commercial vendors (CrysTec GmbH). The miscut of such substrates is less than 0.1 °. The pre-treatment of Al₂O₃(0001) substrate can be found in Appendix which

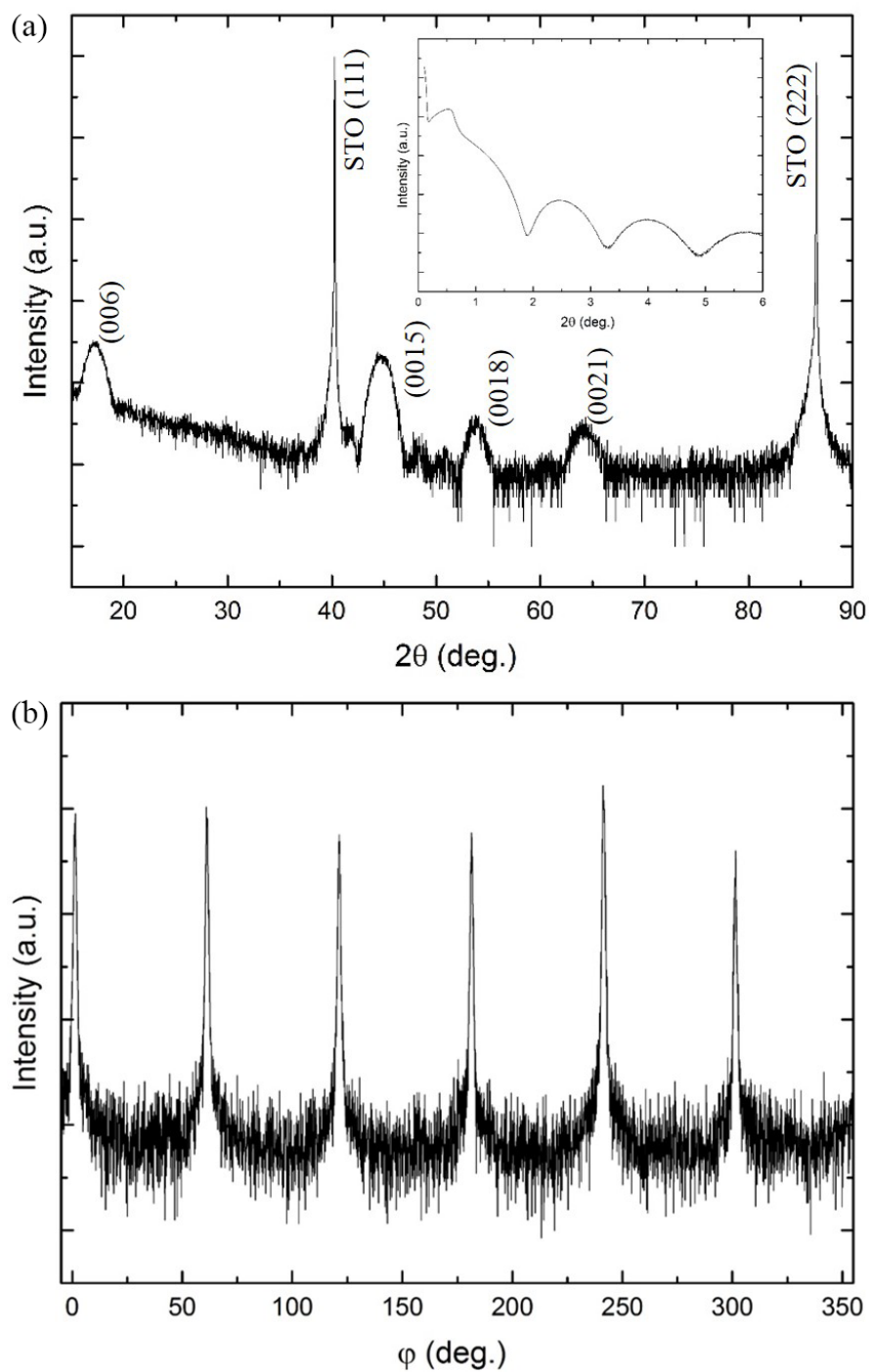


FIGURE 3.4: The XRD curves for 5 QL Bi_2Te_3 thin film. (a) θ - 2θ scan shows the peaks. The XRR scan is performed between 0 - 6° (2θ) as shown in the insert panel. (b) ϕ scan profile using the (015) planes for the Bi_2Te_3 layer.

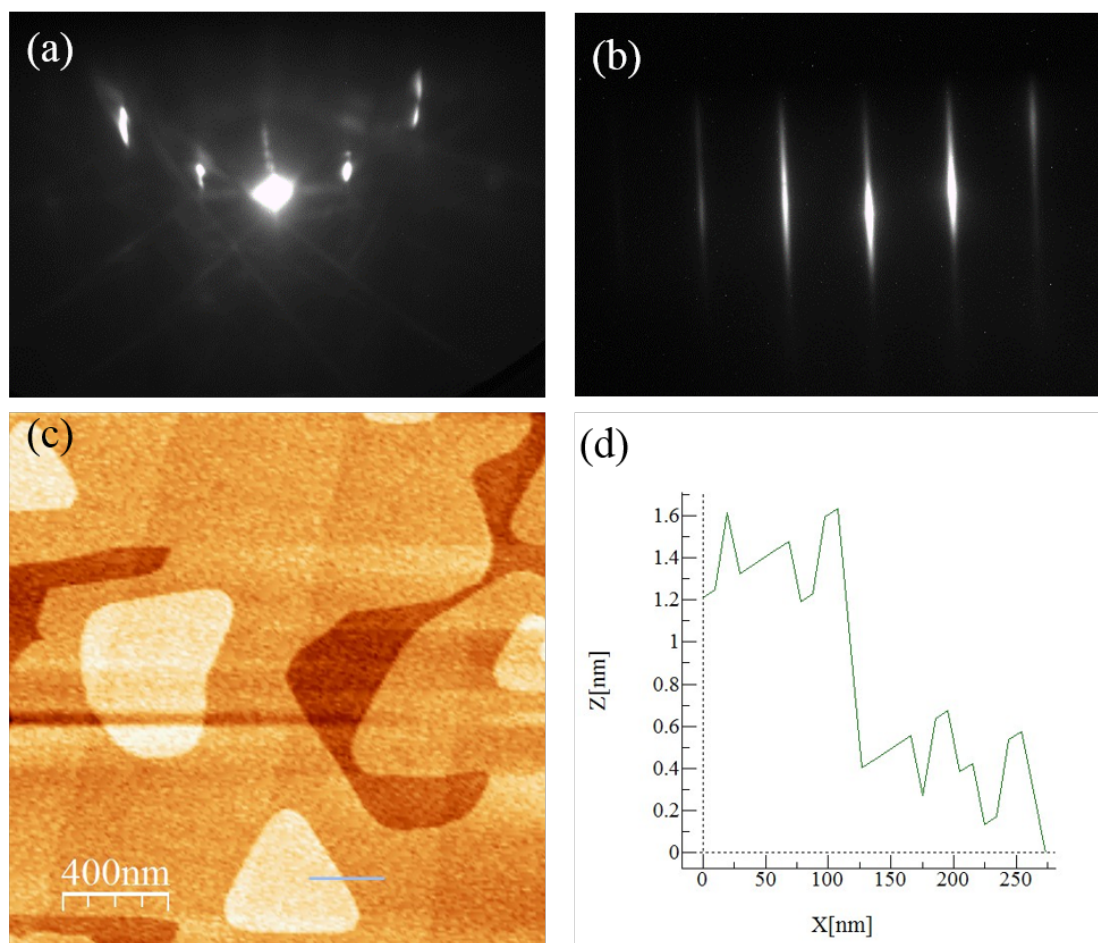


FIGURE 3.5: Characterization of Bi_2Te_3 film grown on $\text{Al}_2\text{O}_3(0001)$. (a) and (b) are RHEED patterns of $\text{Al}_2\text{O}_3(0001)$ and 7 QL Bi_2Te_3 film on $\text{Al}_2\text{O}_3(0001)$, respectively; (c) is an AFM image of Bi_2Te_3 film and (d) is the profile taken across the blue area in (c).

is different from $\text{STO}(111)$ and involves more steps. The evaporation temperature of Bi and Te was set $545\text{ }^\circ\text{C}$ and $240\text{ }^\circ\text{C}$, respectively, while the temperature of substrate was at $230\text{ }^\circ\text{C}$. Both the clear and sharp streaky RHEED pattern (Fig. 3.5(b)) and the AFM image (Fig. 3.5(c)) indicate the high quality of the thin film.

In summary, taking advantage of *in-situ* and *ex-situ* characterizations, the growth procedure of Bi_2Te_3 thin films by MBE has been optimized on both $\text{STO}(111)$

and Al₂O₃(0001) substrates. Therefore we start with high-quality samples for the measurements in next chapters.

Chapter 4

Electronic Transport Measurements

In Chapter 2 and 3 we discussed the growth and structural characterization of Bi_2Te_3 thin films. In order to understand the charge-to-spin phenomena associated with those films, we first investigate the charge transport, by performing electrical and magneto transport characterizations of our samples.

4.1 Measurement geometry

For the measurement of electrical properties of thin films, either the Hall bar geometry or the Van der Pauw (VdP) geometry is mostly used, both of which are schematically shown in Fig. 4.1. Both measurements employ a four-point contact scheme, which can avoid the measurement of contact resistances and lead resistances. For two-point measurements, these issues are unavoidable. In our electrical measurements, Hall bar geometry is employed. We aim to measure the

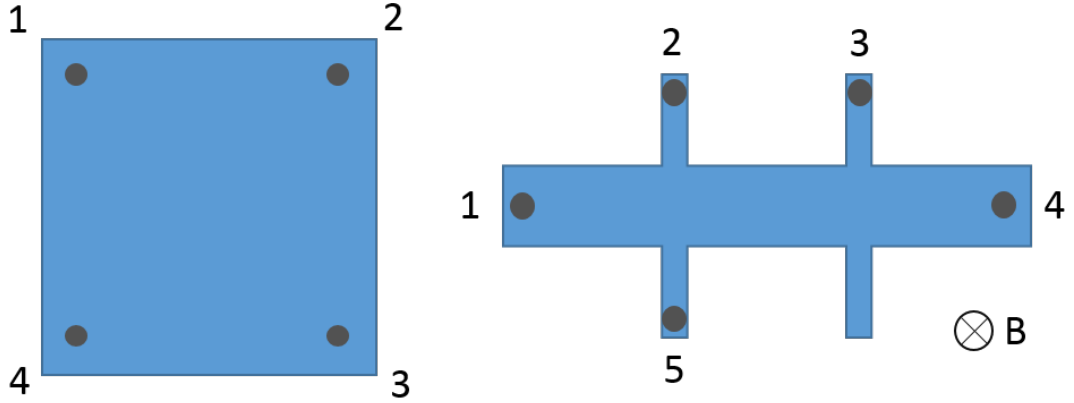


FIGURE 4.1: Electrical measurement geometries: Van der Pauw geometry (left panel) and Hall bar geometry (right panel). The black circles represent measurement leads and the magnetic field is applied perpendicular to the plane.

longitudinal resistance (R_{xx}) and Hall resistance (R_{xy}) of the given samples. From these measured data, we can extract carrier density and mobility of the film, which are the most relevant parameters related to the electrical properties of the thin films.

In the Hall bar geometry, the resistivity $\rho_{xx} = V_{23}/I_{14} \times (w \times t/l)$ and Hall resistivity $\rho_{xy} = V_{25}/I_{14} \times (w \times t/l)$, where w , l and t are the width, length and thickness of the sample, respectively.

In practice, the measurement leads are never perfectly aligned. Such misalignment brings mixing of longitudinal and Hall voltages. In other words, experimentally measured longitudinal resistance R_{xx} picks up a small portion of the Hall resistance R_{xy} and vice versa. This problem can be solved by the properties of longitudinal and Hall resistance with post data analysis. As we know, R_{xx} is an even function of magnetic field, while R_{xy} is an odd function of magnetic field. The raw data can be processed with respect of magnetic field to get unmixed values of R_{xx} and R_{xy} using following equations:

$$\begin{aligned}
R_{xx}(B) &= \frac{R_{xx,exp}(B) + R_{xx,exp}(-B)}{2} \\
R_{xy}(B) &= \frac{R_{xy,exp}(B) - R_{xy,exp}(-B)}{2}
\end{aligned} \tag{4.1}$$

4.2 Hall effect

In a semi-classical model, charged particles (electrons or holes) experience Lorentz force in the presence of electric field and magnetic field given by $\mathbf{F} = q(\mathbf{E} + \mathbf{v} \times \mathbf{B})$. \mathbf{v} and $q = \pm e$ are the velocity and the charge of the carriers, \mathbf{E} is the electric field. As shown in Fig.4.2, by applying a current along x direction and an out-of-plane magnetic field along z direction, a voltage develops along y direction (E_y). At steady state $qE_y = qvB$. This is the Hall effect which was first demonstrated by Edwin Hall. The Hall resistance is given as $R_{xy} = V_H/I$. Furthermore, I can be written in terms of current density as $I = jwt = nqvt$, where n is the areal carrier density and t is the thickness of the sample. As a result, we can get the expression $R_{xy} = B/nq$. The 2D carrier density can be determined by $n = 1/(qR_H)$, where the Hall constant R_H is defined as $R_H = R_{xy}/B$. In practice, for a single type of carrier, R_H can be determined from a linear fit to the transverse magnetoresistance trace $R_{xy}(B)$. Making use of the Drude formula for the electrical conductivity $\sigma_{xx} = nq\mu$, the carrier mobility μ is determined.

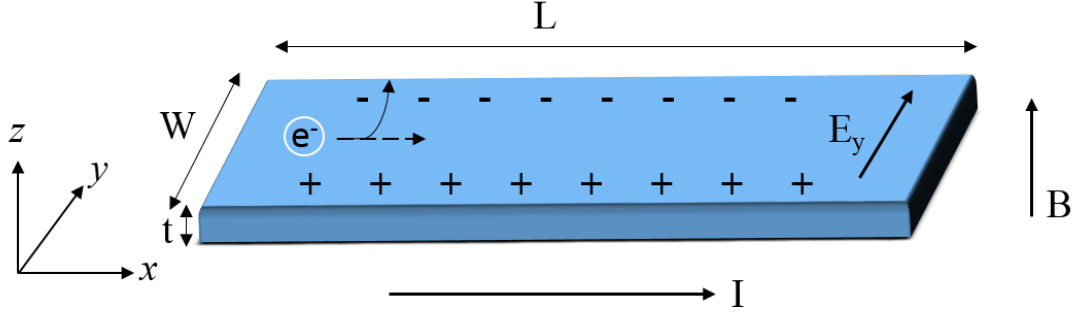


FIGURE 4.2: Hall effect measurement setup for electrons. By applying a current along x direction and an out-of-plane magnetic field along z direction, a voltage develops along y direction (E_y).

4.3 Temperature dependence of resistivity, carrier density and mobility

The magneto-transport studies are done on the samples using the Hall bar geometry and standard DC measurement in a physical property measurement system (PPMS), with magnetic fields up to 14 T and temperature down to 2 K.

The longitudinal resistivity is plotted versus temperature from 2 K to 300 K for Bi_2Te_3 samples with thickness of 5 QL, 10 QL and 20 QL, which is shown in Fig. 4.3. The R_{xx} vs T curves show metallic behavior at high temperatures with positive slope for all three samples. Below ~ 20 K, the resistivity remains almost constant and is quite thickness independent, except for thickness 5 QL, which shows slight increase in resistivity with decreasing temperature, indicating static disorder and scattering at grain boundaries [111, 112], more likely to happen at low film thicknesses. An upturn due to Kondo effect is unlikely as there are no magnetic impurities in the Bi_2Te_3 layers. Also, the resistivity of the film with thickness of 5 QL is much higher than the other two films, which suggest the suppression of bulk conductivity.

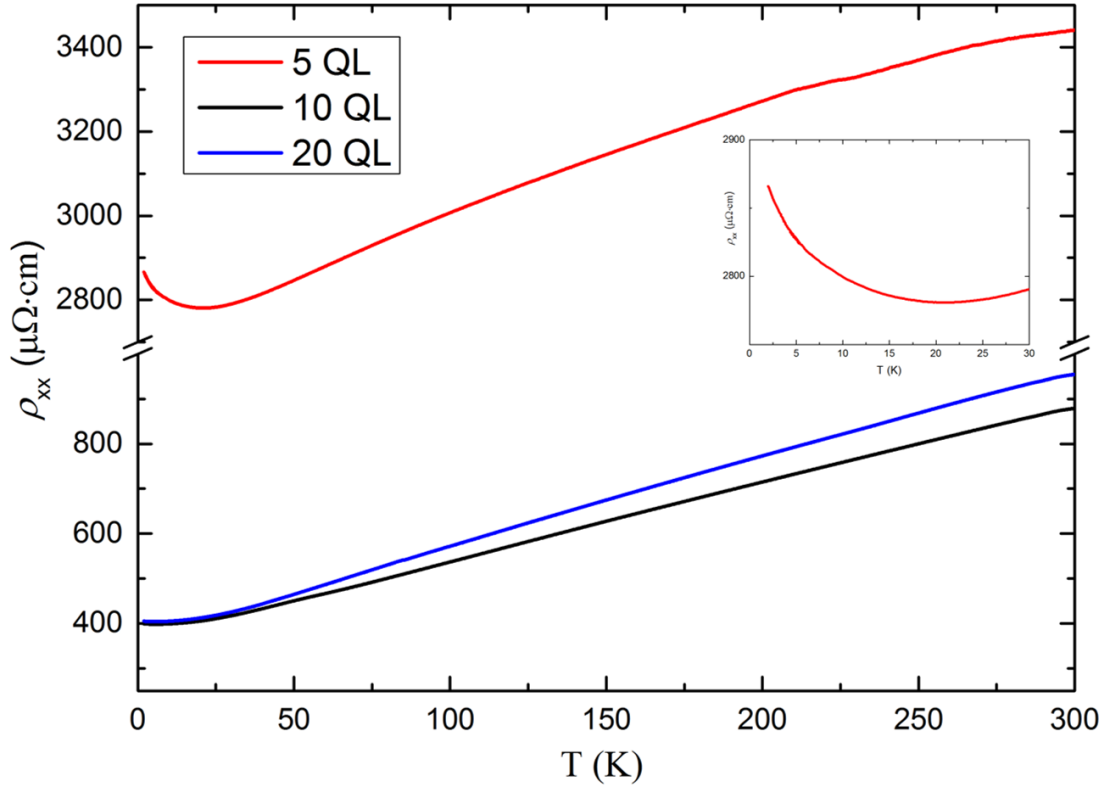


FIGURE 4.3: Temperature dependence of longitudinal resistivity for temperature varying from 2 K to 300 K with film thickness $d=5$ QL, 10 QL and 20 QL. The inset shows the resistivity for 5 QL Bi_2Te_3 ranging from 2 K to 30 K.

Fig. 4.4 shows the normalized MR of the film with $d=5$ QL measured at different temperatures in a perpendicular magnetic field. At $T=2$ K, the MR shows a sharp cusp in the weak field regime. As T increases, the MR dip decreases until $T=20$ K and diminishes at $T=50$ K. Also, we can notice that the MR displays more linear dependence rather than a parabolic dependence in the high field regime. This is consistent with the reports on Bi_2Se_3 thin film grown on sapphire [113] and Bi_2Te_3 thin film grown on Si (111)-(7 \times 7) [114]. The linear MR can be understood by the linear quantum MR model [115], as the topological states are zero-gap with linear E-K dispersion [116]. It is an evidence that the surface state dominates the electronic transport.

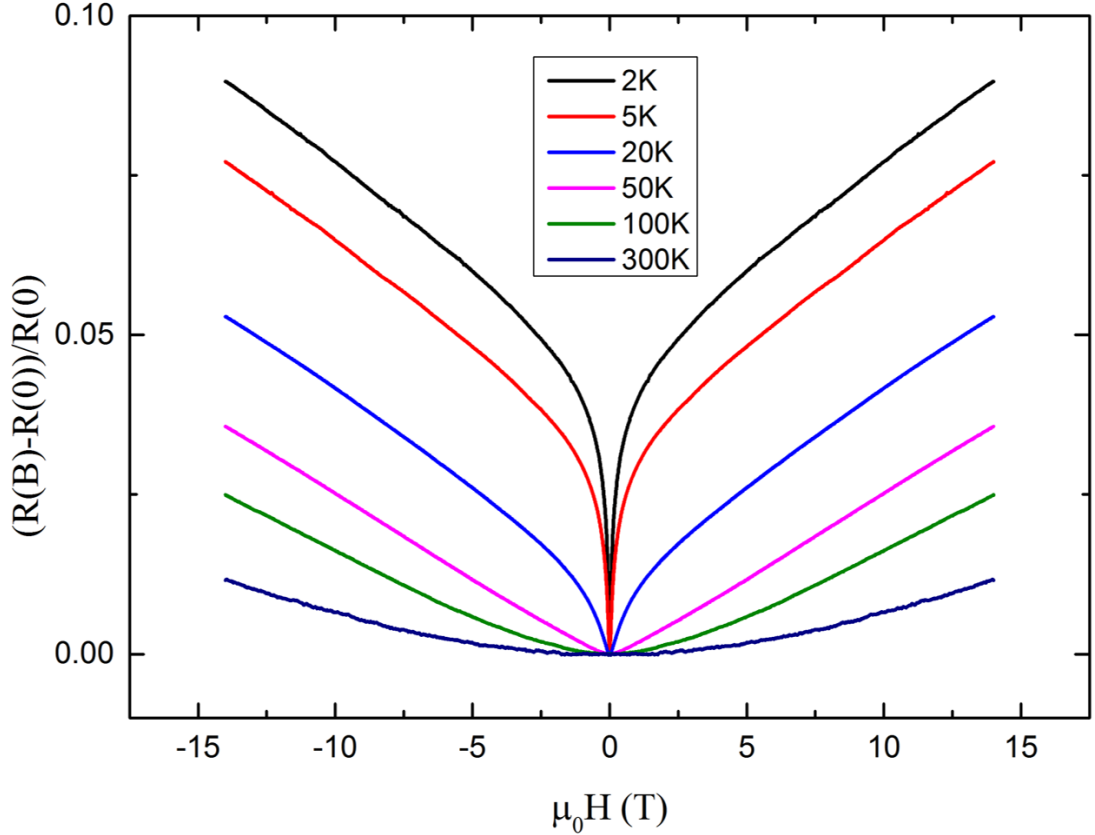


FIGURE 4.4: The normalized magnetoresistance of the film with $d=5$ QL measured at various temperatures. In the weak H regime, the MR shows a steep increase characteristic of WAL with temperature below 20 K.

As shown in Fig. 4.5(a), the 2D carrier density of electrons changes with different thickness of Bi_2Te_3 films. The total 2D carrier density estimated from the Hall coefficient is around $2.8 \times 10^{13}/\text{cm}^2$ at 2 K for the 5 QL film, and reaches to around $10 \times 10^{13}/\text{cm}^2$ for the 20 QL film. From 2 K to 300 K, the carrier density and mobility remain almost constant for 5 QL, and do not change so much for 10 QL and 20 QL, which suggests the contribution of the bulk states is still weak. As reported in [110, 117], the selection of substrates presumably plays a role in the values of 2D carrier density. Bansal et al. [110] and Kim et al. [117] grow Bi_2Se_3 films on $\text{Al}_2\text{O}_3(0001)$ and $\text{Si}(111)$ respectively. In their results, for films grown on Si, it also shows a thickness dependence, while for films grown on Al_2O_3 , nearly

thickness independent values of 2D carrier density are observed. The films grown on STO (111) in this dissertation have similar properties like the former.

For the thickness-related transport in TIs, Bansal et al. [110] reported the evidence of two surface channels in Bi_2Se_3 films. They claim that the two surface channels are TI band and two-dimensional electron gas (2DEG) by measuring electrical properties on Bi_2Se_3 film with thickness ranging from 256 - 2 QL. We plot n_{2D} vs thickness as shown in Fig. 4.6 and find the carrier density changes less than an order of magnitude between 5 and 20 QL, a scenario compatible with the presence of topological surface states rather than 2DEG channels. For the 2DEG case, the carrier density is expected to decrease abruptly in the region of band bending ($t=8$ nm for Bi_2Se_3) [110]. For the case of the parent Bi_2Te_3 studied here, however, a thinner 2DEG formation ($t<5$ QL) cannot be ruled out from the present data. This observation suggests we likely have a TI channel but not a 2DEG one [111, 112].

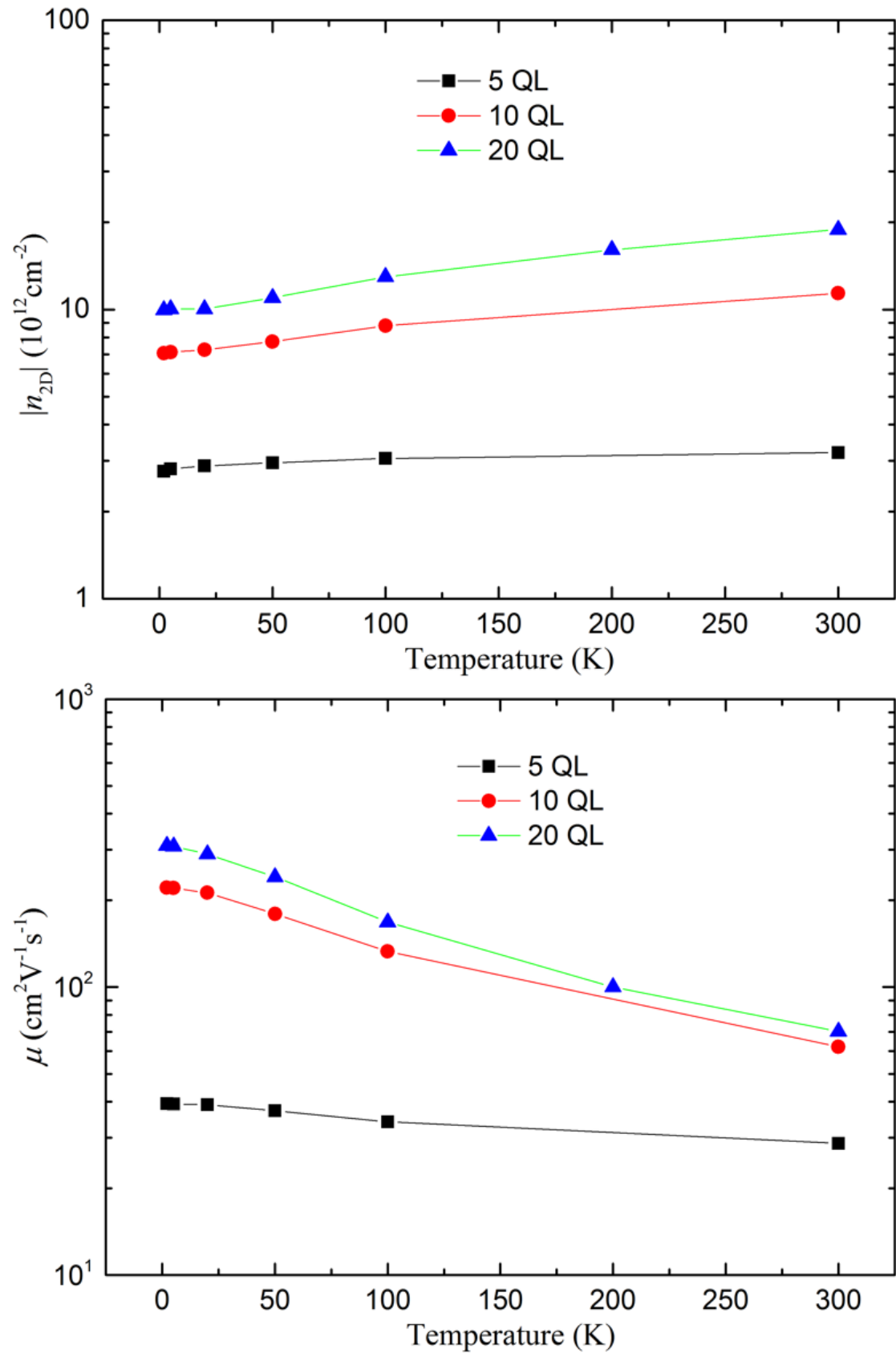


FIGURE 4.5: (a) 2D carrier density of electrons and (b) mobility of electrons in Bi₂Te₃ films grown on STO(111) obtained by Hall measurements at various temperatures with thickness $d=5$ QL, 10 QL and 20 QL.

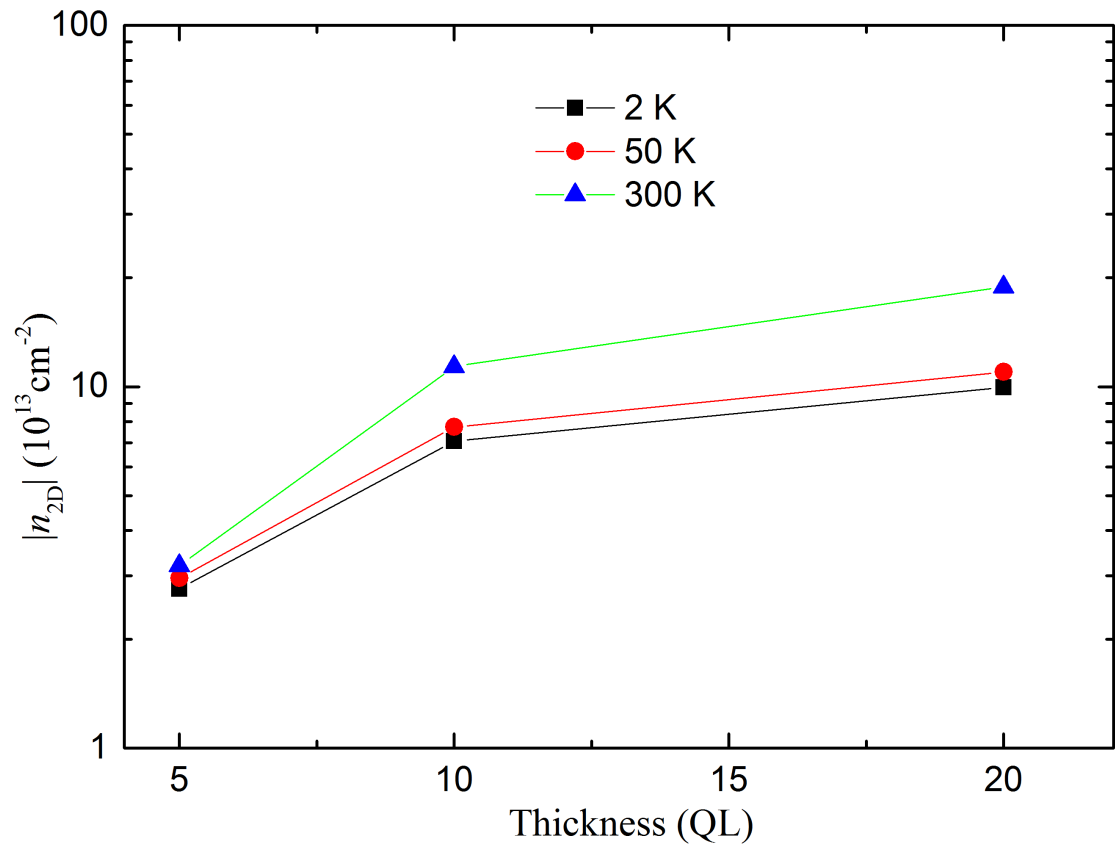


FIGURE 4.6: Dependence of 2D carrier density on film thickness for Bi₂Te₃ films grown on STO(111) at various temperatures .

Chapter 5

Spin Torque Ferromagnetic Resonance Experiments

5.1 Spin torque ferromagnetic resonance

To measure the spin transfer torque in TI/FM bilayers, the method of spin torque ferromagnetic resonance (ST-FMR) is employed, where the oscillation of a ferromagnetic layer is modified by the spin torque generated by a radio frequency (RF) current. By applying a RF current, the alternating Oested field can drive the ferromagnet into resonant precession when the frequency of the current matches the intrinsic precession frequency of the magnetic layer. Similar to the well-known ferromagnetic resonance technique where a RF magnetic field is applied to drive precession of a ferromagnet thin film, this is on an individual micrometer-sized device where the resonance condition is modified by any spin torque at RF frequency. The precession of the magnetic moment leads to the oscillation of the resistance,

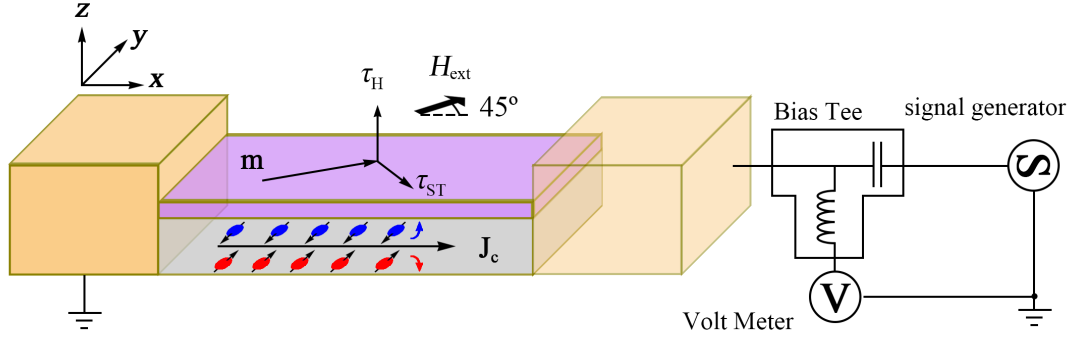


FIGURE 5.1: The wiring of the circuit to the device. RF generator is attached on high frequency port of the bias tee. Voltage meter is on the DC port.

because of the anisotropic magnetoresistance of the ferromagnetic layer, so the dynamics of the moment can be detected by measuring the voltage across the device. The illustration of the circuit is shown in Fig. 5.1.

In a typical ST-FMR measurement, the device is placed 45° to the magnetic field, where anisotropic magnetoresistance, and hence the change in device resistance as magnetization direction precesses, is largest, giving better resonance signal. A Keysight N5183B is used as RF current generator and attached on the RF port of the Bias Tee. A Keithley 2182A nanovoltmeter is connected on the DC port to detect the mixing voltage. With the RF current $I(t) = I_{rf}\cos(\omega t)$ (I_{rf}, ω are the amplitude and the frequency of RF current, respectively) passing through the device, the resistance of the device changes, since moment of the magnetic layer is oscillating due to both RF field and spin torque from SHE. The resistance is time dependent, $R(t) = R_0 + \delta R \cos(\omega t + \varphi)$. δR is the amplitude of the resistance oscillation and φ is caused by the phase difference which directly relates the shape of the resonance peaks in the DC mixing voltage spectrum to the direction of spin transfer torque as illustrated in Fig.5.2. The voltage arising from current-resistance mixing can be expressed as $\frac{1}{2}I_{rf}\delta R[\cos\varphi + \cos(2\omega t)]$. The first term is

independent of time, while the second term is the second harmonic term. So we can detect $V_{mix} \sim \frac{1}{2}I_{rf}\delta R\cos\varphi$ via the multimeter.

To study the signal of the mixing voltage, it is necessary to understand the dynamics of the magnetization precession. As shown in Fig. 5.1, an oscillating transverse spin current is generated in the NM layer by the SHE and injected into the adjacent FM layer, thereby exerting an oscillating spin torque on the FM layer. On the other hand, an out-of-plane torque is induced by the Oersted field. We model the motion of the FM layer magnetic moment m by the Landau-Lifshitz-Gilbert equation containing the spin torque term [118]:

$$\frac{d\hat{m}}{dt} = -\gamma\hat{m} \times \vec{H}_{eff} + \alpha\hat{m} \times \frac{d\hat{m}}{dt} + \gamma\frac{\hbar}{2e\mu_0M_s t} \times J_s(\hat{m} \times \hat{\sigma} \times \hat{m}) - \gamma\hat{m} \times \vec{H}_{rf} \quad (5.1)$$

Where γ is the gyromagnetic ratio, H_{eff} is the sum of H_{ext} and the demagnetization field $4\pi M_{eff}$, α is the Gilbert damping coefficient, μ_0 is the permeability in vacuum, e is the electron charge, \hbar is the reduced Planck's constant, M_s is the saturation magnetization of the FM layer, t is the thickness of the FM layer, $J_s\hbar/2e$ is the oscillating spin current density injected into FM layer, σ is the direction of the injected spin moment, H_{rf} is the Oersted field generated by the RF current in the NM layer. The third and fourth terms of equation 5.1 are the result of in-plane spin torque and the out-of-plane torque due to the Oersted field, respectively.

At the resonance point, the projection of the magnetization precession reaches maximum. If the torque is only within the plane, the in-plane projection is in-phase with the RF drive. Since AMR is only sensitive to the in-plane component, the resistance oscillation and torque are in-phase. This results in a symmetric Lorentzian line-shape for the ST-FMR spectrum as shown in Fig. 5.2(c). On

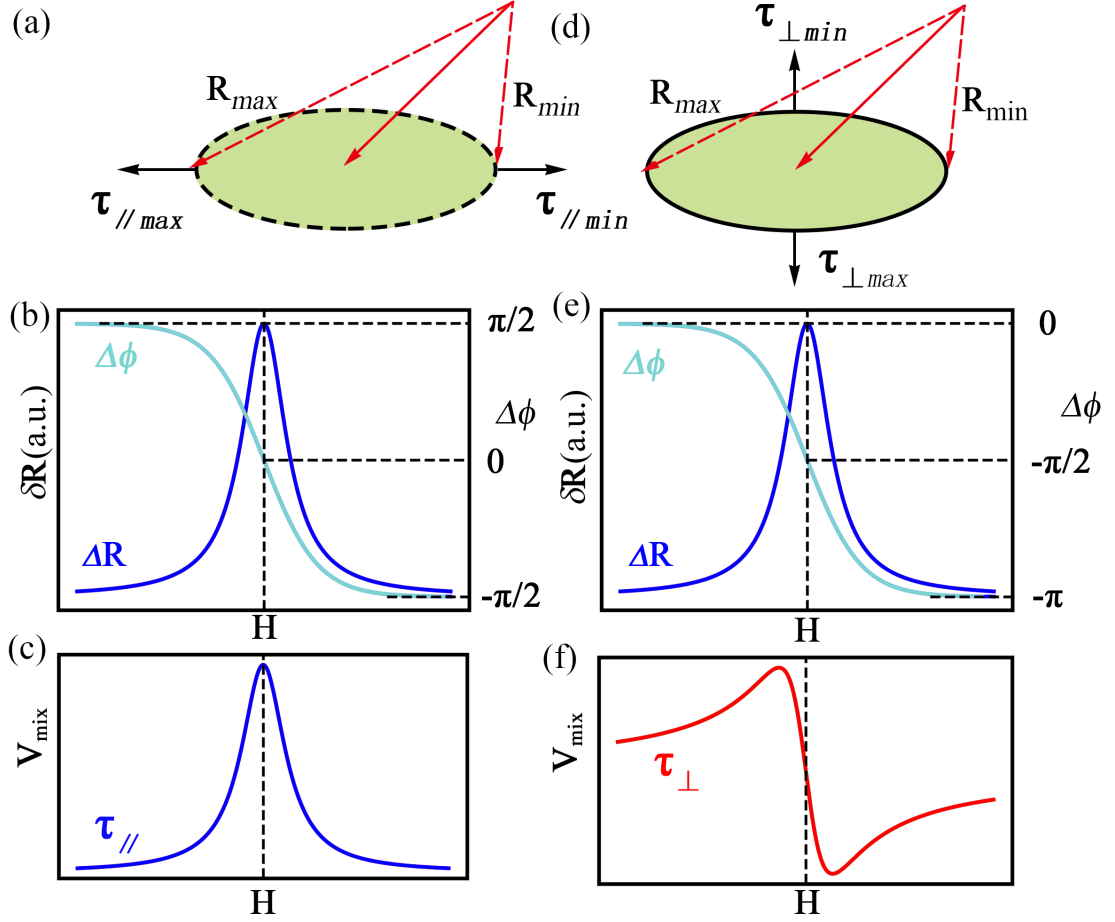


FIGURE 5.2: Illustration of the relation between the ST-FMR line-shape and the direction of the torque. (a)-(c) represent the in-plane torque at the resonance point. The resistance oscillation is in-phase with the driving current, leading to a symmetric line-shape. (d)-(f) describe the out-of-plane torque at the resonance point. The resistance oscillation is 90° out-of-phase with the driving current, leading to an anti-symmetric line-shape [10].

the other hand, if the torque is purely perpendicular, the out-of-plane projection becomes in-phase, so the resistance oscillation and torque are 90° out-of-phase. This leads to an anti-symmetric Lorentzian line-shape for the ST-FMR spectrum as shown in Fig. 5.2(f). With these analysis, one can determine the magnitude of both in-plane and out-of-plane torques by fitting experimental ST-FMR data to a sum of a symmetric Lorentzian and an anti-symmetric Lorentzian.

The mixing signal has been calculated in the context of ST-driven FMR[119, 120], which can be translated to the notation as following [121]:

$$V_{mix} = -\frac{1}{4} \frac{dR}{d\theta} \frac{\gamma I_{rf} \cos\theta}{H_{pp} 2\pi (df/dH)|_{H_{ext} = H_0}} \left[S \frac{H_{pp}^2}{H_{pp}^2 + (H_{ext} - H_{res})^2} + A \frac{H_{pp}(H_{ext} - H_{res})}{H_{pp}^2 + (H_{ext} - H_{res})^2} \right] \quad (5.2)$$

Where $S = \hbar J_s / (2e\mu_0 M_s t)$, $A = H_{rf} [1 + (4\pi M_{eff} / H_{ext})]^{\frac{1}{2}}$, H_{res} is the resonance field and H_{pp} is the linewidth. Equation 5.2 shows that the resonance signal consists of two components, a symmetric Lorentzian function proportional to J_s and an anti-symmetric Lorentzian function proportional to H_{rf} . The Oersted field H_{rf} can be approximately calculated by Ampere's law, $H_{rf} = J_{cd}/2$. The spin Hall angle (SHA, θ_{SH}) is the ratio of the spin current density entering the FM layer to the RF current density in the NM layer, which can be determined quantitatively.[121]

$$\theta_{SH} = \frac{J_s}{J_c} = \frac{S e \mu_0 M_s t d}{A \hbar} [1 + (4\pi M_{eff} / H_{res})]^{\frac{1}{2}} \quad (5.3)$$

5.2 Sample preparation and device fabrication

In the thesis, we use Bi₂Te₃/Py bilayers for the ST-FMR experiment. The details of film growth can be found in chapter 3. Here, we would like to briefly describe the procedure of device fabrication. The microstrip devices is fabricated using a standard photolithographic process. The maskless laser writer (MLA150, Heidelberg instruments) is used to write the patterns. Then we etch the microstrips using the ion milling, and deposit the contacts with 5 nm ruthenium / 50 nm gold



FIGURE 5.3: Microscope image of a typical microstrip device after fabrication used for ST-FMR measurements.

in a sputtering system (SCIA Coat 200). The active regions of our devices range from 10-75 μm long and 5-25 μm wide. A typical device is shown in Fig. 5.3.

5.3 Experiments and results

The system setup is shown in Fig. 5.4. It consists of an electromagnet to apply in-plane magnetic field and microscope to observe the device. The position of the RF probe is fixed in the center. By moving the sample stage in three directions, the device and the probe can be well contacted. The system is programmed with LabView to realize automated measurement.

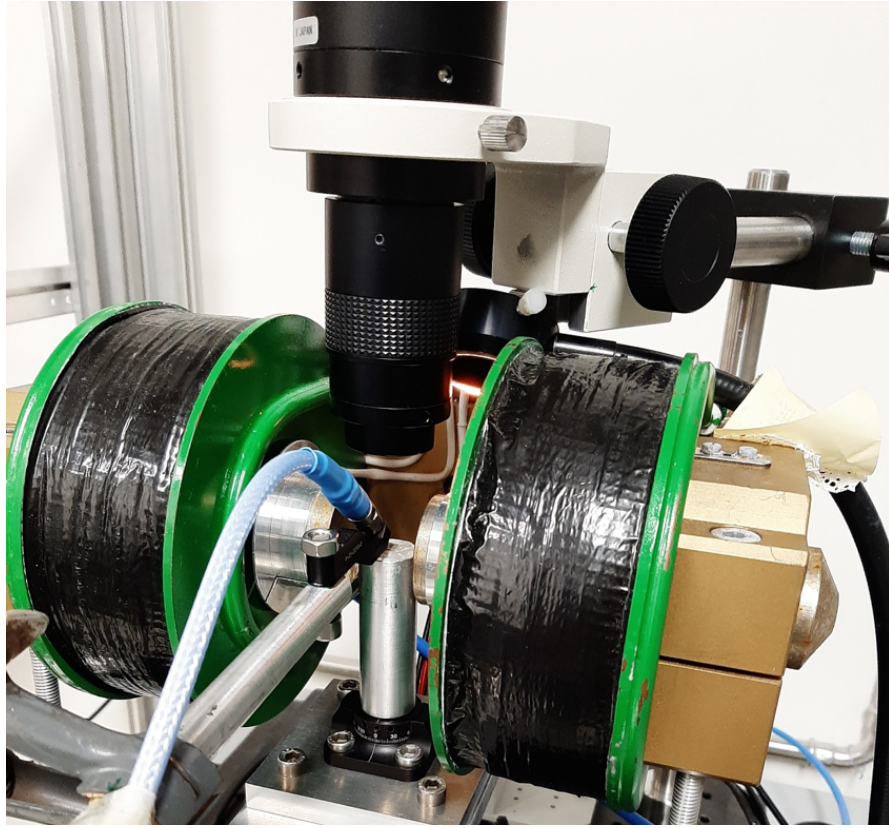


FIGURE 5.4: System setup of ST-FMR measurement. The RF probe is fixed in the center of the magnetic field and sample holder can be moved in three directions. On the top of the magnet, a microscope is used to observe the position of the device and the probe.

Fig. 5.5 shows ST-FMR spectra measured on 10 QL $\text{Bi}_2\text{Te}_3/5$ nm Py bilayers for RF frequencies varying between 4 and 14 GHz. V_{mix} is plotted versus H_{ext} for various RF frequencies f . As expected, the resonance peak shapes can be very well fit with equation 5.2 [fits are shown as lines in Fig. 5.5]. Fig. 5.6 (a) is a typical mixing voltage measured at $f=8$ GHz and fitted with a symmetric component and an antisymmetric component, from which the ratio of S/A in equation 5.3 can be extracted, as well as the resonant field and the line width. The resonant peak positions (H_{res}) are summarized in Fig. 5.6 (b). By fitting the frequency as a function of the resonant field using the Kittel formula [122] $f = \frac{\gamma}{2\pi} \sqrt{(H_{res} + 4\pi M_{eff})H_{res}}$,

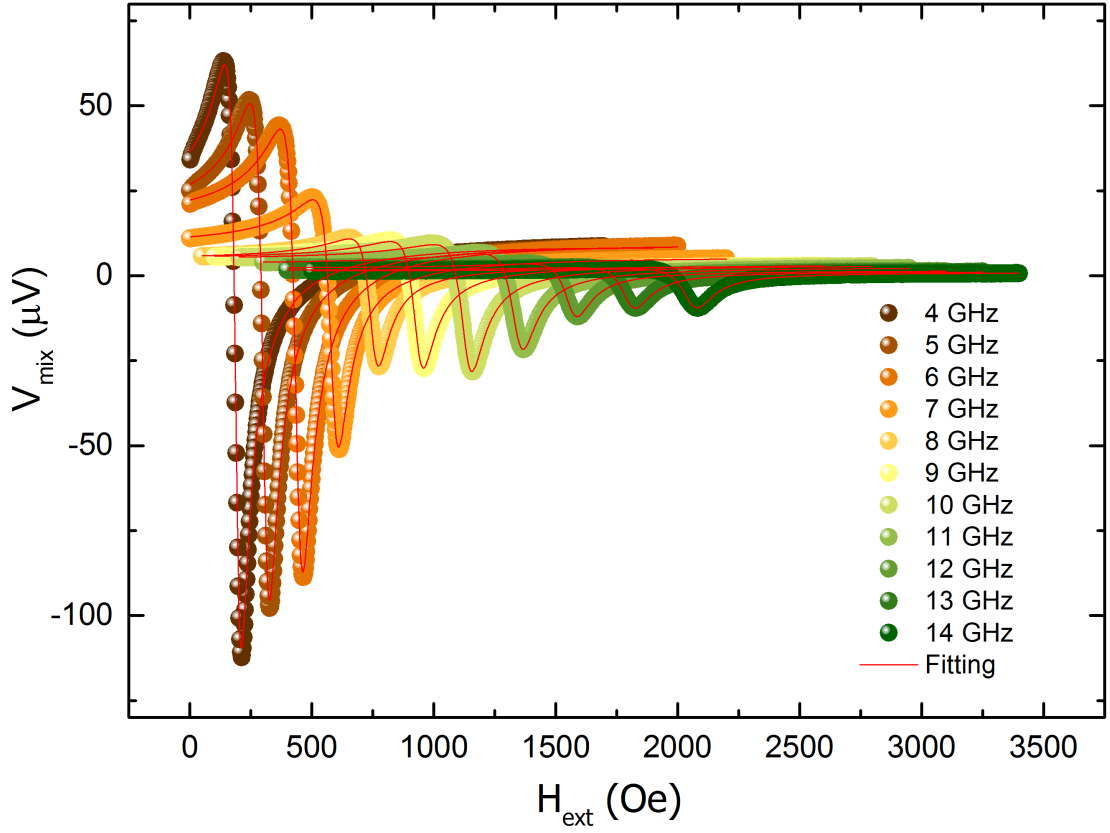


FIGURE 5.5: ST-FMR spectra measured on a 10 QL $\text{Bi}_2\text{Te}_3/5$ nm Py sample versus external magnetic field H_{ext} . Solid lines represent fits.

the demagnetization field $4\pi M_{\text{eff}}$ can be determined. In parallel, we measure M_s by superconducting quantum interference device (SQUID) magnetometry for a 30-nm Py film. For the size and shape of devices used here, M_s measured by SQUID of test sample is in agreement with M_{eff} determined by fitting to the FMR resonance field, whereas the demagnetization field can deviate from M_s for nanoscopic devices or strange shapes.

We have performed similar measurements on sets of samples with Bi_2Te_3 thicknesses of $t=3$ QL, 5 QL, 8 QL and 10 QL while the thickness of the magnetic layer Py is fixed at 5 nm. For each film thickness, spin Hall angle was extracted from the ST-FMR measurements using equation 5.3. Fig. 5.7 is a summary of

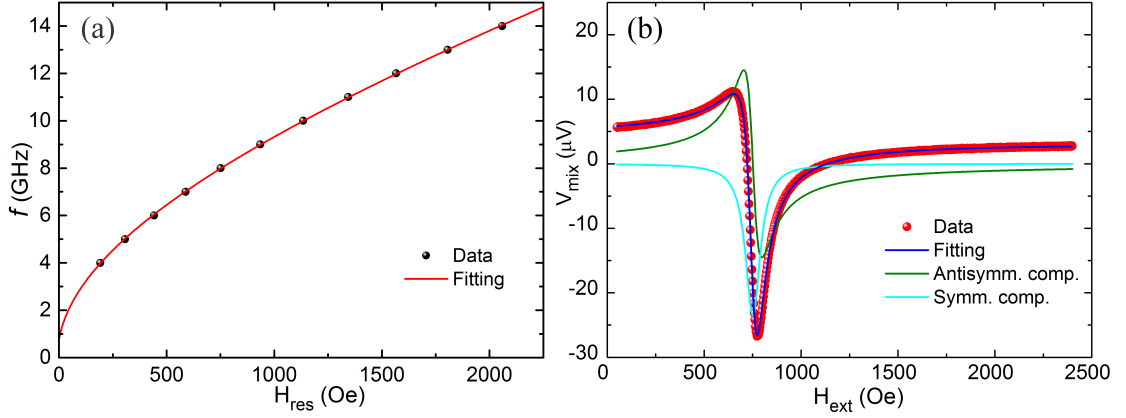


FIGURE 5.6: (a) Fitting curve for M_{eff} by using the Kittel formula and (b) a typical mixing voltage signal at resonance, showing the fit and its two components: the black solid line is fit to the data using equation 5.2 where the blue and green lines are the symmetric and antisymmetric Lorentzian fits.

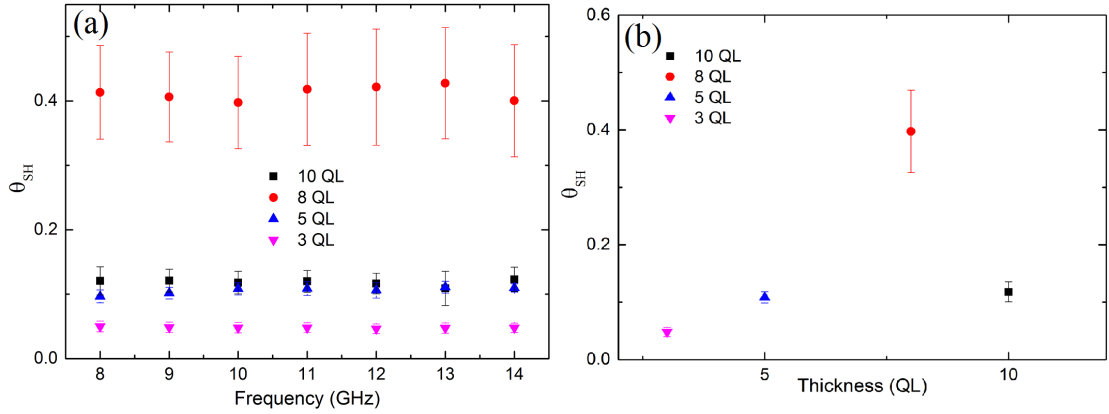


FIGURE 5.7: SHA of Bi_2Te_3 films on STO substrate. (a) The frequency dependence and (b) the thickness dependence of SHA for 3 QL, 5 QL, 8 QL, 10 QL Bi_2Te_3 with 5 nm Py, respectively.

SHA calculated for various thickness of Bi_2Te_3 (t)/Py (5 nm) thin films. The value of SHA shows little variation with frequency in the high frequency regime, but changes below 6 GHz. As we can see from Fig. 5.5, the spectra curves do not reach flat until zero field when the frequency is below 6 GHz, which cannot provide a good background for the consequent fitting. This can lead to the uncertainty of parameters extracted from the fitting results. These compare favorably with

reports previously reported by M Jamali et al [123], who reported values of SHA characterized from ST-FMR at high frequencies of 0.3 (increasing to 1.7 at low measurement frequencies) for a Bi_2Se_3 (10 QL)/CoFeB (5 nm) bilayer.

The SHA extracted from ST-FMR measurements performed at high frequencies show a dependence on the thickness of our TI layers. For the Bi_2Te_3 (3 QL)/Py (5 nm) bilayer, the value of SHA is about 0.05 whereas it is about 0.4 for Bi_2Te_3 (8 QL)/Py (5 nm) bilayer. However, to the best of our knowledge, there is no report about the thickness-dependent spin-to-charge conversion on Bi_2Te_3 . Instead, in Table 5.1, we compare with SHA in the family of 3D topological insulators, which share similar properties with Bi_2Te_3 .

TABLE 5.1: Comparison of SHA in topological insulators.

Material structures	Sample growth	Measurement technique	θ_{SH}	References
Bi_2Se_3 (10 QL/5 QL)/ CoFeB(5 nm)	MBE	Spin pumping	0.43	Ref.[123]
Bi_2Se_3 (8 QL)/ Py(16 nm)	MBE	ST-FMR	2.0-3.5	Ref.[124]
Bi_2Se_3 (9 QL)	MBE	Scanning photovoltage microscope	0.0085	Ref.[125]
Bi_2Se_3 (20 QL)/ Py (20 nm)	MBE	Spin pumping	0.0093	Ref.[126]
$(\text{Bi}_{0.5}\text{Sb}_{0.5})_2\text{Te}_3$ (3 QL) / $(\text{Cr}_{0.08}\text{Bi}_{0.54}\text{Sb}_{0.38})_2\text{Te}_3$ (6 QL)	MBE	Second- harmonic	140-425	Ref.[127]
Bi_2Se_3 (20 QL)/ CoFeB(5 nm)	MBE	ST-FMR	0.047	Ref.[128]
Bi_2Te_3 (6 QL)/ CoFeB(1 nm)	MBE	Second harmonic and MOKE	1.76	Ref.[129]

As can be seen in Table 5.1, the value of SHA varies with the film thickness and measurement techniques. Except for the large values of θ_{SH} in TI reported in

Ref. [124] and Ref.[127], the values are comparable with our values of θ_{SH} ranging from ~ 0.05 to ~ 0.4 with different thickness, are also consistent with the smaller values.

The method we used above is line-shape analysis. We also employed an alternative technique of ST-FMR called line-width analysis as an independent check. Line-width analysis is based on measuring changes in the linewidth as a function of applied DC current. The linewidth H_{pp} can be written as

$$H_{pp} = \frac{2\pi f}{\gamma} \left(\alpha + \frac{\sin\theta}{(H_{ext} + 2\pi M_{eff})\mu_0 M_{st}} \frac{\hbar J_s}{2e} \right) \quad (5.4)$$

To determine θ_{SH} by equation 5.4, it can be further expressed as

$$\theta_{SH} = \frac{\delta H_{pp}/\delta I_{dc}}{\frac{2\pi f}{\gamma} \frac{\sin\theta}{(H_{ext} + 2\pi M_{eff})\mu_0 M_{st}} \frac{\hbar}{2e}} \frac{R_{FM} + R_{TI}}{R_{FM}} A_C \quad (5.5)$$

R_{FM} and R_{TI} are the resistances of the ferromagnetic layer and TI layer, respectively, and A_C is the cross-sectional area of the device. By fitting the data shown in Fig. 5.8, the slope $\delta\Delta H_{pp}/\delta I_{dc}$ can be determined. By using Eq. 5.5, θ_{SH} can be calculated. As for the sample Bi_2Te_3 (5 QL)/Py (5 nm), this yields $\theta_{SH} \sim 0.064$ which agrees with the value determined from the FMR line shape analysis. Having confirmed the agreement between the two measurement techniques, we only use line-shape results for the discussions of thickness-dependent SHA in the next section.

We also grew several Bi_2Te_3 /Py bilayers on $\text{Al}_2\text{O}_3(0001)$ substrates and measured SHA in these films, as show in Fig. 5.9. The value of SHA shows similar tendency with the films grown on $\text{STO}(111)$ substrates. This can be explained by the fact that the main role of changing the substrate would be to seed a slightly different

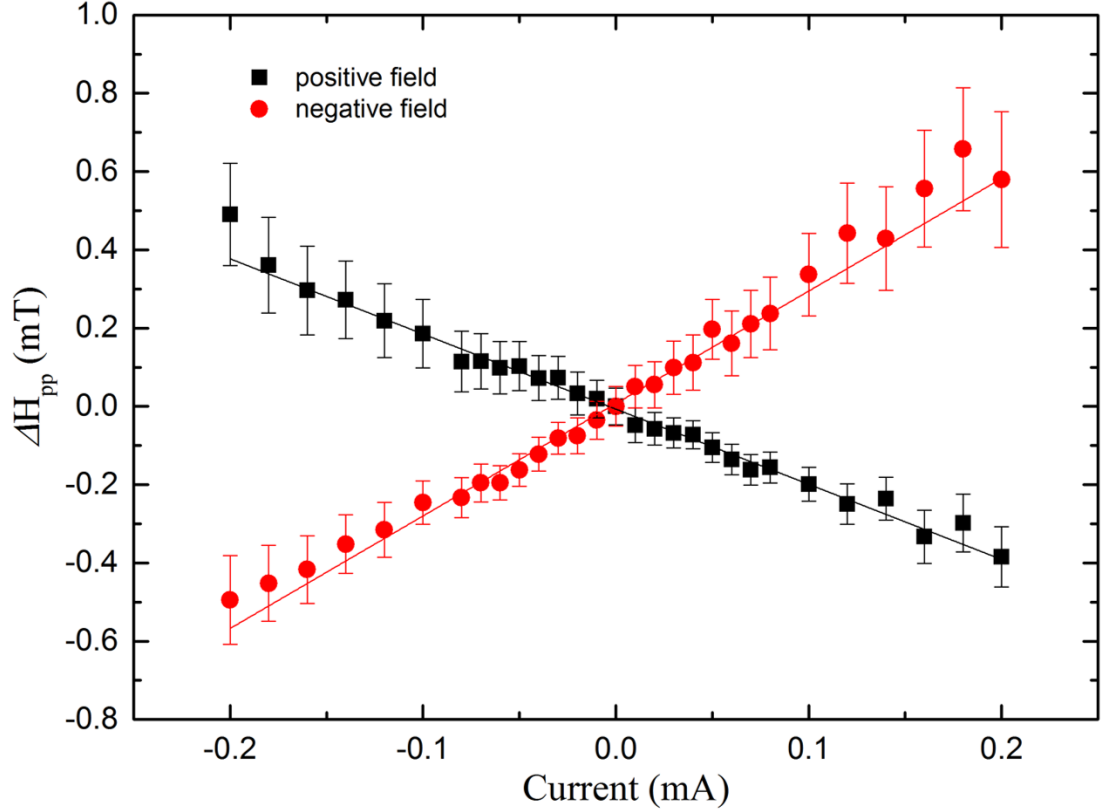


FIGURE 5.8: Change of linewidth (ΔH_{pp}) versus DC current for $\text{Bi}_2\text{Te}_3(5 \text{ QL})/\text{Py}(5 \text{ nm})$ at 8 GHz.

growth quality into the Bi_2Te_3 film, however, the similar values of SHA suggest that Bi_2Te_3 films grown on both Al_2O_3 and STO have similar properties. This is confirmed by the structural measurements of the films reported above, which confirm a similar crystal structure quality for both set of samples.

In addition, the samples with stack $\text{Al}_2\text{O}_3/\text{Bi}_2\text{Te}_3(3 \text{ QL}/5 \text{ QL})/\text{Py}(5 \text{ nm})$ underwent ST-FMR measurements performed in the PPMS at low temperature. Fig. 5.10 shows ST-FMR spectra measured on 5 QL $\text{Bi}_2\text{Te}_3/5 \text{ nm Py}$ bilayers at different temperatures for RF frequencies varying between 5 and 12 GHz. V_{mix} is plotted versus H_{ext} for various RF frequencies f . The method to fit the curves to symmetric and anti-symmetric components is the same as the former. Then we

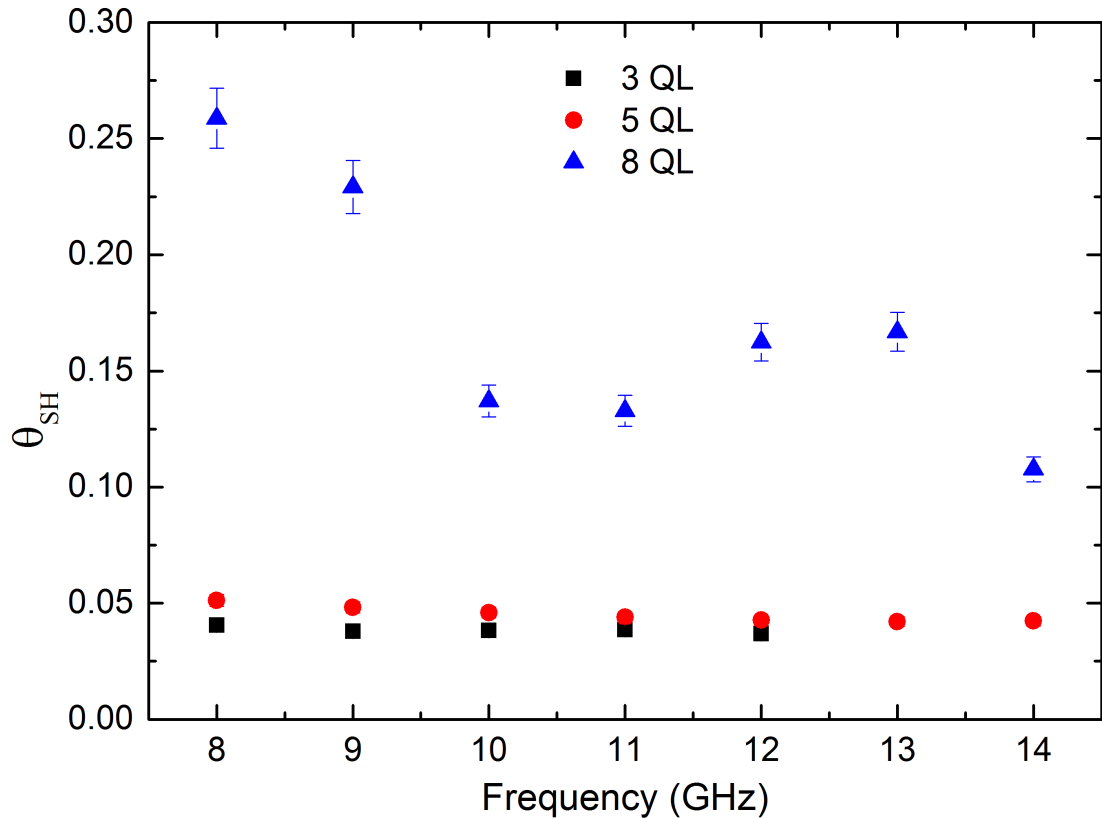


FIGURE 5.9: The frequency dependence of measured SHA for 3 QL, 5 QL, 8 QL Bi₂Te₃ with 5 nm Py on Al₂O₃ substrate, respectively.

calculated the SHA as shown in Fig. 5.11. The value of SHA at 4 K is bigger than that at 300 K for those two devices.

5.4 Discussion

TI/FM heterostructures have drawn much attention since A. R. Mellnik et al. [124] first reported the large SHA found in a Bi₂Se₃ thin film. The discussions are mainly focused on the mechanism of the charge-spin conversion in TIs. It is reported that a current-induced spin accumulation is produced due to spin-momentum locking of the topological insulator surface state [123, 124, 127, 130, 131]. Meanwhile, another

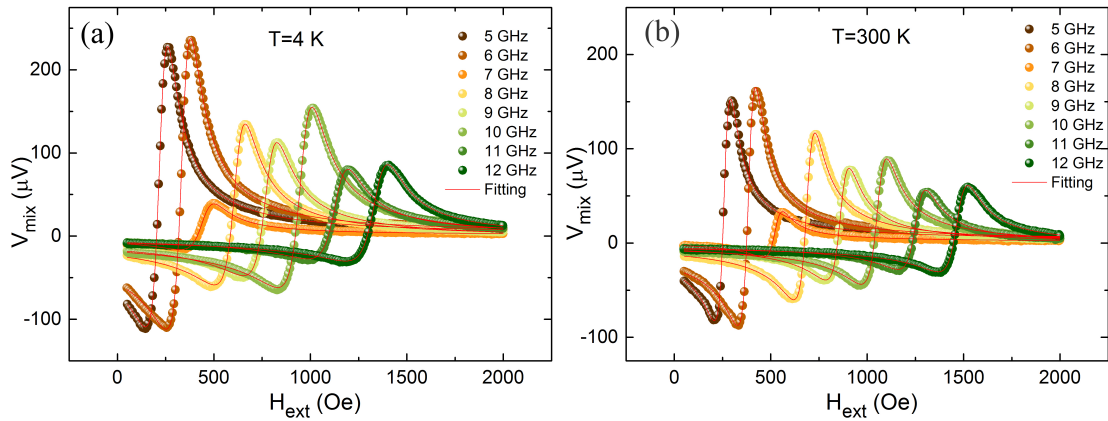


FIGURE 5.10: ST-FMR spectra measured on a 5 QL $\text{Bi}_2\text{Te}_3/5$ nm Py device versus external magnetic field H_{ext} at (a) 4 K and (b) 300 K. Solid lines represent fits.

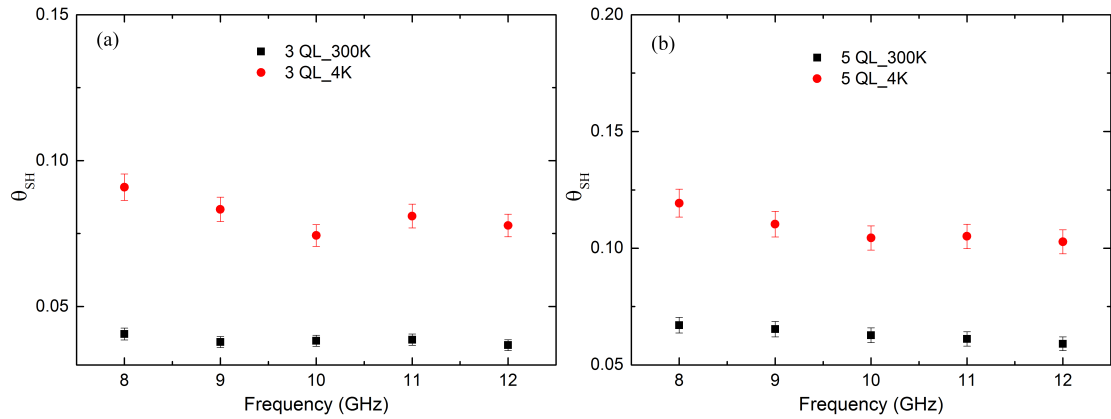


FIGURE 5.11: The frequency dependence of SHA measured at 4 K and 300 K for (a) 3 QL and (b) 5 QL Bi_2Te_3 with 5 nm Py on Al_2O_3 substrate, respectively

feature of TIs is the bulk behavior as a semiconductor. A perfect semiconductor will conduct poorly and generate a small contribution to SHE, but in reality the TI thin films are defective semiconductors with metallic-like behavior, which can contribute to spin accumulation via SHE as well [125, 126, 132, 133]. Furthermore, the Edelstein-Rashba effect can also play a role in the spin accumulation [123, 127, 128, 132, 134–137].

In our case, we performed thickness-dependent ST-FMR measurements on $\text{Bi}_2\text{Te}_3/\text{Py}$

bilayers with the thickness of Bi_2Te_3 ranging from 3-10 QL. The choice of thickness range is based on three reasons. Firstly, it is reported the topological features start to appear above 2 QL [108] for Bi_2Te_3 . Secondly, it is noted that Zhang, J. et al. [138] reported the coupling between the top and bottom surfaces for ultrathin films of Bi_2Te_3 with thickness $d < 4$ QL. Thirdly, there is experimental evidence [110] showing thickness-independent transport channels in Bi_2Se_3 thin films from 256 QL down to 8 QL, but changing from 8 QL to 2 QL.

Theoretically, a 3D topological insulator only has a metallic surface state and the bulk is insulating. However, such ideal thin film is hard to obtain experimentally because defects occurring during film growth contribute bulk charge carriers.

In chapter 4, we studied the transport properties on Bi_2Te_3 thin films with different thickness. The resistivity versus temperature of the film with a 5 QL thickness shows different properties from those with 10 QL and 20 QL thicknesses below 20 K, which is similar to the results shown in Ref. [110], with this observation suggesting the resistivity is dominated by some surface transport channels.

Here, Bansal et al. [110] also measured the Hall effect and claimed the surface transport channel as a combination of topological surface states and 2DEG channels, since they observed non-linear R_{xy} vs H curves characteristic of multi-band carriers. In our case, we observed a linear line for R_{xy} vs H . The carrier density and electron mobility remains almost constant for entire temperature range 2 K - 300 K for 5 QL, which suggests surface-dominated transport. For 10 QL and 20 QL, the carrier density slightly increases with increasing temperature, while the electron mobility decreases. This observation suggests bulk conduction starts to play a role in thicker films.

Having demonstrated that transport is dominated by surface states in our Bi_2Te_3 films with thickness less than 10 QL, we note that our Bi_2Te_3 film has two surfaces,

however, the bottom surface has contributions to the spin accumulations with a sign opposite that of the upper surface. So the spin accumulation increases with the film thickness due to the diminished cancellation of the spin accumulation from the bottom surface [139]. For the thickness of 3 QL and 5 QL, the bulk state can be neglected and the spin accumulation is dominated by surface channels. However, the spin torque efficiency is low which is caused by the coupling between top and bottom surfaces. On the other hand, the spin accumulation may increase with the film thickness due to the diminished cancellation of the spin accumulation from the bottom surface [139]. Therefore, when the thickness increases to 8 QL, the surfaces coupling diminishes and vanishes, and the value of SHA reaches the peak around the 8 QL thickness. As the thickness is increased to 10 QL, the value of SHA decreases. This is because, as discussed above, at thickness of 10 QL conducting bulk states are found in our Bi_2Te_3 films. A portion of current will therefore flow in these states as opposed to the spin-momentum locked surface states, thus reducing the efficiency of charge-to-spin current conversion. It is worthy to note that there are several reports [125, 133, 137, 140] about the thickness-dependent spin-charge-conversion on Bi_2Se_3 , with thickness ranging from 2-20 QL, which all illustrate the similar tendency with our results. Due to different measurement techniques and the quality of materials, the critical thickness of TI varies slightly from 6-9 QL. It has also been experimentally shown that bulk states may diminish the spin accumulation torques [125, 140–145]. However, we note that here we present the first reports of thickness dependence of SHA in Bi_2Te_3 thin films, finding a maximum of charge-to-spin current conversion efficiency at a thickness of 8 QL.

Finally, the SHA measured at 4 K and 300 K for 3 QL and 5 QL Bi_2Te_3 with 5 nm Py is an evidence for the surface contribution to the SHA. The values of SHA measured at 4 K are bigger than that at 300 K, which highlights the dominant

contributions of the surface state channels, since the bulk electrons freeze out at low temperatures and do not contribute to the charge-to-spin conversion.

Chapter 6

Summary and Outlook

6.1 Summary

We start this dissertation describing in detail the epitaxial growth of Bi_2Te_3 thin film. We introduce UHV technique which is essential for growing highly pure thin films and describe the design and implementation of a MBE system for telluride-based topological insulators. The mechanism of TI growth is then briefly described. With a large flux ratio of Te/Bi (8-20) being set, the growth is mainly controlled by the temperature of substrate and flux of Bi. Through systematic experiments, we developed an optimized growth recipe for Bi_2Te_3 film grown both on STO(111) substrate and Al_2O_3 substrate. The structure and morphology of the films are characterized by using both *in-situ* and *ex-situ* methods.

In a second stage we perform electrical transport measurements on these well-grown thin films in PPMS. For the film of 5 QL in thickness, the inferred carrier density and electron mobility show almost temperature-independent with temperature ranging from 2 K - 300 K. On the other hand, the carrier density increases

and electron mobility decrease with increasing temperature from 2 K to 300 K for the films of 10 QL and 20 QL in thickness. This observation suggests the surface dominated transport channel for the thinner film, which is important for explaining the STFMR results in next section.

In chapter 5, we measure SHA of Bi_2Te_3 thin films by ST-FMR. Lineshape analysis is used for all tested samples and we have cross check their validity also by linewidth analysis. The values obtained from the two analysis methods agree well. We find the value of SHA is thickness dependent. With thickness increasing from 3 QL to 10 QL, the SHA increases first and reaches maximum at 8 QL, then decreases at 10 QL. It can be understood as the different contributions of spin accumulation from surface channels and bulk state. For the thickness of 3 QL and 5 QL, the coupling between top and bottom surfaces reduces the spin accumulation. When the thickness increases to 8 QL, the surfaces coupling diminishes and vanishes, so the value increases. As for 10 QL, the bulk state play a more important role than the other three samples and the decreased value is a sign that the bulk state reduces the effective spin accumulation. To support this assumption, we measure two samples at temperature 4 K and 300 K, respectively. The SHA at 4 K is bigger than at 300 K, which indicates that the surface contribution is dominant in the charge-to-spin conversion process..

6.2 Outlook

The aim of this dissertation is to understand the spin-charge conversion in TIs by coupling to a magnetic layer. All the research results we present in this dissertation indicate the key role of the surface states, yet more efforts are required to deeply understand the mechanism and improve the SHA for device applications.

It is important to create real bulk insulating thin films, but it is hard due to the intrinsic defects. An alternative way is to grow antimony doped Bi_2Te_3 . Truly insulating bulk and tunable surface states can be achieved via band structure engineering. Moreover, TIs are highly resistive comparing to the normal magnetic layer (permalloy, cobalt, et al.) we used, which leads the charge current flowing mostly from the conductive layer. It is meaningful to try couple TIs to ferromagnetic insulators. On the other hand, there are reports on large spin-orbit torque in Cr-doped TI which can be further developed. Beyond understanding the charge-to-spin conversion in TIs, a very exciting research direction is to study the quantum anomalous Hall effect (QAHE) in magnetic TIs. The experimental observation of the QAHE in a magnetic TI was first reported by C. Chang et al. [109] in 2013, but it can only be observed in extremely low temperature which is limited to 2 K [146, 147]. It is of great interest to realize the QAHE at higher temperature, which is necessary for applications such as dissipationless spintronics and low-energy electronics technologies [148, 149].

Appendix A

Cleaning of $\text{Al}_2\text{O}_3(0001)$

Substrates

- 1) Soak the substrate in ethanol for 12 hours.
- 2) Clean the substrate in ultrasonic bath of acetone or isopropanol for 10 minutes to remove bulky dissolvable contaminants and particulates materials.
- 3) Rinse thoroughly in deionized water thoroughly and blow with dry nitrogen gas.
- 4) Heat the substrate in $\text{NH}_4\text{OH} : \text{H}_2\text{O}_2 : \text{H}_2\text{O} = 1 : 1 : 5$ to about $80\text{ }^\circ\text{C}$ for 10 minutes. NH_4^+ ion in the cleaning solution will complex with heavy metal on the substrate surface to form a soluble metal salts which is removed.
- 5) Rinse thoroughly in deionized water thoroughly and dry with pure nitrogen gas.
- 6) Soak the substrate in solution of HCl (hydrochloric acid): $\text{H}_2\text{O}_2 : \text{H}_2\text{O} = 1 : 1 : 3$ at about $80\text{ }^\circ\text{C}$ for 10 minutes. H^+ ion in the cleaning solution will replace with the light metal impurities to form soluble salt and be removed.

- 7) Rinse thoroughly in DI water thoroughly and dry with pure nitrogen gas.
- 8) Clean in H₂SO₄ (sulphuric acid): H₃PO₄ (orthophosphoric acid)=1:3 at about 250 °C for 10minutes to move the oxide layer on the sapphire substrate.
- 9) Fully rinse with deionized water and dry with a stream of high speed pure nitrogen.
- 11) Annealing in the atmosphere furnace for 3 hours at 1200 °C to gain atomically flat surface.

Bibliography

- [1] C.-Z. Chang and M. Li, “Quantum anomalous hall effect in time-reversal-symmetry breaking topological insulators,” *Journal of Physics: Condensed Matter*, vol. 28, no. 12, p. 123002, 2016.
- [2] K. Von Klitzing, “The quantized hall effect,” *Reviews of Modern Physics*, vol. 58, no. 3, p. 519, 1986.
- [3] B. A. Bernevig, T. L. Hughes, and S.-C. Zhang, “Quantum spin hall effect and topological phase transition in hgte quantum wells,” *Science*, vol. 314, no. 5806, pp. 1757–1761, 2006.
- [4] C. H. Li, O. M. J. van âEUR~t Erve, Y. Y. Li, L. Li, and B. T. Jonker, “Electrical detection of the helical spin texture in a p-type topological insulator sb2te3,” *Scientific Reports*, vol. 6, no. 1, p. 29533, 2016.
- [5] D. Hsieh, Y. Xia, D. Qian, L. Wray, J. H. Dil, F. Meier, J. Osterwalder, L. Patthey, J. G. Checkelsky, N. P. Ong, A. V. Fedorov, H. Lin, A. Bansil, D. Grauer, Y. S. Hor, R. J. Cava, and M. Z. Hasan, “A tunable topological insulator in the spin helical dirac transport regime,” *Nature*, vol. 460, no. 7259, pp. 1101–1105, 2009.
- [6] S. Parkin and S.-H. Yang, “Memory on the racetrack,” *Nature Nanotechnology*, vol. 10, no. 3, pp. 195–198, 2015.
- [7] F. Tang, T. Parker, G. Wang, and T. Lu, “Surface texture evolution of polycrystalline and nanostructured films: Rheed surface pole figure analysis,” *Journal of Physics D: Applied Physics*, vol. 40, no. 23, p. R427, 2007.

-
- [8] A. Handbook, “Vol. 3: alloy phase diagrams,” *ASM International, Materials Park, OH, USA*, vol. 2, p. 48, 1992.
- [9] Y. Chen, J. G. Analytis, J.-H. Chu, Z. Liu, S.-K. Mo, X.-L. Qi, H. Zhang, D. Lu, X. Dai, Z. Fang, *et al.*, “Experimental realization of a three-dimensional topological insulator, Bi_2Te_3 ,” *science*, vol. 325, no. 5937, pp. 178–181, 2009.
- [10] W. Zhang, *Charge to Spin Current Efficiency Studied by Spin Torque Ferromagnetic Resonance in Various Metal Heterostructures*. Stanford University, 2015.
- [11] B. A. Bernevig, T. L. Hughes, and S.-C. Zhang, “Quantum spin hall effect and topological phase transition in hgte quantum wells,” *science*, vol. 314, no. 5806, pp. 1757–1761, 2006.
- [12] K. v. Klitzing, G. Dorda, and M. Pepper, “New method for high-accuracy determination of the fine-structure constant based on quantized hall resistance,” *Phys. Rev. Lett.*, vol. 45, pp. 494–497, Aug 1980.
- [13] C. L. Kane and E. J. Mele, “ \mathbb{Z}_2 topological order and the quantum spin hall effect,” *Physical review letters*, vol. 95, no. 14, p. 146802, 2005.
- [14] C. L. Kane and E. J. Mele, “ \mathbb{Z}_2 topological order and the quantum spin hall effect,” *Phys. Rev. Lett.*, vol. 95, p. 146802, Sep 2005.
- [15] C. L. Kane and E. J. Mele, “Quantum spin hall effect in graphene,” *Phys. Rev. Lett.*, vol. 95, p. 226801, Nov 2005.
- [16] M. König, S. Wiedmann, C. Brüne, A. Roth, H. Buhmann, L. W. Molenkamp, X.-L. Qi, and S.-C. Zhang, “Quantum spin hall insulator state in hgte quantum wells,” *Science*, vol. 318, no. 5851, pp. 766–770, 2007.
- [17] A. Roth, C. Brüne, H. Buhmann, L. W. Molenkamp, J. Maciejko, X.-L. Qi, and S.-C. Zhang, “Nonlocal transport in the quantum spin hall state,” *Science*, vol. 325, no. 5938, pp. 294–297, 2009.

-
- [18] L. Fu, C. L. Kane, and E. J. Mele, “Topological insulators in three dimensions,” *Phys. Rev. Lett.*, vol. 98, p. 106803, Mar 2007.
- [19] J. E. Moore and L. Balents, “Topological invariants of time-reversal-invariant band structures,” *Phys. Rev. B*, vol. 75, p. 121306, Mar 2007.
- [20] R. Roy, “Topological phases and the quantum spin hall effect in three dimensions,” *Phys. Rev. B*, vol. 79, p. 195322, May 2009.
- [21] L. Fu and C. L. Kane, “Topological insulators with inversion symmetry,” *Phys. Rev. B*, vol. 76, p. 045302, Jul 2007.
- [22] H.-J. Zhang, C.-X. Liu, X.-L. Qi, X.-Y. Deng, X. Dai, S.-C. Zhang, and Z. Fang, “Electronic structures and surface states of the topological insulator $\text{bi}_{1-x}\text{sb}_x$,” *Phys. Rev. B*, vol. 80, p. 085307, Aug 2009.
- [23] D. Hsieh, D. Qian, L. Wray, Y. Xia, Y. S. Hor, R. J. Cava, and M. Z. Hasan, “A topological dirac insulator in a quantum spin hall phase,” *Nature*, vol. 452, no. 7190, pp. 970–974, 2008.
- [24] M. Z. Hasan and C. L. Kane, “Colloquium: topological insulators,” *Reviews of modern physics*, vol. 82, no. 4, p. 3045, 2010.
- [25] H. Zhang, C.-X. Liu, X.-L. Qi, X. Dai, Z. Fang, and S.-C. Zhang, “Topological insulators in bi_2se_3 , bi_2te_3 and sb_2te_3 with a single dirac cone on the surface,” *Nature Physics*, vol. 5, no. 6, pp. 438–442, 2009.
- [26] Y. Xia, D. Qian, D. Hsieh, L. Wray, A. Pal, H. Lin, A. Bansil, D. Grauer, Y. S. Hor, R. J. Cava, and M. Z. Hasan, “Observation of a large-gap topological-insulator class with a single dirac cone on the surface,” *Nature Physics*, vol. 5, no. 6, pp. 398–402, 2009.
- [27] Y. L. Chen, J. G. Analytis, J.-H. Chu, Z. K. Liu, S.-K. Mo, X. L. Qi, H. J. Zhang, D. H. Lu, X. Dai, Z. Fang, S. C. Zhang, I. R. Fisher, Z. Hussain, and Z.-X. Shen, “Experimental realization of a three-dimensional topological insulator, bi_2te_3 ,” *Science*, vol. 325, no. 5937, pp. 178–181, 2009.

- [28] S.-Y. Xu, L. A. Wray, Y. Xia, R. Shankar, S. Jia, A. Fedorov, J. H. Dil, F. Meier, B. Slomski, J. Osterwalder, R. J. Cava, and M. Z. Hasan, “Observation of topological order in the $tlbise_2$ class : Probing the ”spin” and ”phase” on topological insulator surfaces,” 2010.
- [29] H. Lin, R. S. Markiewicz, L. A. Wray, L. Fu, M. Z. Hasan, and A. Bansil, “Single-dirac-cone topological surface states in the $tlbise_2$ class of topological semiconductors,” *Phys. Rev. Lett.*, vol. 105, p. 036404, Jul 2010.
- [30] Y. L. Chen, Z. K. Liu, J. G. Analytis, J.-H. Chu, H. J. Zhang, B. H. Yan, S.-K. Mo, R. G. Moore, D. H. Lu, I. R. Fisher, S. C. Zhang, Z. Hussain, and Z.-X. Shen, “Single dirac cone topological surface state and unusual thermoelectric property of compounds from a new topological insulator family,” *Phys. Rev. Lett.*, vol. 105, p. 266401, Dec 2010.
- [31] T. Sato, K. Segawa, K. Kosaka, S. Souma, K. Nakayama, K. Eto, T. Minami, Y. Ando, and T. Takahashi, “Unexpected mass acquisition of dirac fermions at the quantum phase transition of a topological insulator,” *Nature Physics*, vol. 7, no. 11, pp. 840–844, 2011.
- [32] B. Yan, L. MÜchler, and C. Felser, “Prediction of weak topological insulators in layered semiconductors,” *Phys. Rev. Lett.*, vol. 109, p. 116406, Sep 2012.
- [33] B. Yan, M. Jansen, and C. Felser, “A large-energy-gap oxide topological insulator based on the superconductor $babio_3$,” *Nature Physics*, vol. 9, no. 11, pp. 709–711, 2013.
- [34] M. Dzero and V. Galitski, “A new exotic state in an old material: a tale of smb_6 ,” *Journal of Experimental and Theoretical Physics*, vol. 117, pp. 499–507, Sep 2013.
- [35] M. Neupane, N. Alidoust, S.-Y. Xu, T. Kondo, Y. Ishida, D. J. Kim, C. Liu, I. Belopolski, Y. J. Jo, T.-R. Chang, H.-T. Jeng, T. Durakiewicz, L. Balicas, H. Lin, A. Bansil, S. Shin, Z. Fisk, and M. Z. Hasan, “Surface electronic structure of the topological kondo-insulator candidate correlated electron system smb_6 ,” *Nature Communications*, vol. 4, no. 1, p. 2991, 2013.

-
- [36] E. Frantzeskakis, N. de Jong, B. Zwartsenberg, Y. K. Huang, Y. Pan, X. Zhang, J. X. Zhang, F. X. Zhang, L. H. Bao, O. Tegus, A. Varykhalov, A. de Visser, and M. S. Golden, “Kondo hybridization and the origin of metallic states at the (001) surface of SmB_6 ,” *Phys. Rev. X*, vol. 3, p. 041024, Dec 2013.
- [37] D. J. Kim, J. Xia, and Z. Fisk, “Topological surface state in the kondo insulator samarium hexaboride,” *Nature Materials*, vol. 13, no. 5, pp. 466–470, 2014.
- [38] A. A. Burkov and D. G. Hawthorn, “Spin and charge transport on the surface of a topological insulator,” *Phys. Rev. Lett.*, vol. 105, p. 066802, Aug 2010.
- [39] O. V. Yazyev, J. E. Moore, and S. G. Louie, “Spin polarization and transport of surface states in the topological insulators Bi_2Se_3 and Bi_2Te_3 from first principles,” *Phys. Rev. Lett.*, vol. 105, p. 266806, Dec 2010.
- [40] S. Souma, K. Kosaka, T. Sato, M. Komatsu, A. Takayama, T. Takahashi, M. Kriener, K. Segawa, and Y. Ando, “Direct measurement of the out-of-plane spin texture in the dirac-cone surface state of a topological insulator,” *Phys. Rev. Lett.*, vol. 106, p. 216803, May 2011.
- [41] Z.-H. Pan, E. Vescovo, A. V. Fedorov, D. Gardner, Y. S. Lee, S. Chu, G. D. Gu, and T. Valla, “Electronic structure of the topological insulator Bi_2Se_3 using angle-resolved photoemission spectroscopy: Evidence for a nearly full surface spin polarization,” *Phys. Rev. Lett.*, vol. 106, p. 257004, Jun 2011.
- [42] J. W. McIver, D. Hsieh, H. Steinberg, P. Jarillo-Herrero, and N. Gedik, “Control over topological insulator photocurrents with light polarization,” *Nature Nanotechnology*, vol. 7, no. 2, pp. 96–100, 2012.
- [43] Y. Ando, T. Hamasaki, T. Kurokawa, K. Ichiba, F. Yang, M. Novak, S. Sasaki, K. Segawa, Y. Ando, and M. Shiraishi, “Electrical detection of the spin polarization due to charge flow in the surface state of the topological insulator $\text{Bi}_{1.5}\text{Sb}_{0.5}\text{Te}_{1.7}\text{Se}_{1.3}$,” *Nano Letters*, vol. 14, pp. 6226–6230, Nov 2014.

-
- [44] C. H. Li, O. M. J. van âEUR~t Erve, J. T. Robinson, Y. Liu, L. Li, and B. T. Jonker, “Electrical detection of charge-current-induced spin polarization due to spin-momentum locking in Bi_2Se_3 ,” *Nature Nanotechnology*, vol. 9, no. 3, pp. 218–224, 2014.
- [45] J. Tang, L.-T. Chang, X. Kou, K. Murata, E. S. Choi, M. Lang, Y. Fan, Y. Jiang, M. Montazeri, W. Jiang, Y. Wang, L. He, and K. L. Wang, “Electrical detection of spin-polarized surface states conduction in $(\text{Bi}_{0.53}\text{Sb}_{0.47})_2\text{Te}_3$ topological insulator,” *Nano Letters*, vol. 14, pp. 5423–5429, Sep 2014.
- [46] A. Dankert, J. Geurs, M. V. Kamalakar, S. Charpentier, and S. P. Dash, “Room temperature electrical detection of spin polarized currents in topological insulators,” *Nano Letters*, vol. 15, pp. 7976–7981, Dec 2015.
- [47] Y. Cao, J. A. Waugh, X.-W. Zhang, J.-W. Luo, Q. Wang, T. J. Reber, S. K. Mo, Z. Xu, A. Yang, J. Schneeloch, G. D. Gu, M. Brahlek, N. Bansal, S. Oh, A. Zunger, and D. S. Dessau, “Mapping the orbital wavefunction of the surface states in three-dimensional topological insulators,” *Nature Physics*, vol. 9, no. 8, pp. 499–504, 2013.
- [48] S.-Y. Xu, Y. Xia, L. A. Wray, S. Jia, F. Meier, J. H. Dil, J. Osterwalder, B. Slomski, A. Bansil, H. Lin, R. J. Cava, and M. Z. Hasan, “Topological phase transition and texture inversion in a tunable topological insulator,” *Science*, vol. 332, no. 6029, pp. 560–564, 2011.
- [49] J. Han, A. Richardella, S. A. Siddiqui, J. Finley, N. Samarth, and L. Liu, “Room-temperature spin-orbit torque switching induced by a topological insulator,” *Phys. Rev. Lett.*, vol. 119, p. 077702, Aug 2017.
- [50] Y. Wang, D. Zhu, Y. Wu, Y. Yang, J. Yu, R. Ramaswamy, R. Mishra, S. Shi, M. Elyasi, K.-L. Teo, Y. Wu, and H. Yang, “Room temperature magnetization switching in topological insulator-ferromagnet heterostructures by spin-orbit torques,” *Nature Communications*, vol. 8, no. 1, p. 1364, 2017.

-
- [51] Y. Fan, P. Upadhyaya, X. Kou, M. Lang, S. Takei, Z. Wang, J. Tang, L. He, L.-T. Chang, M. Montazeri, G. Yu, W. Jiang, T. Nie, R. N. Schwartz, Y. Tserkovnyak, and K. L. Wang, “Magnetization switching through giant spinâneur” orbit torque in a magnetically doped topological insulator heterostructure,” *Nature Materials*, vol. 13, no. 7, pp. 699–704, 2014.
- [52] P. B. Ndiaye, C. A. Akosa, M. H. Fischer, A. Vaezi, E.-A. Kim, and A. Manchon, “Dirac spin-orbit torques and charge pumping at the surface of topological insulators,” *Phys. Rev. B*, vol. 96, p. 014408, Jul 2017.
- [53] S. Ghosh and A. Manchon, “Spin-orbit torque in a three-dimensional topological insulator–ferromagnet heterostructure: Crossover between bulk and surface transport,” *Phys. Rev. B*, vol. 97, p. 134402, Apr 2018.
- [54] Y. K. Kato, R. C. Myers, A. C. Gossard, and D. D. Awschalom, “Observation of the spin hall effect in semiconductors,” *Science*, vol. 306, no. 5703, pp. 1910–1913, 2004.
- [55] J. Wunderlich, B. Kaestner, J. Sinova, and T. Jungwirth, “Experimental observation of the spin-hall effect in a two-dimensional spin-orbit coupled semiconductor system,” *Phys. Rev. Lett.*, vol. 94, p. 047204, Feb 2005.
- [56] N. F. Mott and N. H. D. Bohr, “The scattering of fast electrons by atomic nuclei,” *Proceedings of the Royal Society of London. Series A, Containing Papers of a Mathematical and Physical Character*, vol. 124, no. 794, pp. 425–442, 1929.
- [57] M. I. Dyakonov and V. Perel, “Current-induced spin orientation of electrons in semiconductors,” *Physics Letters A*, vol. 35, no. 6, pp. 459–460, 1971.
- [58] J. Sinova, D. Culcer, Q. Niu, N. A. Sinitsyn, T. Jungwirth, and A. H. MacDonald, “Universal intrinsic spin hall effect,” *Phys. Rev. Lett.*, vol. 92, p. 126603, Mar 2004.

-
- [59] S. Murakami, N. Nagaosa, and S.-C. Zhang, “Dissipationless quantum spin current at room temperature,” *Science*, vol. 301, no. 5638, pp. 1348–1351, 2003.
- [60] K. Nomura, J. Wunderlich, J. Sinova, B. Kaestner, A. H. MacDonald, and T. Jungwirth, “Edge-spin accumulation in semiconductor two-dimensional hole gases,” *Phys. Rev. B*, vol. 72, p. 245330, Dec 2005.
- [61] V. Sih, R. C. Myers, Y. K. Kato, W. H. Lau, A. C. Gossard, and D. D. Awschalom, “Spatial imaging of the spin hall effect and current-induced polarization in two-dimensional electron gases,” *Nature Physics*, vol. 1, no. 1, pp. 31–35, 2005.
- [62] N. P. Stern, S. Ghosh, G. Xiang, M. Zhu, N. Samarth, and D. D. Awschalom, “Current-induced polarization and the spin hall effect at room temperature,” *Phys. Rev. Lett.*, vol. 97, p. 126603, Sep 2006.
- [63] V. Sih, W. H. Lau, R. C. Myers, V. R. Horowitz, A. C. Gossard, and D. D. Awschalom, “Generating spin currents in semiconductors with the spin hall effect,” *Phys. Rev. Lett.*, vol. 97, p. 096605, Sep 2006.
- [64] N. P. Stern, D. W. Steuerman, S. Mack, A. C. Gossard, and D. D. Awschalom, “Drift and diffusion of spins generated by the spin hall effect,” *Applied Physics Letters*, vol. 91, no. 6, p. 062109, 2007.
- [65] H. J. Chang, T. W. Chen, J. W. Chen, W. C. Hong, W. C. Tsai, Y. F. Chen, and G. Y. Guo, “Current and strain-induced spin polarization in InGaN/GaN superlattices,” *Phys. Rev. Lett.*, vol. 98, p. 136403, Mar 2007.
- [66] S. Matsuzaka, Y. Ohno, and H. Ohno, “Electron density dependence of the spin hall effect in gaas probed by scanning kerr rotation microscopy,” *Phys. Rev. B*, vol. 80, p. 241305, Dec 2009.
- [67] J. E. Hirsch, “Spin hall effect,” *Phys. Rev. Lett.*, vol. 83, pp. 1834–1837, Aug 1999.

- [68] E. Saitoh, M. Ueda, H. Miyajima, and G. Tatara, "Conversion of spin current into charge current at room temperature: Inverse spin-hall effect," *Applied Physics Letters*, vol. 88, no. 18, p. 182509, 2006.
- [69] S. O. Valenzuela and M. Tinkham, "Direct electronic measurement of the spin hall effect," *Nature*, vol. 442, no. 7099, pp. 176–179, 2006.
- [70] H. Zhao, E. J. Loren, H. M. van Driel, and A. L. Smirl, "Coherence control of hall charge and spin currents," *Phys. Rev. Lett.*, vol. 96, p. 246601, Jun 2006.
- [71] C. BrÅene, A. Roth, E. G. Novik, M. KÅnig, H. Buhmann, E. M. Hankiewicz, W. Hanke, J. Sinova, and L. W. Molenkamp, "Evidence for the ballistic intrinsic spin hall effect in hgte nanostructures," *Nature Physics*, vol. 6, no. 6, pp. 448–454, 2010.
- [72] K. Uchida, S. Takahashi, K. Harii, J. Ieda, W. Koshibae, K. Ando, S. Maekawa, and E. Saitoh, "Observation of the spin seebeck effect," *Nature*, vol. 455, no. 7214, pp. 778–781, 2008.
- [73] K. Uchida, J. Xiao, H. Adachi, J. Ohe, S. Takahashi, J. Ieda, T. Ota, Y. Kajiwara, H. Umezawa, H. Kawai, G. E. W. Bauer, S. Maekawa, and E. Saitoh, "Spin seebeck insulator," *Nature Materials*, vol. 9, no. 11, pp. 894–897, 2010.
- [74] C. M. Jaworski, J. Yang, S. Mack, D. D. Awschalom, J. P. Heremans, and R. C. Myers, "Observation of the spin-seebeck effect in a ferromagnetic semiconductor," *Nature Materials*, vol. 9, no. 11, pp. 898–903, 2010.
- [75] G. E. W. Bauer, E. Saitoh, and B. J. van Wees, "Spin caloritronics," *Nature Materials*, vol. 11, no. 5, pp. 391–399, 2012.
- [76] A. Fert and I. A. Campbell, "Electrical resistivity of ferromagnetic nickel and iron based alloys," *Journal of Physics F: Metal Physics*, vol. 6, pp. 849–871, may 1976.

-
- [77] A. Fert, “Two-current conduction in ferromagnetic metals and spin wave-electron collisions,” *Journal of Physics C: Solid State Physics*, vol. 2, pp. 1784–1788, oct 1969.
- [78] S. I. Kiselev, J. C. Sankey, I. N. Krivorotov, N. C. Emley, R. J. Schoelkopf, R. A. Buhrman, and D. C. Ralph, “Microwave oscillations of a nanomagnet driven by a spin-polarized current,” *Nature*, vol. 425, no. 6956, pp. 380–383, 2003.
- [79] I. N. Krivorotov, N. C. Emley, J. C. Sankey, S. I. Kiselev, D. C. Ralph, and R. A. Buhrman, “Time-domain measurements of nanomagnet dynamics driven by spin-transfer torques,” *Science*, vol. 307, no. 5707, pp. 228–231, 2005.
- [80] L. Berger, “Low-field magnetoresistance and domain drag in ferromagnets,” *Journal of Applied Physics*, vol. 49, no. 3, pp. 2156–2161, 1978.
- [81] J. Slonczewski, “Current-driven excitation of magnetic multilayers,” *Journal of Magnetism and Magnetic Materials*, vol. 159, no. 1, pp. L1 – L7, 1996.
- [82] L. Berger, “Emission of spin waves by a magnetic multilayer traversed by a current,” *Phys. Rev. B*, vol. 54, pp. 9353–9358, Oct 1996.
- [83] M. Tsoi, A. G. M. Jansen, J. Bass, W.-C. Chiang, M. Seck, V. Tsoi, and P. Wyder, “Excitation of a magnetic multilayer by an electric current,” *Phys. Rev. Lett.*, vol. 80, pp. 4281–4284, May 1998.
- [84] E. B. Myers, D. C. Ralph, J. A. Katine, R. N. Louie, and R. A. Buhrman, “Current-induced switching of domains in magnetic multilayer devices,” *Science*, vol. 285, no. 5429, pp. 867–870, 1999.
- [85] J. A. Katine, F. J. Albert, R. A. Buhrman, E. B. Myers, and D. C. Ralph, “Current-driven magnetization reversal and spin-wave excitations in co /cu /co pillars,” *Phys. Rev. Lett.*, vol. 84, pp. 3149–3152, Apr 2000.

- [86] Y. K. Kato, R. C. Myers, A. C. Gossard, and D. D. Awschalom, “Current-induced spin polarization in strained semiconductors,” *Phys. Rev. Lett.*, vol. 93, p. 176601, Oct 2004.
- [87] I. M. Miron, K. Garello, G. Gaudin, P.-J. Zermatten, M. V. Costache, S. Auffret, S. Bandiera, B. Rodmacq, A. Schuhl, and P. Gambardella, “Perpendicular switching of a single ferromagnetic layer induced by in-plane current injection,” *Nature*, vol. 476, no. 7359, pp. 189–193, 2011.
- [88] L. Liu, C.-F. Pai, Y. Li, H. W. Tseng, D. C. Ralph, and R. A. Buhrman, “Spin-torque switching with the giant spin hall effect of tantalum,” *Science*, vol. 336, no. 6081, pp. 555–558, 2012.
- [89] H. Kurebayashi, J. Sinova, D. Fang, A. C. Irvine, T. D. Skinner, J. Wunderlich, V. Novák, R. P. Campion, B. L. Gallagher, E. K. Vehstedt, L. P. Zârbo, K. Věrborná, A. J. Ferguson, and T. Jungwirth, “An antidamping spin-orbit torque originating from the berry curvature,” *Nature Nanotechnology*, vol. 9, no. 3, pp. 211–217, 2014.
- [90] V. Edelstein, “Spin polarization of conduction electrons induced by electric current in two-dimensional asymmetric electron systems,” *Solid State Communications*, vol. 73, no. 3, pp. 233 – 235, 1990.
- [91] A. R. Mellnik, J. S. Lee, A. Richardella, J. L. Grab, P. J. Mintun, M. H. Fischer, A. Vaezi, A. Manchon, E.-A. Kim, N. Samarth, and D. C. Ralph, “Spin-transfer torque generated by a topological insulator,” *Nature*, vol. 511, no. 7510, pp. 449–451, 2014.
- [92] P. Li, W. Wu, Y. Wen, C. Zhang, J. Zhang, S. Zhang, Z. Yu, S. A. Yang, A. Manchon, and X.-x. Zhang, “Spin-momentum locking and spin-orbit torques in magnetic nano-heterojunctions composed of weyl semimetal WTe_2 ,” *Nature Communications*, vol. 9, no. 1, p. 3990, 2018.
- [93] X. Wan, A. M. Turner, A. Vishwanath, and S. Y. Savrasov, “Topological semimetal and fermi-arc surface states in the electronic structure of pyrochlore iridates,” *Phys. Rev. B*, vol. 83, p. 205101, May 2011.

- [94] X.-Q. Sun, S.-C. Zhang, and Z. Wang, “Helical spin order from topological dirac and weyl semimetals,” *Phys. Rev. Lett.*, vol. 115, p. 076802, Aug 2015.
- [95] S.-Y. Xu, C. Liu, S. K. Kushwaha, R. Sankar, J. W. Krizan, I. Belopolski, M. Neupane, G. Bian, N. Alidoust, T.-R. Chang, H.-T. Jeng, C.-Y. Huang, W.-F. Tsai, H. Lin, P. P. Shibayev, F.-C. Chou, R. J. Cava, and M. Z. Hasan, “Observation of fermi arc surface states in a topological metal,” *Science*, vol. 347, no. 6219, pp. 294–298, 2015.
- [96] Y. Sun, S.-C. Wu, and B. Yan, “Topological surface states and fermi arcs of the noncentrosymmetric weyl semimetals taas, tap, nbas, and nbp,” *Phys. Rev. B*, vol. 92, p. 115428, Sep 2015.
- [97] D. MacNeill, G. M. Stiehl, M. H. D. Guimaraes, R. A. Buhrman, J. Park, and D. C. Ralph, “Control of spinâeur” orbit torques through crystal symmetry in wte2/ferromagnet bilayers,” *Nature Physics*, vol. 13, no. 3, pp. 300–305, 2017.
- [98] W. Zhang, J. Sklenar, B. Hsu, W. Jiang, M. B. Jungfleisch, J. Xiao, F. Y. Fradin, Y. Liu, J. E. Pearson, J. B. Ketterson, Z. Yang, and A. Hoffmann, “Research update: Spin transfer torques in permalloy on monolayer mos2,” *APL Materials*, vol. 4, no. 3, p. 032302, 2016.
- [99] Q. Shao, G. Yu, Y.-W. Lan, Y. Shi, M.-Y. Li, C. Zheng, X. Zhu, L.-J. Li, P. K. Amiri, and K. L. Wang, “Strong rashba-edelstein effect-induced spinâeur” orbit torques in monolayer transition metal dichalcogenide/ferromagnet bilayers,” *Nano Letters*, vol. 16, pp. 7514–7520, Dec 2016.
- [100] N. Yoshimura, *Vacuum technology: practice for scientific instruments*. Springer Science & Business Media, 2007.
- [101] K. Oura, V. Lifshits, A. Saranin, A. Zotov, and M. Katayama, *Surface science: an introduction*. Springer Science & Business Media, 2013.
- [102] M. A. Herman and H. Sitter, *Molecular beam epitaxy: fundamentals and current status*, vol. 7. Springer Science & Business Media, 2012.

-
- [103] J. R. Arthur, “Molecular beam epitaxy,” *Surface science*, vol. 500, no. 1-3, pp. 189–217, 2002.
- [104] M. A. Herman, W. Richter, and H. Sitter, *Epitaxy: physical principles and technical implementation*, vol. 62. Springer Science & Business Media, 2013.
- [105] W. Braun, *Applied RHEED: reflection high-energy electron diffraction during crystal growth*, vol. 154. Springer Science & Business Media, 1999.
- [106] U. Pietsch, V. Holy, and T. Baumbach, *High-resolution X-ray scattering: from thin films to lateral nanostructures*. Springer Science & Business Media, 2004.
- [107] X. Chen, X.-C. Ma, K. He, J.-F. Jia, and Q.-K. Xue, “Molecular beam epitaxial growth of topological insulators,” *Advanced Materials*, vol. 23, no. 9, pp. 1162–1165, 2011.
- [108] Y.-Y. Li, G. Wang, X.-G. Zhu, M.-H. Liu, C. Ye, X. Chen, Y.-Y. Wang, K. He, L.-L. Wang, X.-C. Ma, *et al.*, “Intrinsic topological insulator Bi_2Te_3 thin films on Si and their thickness limit,” *Advanced materials*, vol. 22, no. 36, pp. 4002–4007, 2010.
- [109] C.-Z. Chang, J. Zhang, X. Feng, J. Shen, Z. Zhang, M. Guo, K. Li, Y. Ou, P. Wei, L.-L. Wang, *et al.*, “Experimental observation of the quantum anomalous hall effect in a magnetic topological insulator,” *Science*, vol. 340, no. 6129, pp. 167–170, 2013.
- [110] N. Bansal, Y. S. Kim, M. Brahlek, E. Edrey, and S. Oh, “Thickness-independent transport channels in topological insulator Bi_2Se_3 thin films,” *Physical review letters*, vol. 109, no. 11, p. 116804, 2012.
- [111] A. Bedoya-Pinto, C. Zube, J. Malindretos, A. Urban, and A. Rizzi, “Epitaxial $\delta\text{-Mn}_x\text{Ga}_{1-x}$ layers on GaN (0001): Structural, magnetic, and electrical transport properties,” *Physical Review B*, vol. 84, no. 10, p. 104424, 2011.

- [112] B. Gopalakrishnan, C. Sürgers, R. Montbrun, A. Singh, M. Uhlarz, and H. v. Löhneysen, “Electronic transport in magnetically ordered $\text{mn}_5\text{si}_3\text{cx}$ films,” *Physical Review B*, vol. 77, no. 10, p. 104414, 2008.
- [113] M. Liu, C.-Z. Chang, Z. Zhang, Y. Zhang, W. Ruan, K. He, L.-l. Wang, X. Chen, J.-F. Jia, S.-C. Zhang, *et al.*, “Electron interaction-driven insulating ground state in bi_2se_3 topological insulators in the two-dimensional limit,” *Physical review B*, vol. 83, no. 16, p. 165440, 2011.
- [114] A. Roy, S. Guchhait, S. Sonde, R. Dey, T. Pramanik, A. Rai, H. C. Movva, L. Colombo, and S. K. Banerjee, “Two-dimensional weak anti-localization in bi_2te_3 thin film grown on $\text{si}(111)-(7\times 7)$ surface by molecular beam epitaxy,” *Applied Physics Letters*, vol. 102, no. 16, p. 163118, 2013.
- [115] A. Abrikosov, “Quantum magnetoresistance,” *Physical Review B*, vol. 58, no. 5, p. 2788, 1998.
- [116] X. Wang, Y. Du, S. Dou, and C. Zhang, “Room temperature giant and linear magnetoresistance in topological insulator bi_2te_3 nanosheets,” *Physical Review Letters*, vol. 108, no. 26, p. 266806, 2012.
- [117] Y. S. Kim, M. Brahlek, N. Bansal, E. Edrey, G. A. Kapilevich, K. Iida, M. Tanimura, Y. Horibe, S.-W. Cheong, and S. Oh, “Thickness-dependent bulk properties and weak antilocalization effect in topological insulator bi_2se_3 ,” *Physical Review B*, vol. 84, no. 7, p. 073109, 2011.
- [118] W. Zhang, W. Han, X. Jiang, S.-H. Yang, and S. S. Parkin, “Role of transparency of platinum–ferromagnet interfaces in determining the intrinsic magnitude of the spin hall effect,” *Nature Physics*, vol. 11, no. 6, pp. 496–502, 2015.
- [119] J. C. Sankey, Y.-T. Cui, J. Z. Sun, J. C. Slonczewski, R. A. Buhrman, and D. C. Ralph, “Measurement of the spin-transfer-torque vector in magnetic tunnel junctions,” *Nature Physics*, vol. 4, no. 1, pp. 67–71, 2008.

-
- [120] H. Kubota, A. Fukushima, K. Yakushiji, T. Nagahama, S. Yuasa, K. Ando, H. Maehara, Y. Nagamine, K. Tsunekawa, D. D. Djayaprawira, *et al.*, “Quantitative measurement of voltage dependence of spin-transfer torque in mgo-based magnetic tunnel junctions,” *Nature Physics*, vol. 4, no. 1, pp. 37–41, 2008.
- [121] L. Liu, T. Moriyama, D. Ralph, and R. Buhrman, “Spin-torque ferromagnetic resonance induced by the spin hall effect,” *Physical review letters*, vol. 106, no. 3, p. 036601, 2011.
- [122] C. Kittel, “On the theory of ferromagnetic resonance absorption,” *Physical review*, vol. 73, no. 2, p. 155, 1948.
- [123] M. Jamali, J. S. Lee, J. S. Jeong, F. Mahfouzi, Y. Lv, Z. Zhao, B. K. Nikolic, K. A. Mkhoyan, N. Samarth, and J.-P. Wang, “Giant spin pumping and inverse spin hall effect in the presence of surface and bulk spin-orbit coupling of topological insulator Bi_2Se_3 ,” *Nano letters*, vol. 15, no. 10, pp. 7126–7132, 2015.
- [124] A. Mellnik, J. Lee, A. Richardella, J. Grab, P. Mintun, M. H. Fischer, A. Vaezi, A. Manchon, E.-A. Kim, N. Samarth, *et al.*, “Spin-transfer torque generated by a topological insulator,” *Nature*, vol. 511, no. 7510, pp. 449–451, 2014.
- [125] Y. Liu, J. Besbas, Y. Wang, P. He, M. Chen, D. Zhu, Y. Wu, J. M. Lee, L. Wang, J. Moon, *et al.*, “Direct visualization of current-induced spin accumulation in topological insulators,” *Nature communications*, vol. 9, no. 1, pp. 1–6, 2018.
- [126] P. Deorani, J. Son, K. Banerjee, N. Koirala, M. Brahlek, S. Oh, and H. Yang, “Observation of inverse spin hall effect in bismuth selenide,” *Physical Review B*, vol. 90, no. 9, p. 094403, 2014.
- [127] Y. Fan, P. Upadhyaya, X. Kou, M. Lang, S. Takei, Z. Wang, J. Tang, L. He, L.-T. Chang, M. Montazeri, *et al.*, “Magnetization switching through giant

- spin-orbit torque in a magnetically doped topological insulator heterostructure,” *Nature materials*, vol. 13, no. 7, pp. 699–704, 2014.
- [128] Y. Wang, P. Deorani, K. Banerjee, N. Koirala, M. Brahlek, S. Oh, and H. Yang, “Topological surface states originated spin-orbit torques in Bi_2Se_3 ,” *Physical review letters*, vol. 114, no. 25, p. 257202, 2015.
- [129] Q. Shao, H. Wu, Q. Pan, P. Zhang, L. Pan, K. Wong, X. Che, and K. L. Wang, “Room temperature highly efficient topological insulator/mo/cofeb spin-orbit torque memory with perpendicular magnetic anisotropy,” in *2018 IEEE International Electron Devices Meeting (IEDM)*, pp. 36–3, IEEE, 2018.
- [130] A. Dankert, J. Geurs, M. V. Kamalakar, S. Charpentier, and S. P. Dash, “Room temperature electrical detection of spin polarized currents in topological insulators,” *Nano letters*, vol. 15, no. 12, pp. 7976–7981, 2015.
- [131] P. He, S. S.-L. Zhang, D. Zhu, Y. Liu, Y. Wang, J. Yu, G. Vignale, and H. Yang, “Bilinear magnetoelectric resistance as a probe of three-dimensional spin texture in topological surface states,” *Nature Physics*, vol. 14, no. 5, pp. 495–499, 2018.
- [132] Y. Fan, X. Kou, P. Upadhyaya, Q. Shao, L. Pan, M. Lang, X. Che, J. Tang, M. Montazeri, K. Murata, *et al.*, “Electric-field control of spin-orbit torque in a magnetically doped topological insulator,” *Nature nanotechnology*, vol. 11, no. 4, pp. 352–359, 2016.
- [133] X. Wang, L. Cheng, D. Zhu, Y. Wu, M. Chen, Y. Wang, D. Zhao, C. B. Boothroyd, Y. M. Lam, J.-X. Zhu, *et al.*, “Ultrafast spin-to-charge conversion at the surface of topological insulator thin films,” *Advanced Materials*, vol. 30, no. 52, p. 1802356, 2018.
- [134] Y. Liu, Z. Yuan, R. J. Wesselink, A. A. Starikov, and P. J. Kelly, “Interface enhancement of gilbert damping from first principles,” *Physical review letters*, vol. 113, no. 20, p. 207202, 2014.

- [135] J.-C. Rojas-Sánchez, N. Reyren, P. Laczkowski, W. Savero, J.-P. Attané, C. Deranlot, M. Jamet, J.-M. George, L. Vila, and H. Jaffrès, “Spin pumping and inverse spin hall effect in platinum: the essential role of spin-memory loss at metallic interfaces,” *Physical review letters*, vol. 112, no. 10, p. 106602, 2014.
- [136] L. Wang, R. Wesselink, Y. Liu, Z. Yuan, K. Xia, and P. J. Kelly, “Giant room temperature interface spin hall and inverse spin hall effects,” *Physical review letters*, vol. 116, no. 19, p. 196602, 2016.
- [137] H. Wang, J. Kally, J. S. Lee, T. Liu, H. Chang, D. R. Hickey, K. A. Mkhoyan, M. Wu, A. Richardella, and N. Samarth, “Surface-state-dominated spin-charge current conversion in topological-insulator–ferromagnetic-insulator heterostructures,” *Physical review letters*, vol. 117, no. 7, p. 076601, 2016.
- [138] J. Zhang, C.-Z. Chang, Z. Zhang, J. Wen, X. Feng, K. Li, M. Liu, K. He, L. Wang, X. Chen, *et al.*, “Band structure engineering in (bi 1- x sb x) 2 te 3 ternary topological insulators,” *Nature communications*, vol. 2, no. 1, pp. 1–6, 2011.
- [139] Z. B. Siu, Y. Wang, H. Yang, and M. B. Jalil, “Spin accumulation in topological insulator thin films—influence of bulk and topological surface states,” *Journal of Physics D: Applied Physics*, vol. 51, no. 42, p. 425301, 2018.
- [140] Y. Wang, D. Zhu, Y. Wu, Y. Yang, J. Yu, R. Ramaswamy, R. Mishra, S. Shi, M. Elyasi, K.-L. Teo, *et al.*, “Room temperature magnetization switching in topological insulator-ferromagnet heterostructures by spin-orbit torques,” *Nature communications*, vol. 8, no. 1, pp. 1–6, 2017.
- [141] J. Han, A. Richardella, S. A. Siddiqui, J. Finley, N. Samarth, and L. Liu, “Room-temperature spin-orbit torque switching induced by a topological insulator,” *Physical review letters*, vol. 119, no. 7, p. 077702, 2017.
- [142] Y. Ando, T. Hamasaki, T. Kurokawa, K. Ichiba, F. Yang, M. Novak, S. Sasaki, K. Segawa, Y. Ando, and M. Shiraishi, “Electrical detection of the

- spin polarization due to charge flow in the surface state of the topological insulator bi1. 5sb0. 5te1. 7se1. 3,” *Nano letters*, vol. 14, no. 11, pp. 6226–6230, 2014.
- [143] K. Kondou, R. Yoshimi, A. Tsukazaki, Y. Fukuma, J. Matsuno, K. Takahashi, M. Kawasaki, Y. Tokura, and Y. Otani, “Fermi-level-dependent charge-to-spin current conversion by dirac surface states of topological insulators,” *Nature Physics*, vol. 12, no. 11, pp. 1027–1031, 2016.
- [144] J. S. Lee, A. Richardella, D. R. Hickey, K. A. Mkhoyan, and N. Samarth, “Mapping the chemical potential dependence of current-induced spin polarization in a topological insulator,” *Physical Review B*, vol. 92, no. 15, p. 155312, 2015.
- [145] C. H. Li, O. M. van’t Erve, S. Rajput, L. Li, and B. T. Jonker, “Direct comparison of current-induced spin polarization in topological insulator bi 2 se 3 and inas rashba states,” *Nature communications*, vol. 7, no. 1, pp. 1–8, 2016.
- [146] M. Mogi, R. Yoshimi, A. Tsukazaki, K. Yasuda, Y. Kozuka, K. Takahashi, M. Kawasaki, and Y. Tokura, “Magnetic modulation doping in topological insulators toward higher-temperature quantum anomalous hall effect,” *Applied Physics Letters*, vol. 107, no. 18, p. 182401, 2015.
- [147] Y. Ou, C. Liu, G. Jiang, Y. Feng, D. Zhao, W. Wu, X.-X. Wang, W. Li, C. Song, L.-L. Wang, *et al.*, “Enhancing the quantum anomalous hall effect by magnetic codoping in a topological insulator,” *Advanced materials*, vol. 30, no. 1, p. 1703062, 2018.
- [148] Y. Tokura, K. Yasuda, and A. Tsukazaki, “Magnetic topological insulators,” *Nature Reviews Physics*, vol. 1, no. 2, pp. 126–143, 2019.
- [149] M. Nadeem, A. R. Hamilton, M. S. Fuhrer, and X. Wang, “Quantum anomalous hall effect in magnetic doped topological insulators and ferromagnetic spin-gapless semiconductors—a perspective review,” *Small*, vol. 16, no. 42, p. 1904322, 2020.

Publications

[1]Guowei Li*, Jue Huang*, Qun Yang, Liguozhang, Qingge Mu, Yan Sun, Stuart S. P. Parkin, Kai Chang and Claudia Felser."MoS₂ on topological insulator Bi₂Te₃ thin films: Activation of the basal plane for hydrogen reduction." Journal of Energy Chemistry 62 (2021): 516-522.(* contribute equally)

Acknowledgements

I would like to acknowledge the continuous support and encouragement from many colleagues.

First and foremost, I would like to thank my supervisor Prof. Stuart S.P. Parkin for his mentorship and support. With his great passion and deep scientific knowledge, Stuart is the ideal role-model of a scientist and this inspired me a lot. He gave me large freedom to study the topics that I am interested in and gave me advice and guidance whenever I met challenges. He always encouraged me with my research project which helped me continuing my way towards a doctoral degree. I am so fortunate to have this opportunity to work in his research group at Max Planck Institute of Microstructure Physics.

Next, I would like to thank Kai Chang for teaching me UHV techniques and MBE. Without his initial training I would not have been able to build up the MBE system and get my project started. He is a very kind person who supported me a lot. With his experience and knowledge, I managed to avoid mistakes at the beginning of my thesis.

Besides, I also want to thank Amilcar Bedoya Pinto advising me on data analysis and interpretation as well as providing feedback whenever needed.

I also want to thank all present and former members of our research group. We had many fruitful discussions and I acknowledge especially the support of Fasil Kidane Dejene, Edouard Lesne, Yunyi Zang, James Taylor, Tianping Ma, Jibo Zhang, and Jingrong Ji. My special thanks go to James Taylor for his support with the revision of my thesis.

Another special thank you goes to Simone Jäger, to whom I could always talk to even facing difficult moments.

Last but not least, I would like to express my deepest gratitude to my beloved family: my parents, my sister, and my husband. Thanks for their unconditional love, support and encouragement.

Curriculum Vitae

Name: Jue Huang
Gender: Female
Date of Birth: 24.12.1989
Place of Birth: Anhui, China
Nationality: Chinese

ACADEMIC EDUCATION

08/2015-present PhD student of Natural Sciences in Physics
Max Planck Institute of Microstructure Physics and Martin-Luther-
University Halle-Wittenberg, Halle, Germany

09/2012-07/2015 Master's Degree in Materials Science and Engineering
Tsinghua University, Beijing, China

09/2007-07/2011 Bachelor's Degree in Materials Science and Engineering
Central South University, Changsha, China

Jue Huang
Halle(Saale), Germany
16.12.2020

Eidesstattliche Erklärung

Hiermit erkläre ich, Jue Huang, dass ich die vorliegende Arbeit mit dem Titel: **Epitaxial growth and charge-to-spin conversion studies of Bi₂Te₃ topological insulator** in allen Teilen selbständig verfasst und keine anderen als die angegebenen Quellen und Hilfsmittel benutzt habe. Alle wörtlich oder sinngemäß übernommenen Textstellen habe ich als solche kenntlich gemacht.

Ferner liegen gegen mich weder gerichtliche Vorstrafen vor, noch sind staatsanwaltliche Ermittlungen oder Disziplinarverfahren eingeleitet worden.

Des Weiteren erkläre ich hiermit, dass ich bisher keine andere Arbeit zur Promotion eingereicht noch mit einer anderen Arbeit den Versuch zur Promotion unternommen habe.

Halle(Saale), Germany

16.12.2020

Jue Huang